

Modelling and validation of a hybrid damper in a new non-linear shock and vibration isolation system

Master's Thesis

Tax, J.C.A. (Joep)

DC 2016.031

Supervisor:
Prof.dr. H. Nijmeijer

Coaches:
Dr.ir. R.H.B. Fey (TU/e)
Dr.ir. P.W.J.M. Nuij (NTS SD)
Ir. A. Abbasi (NTS SD)

Committee:
Prof.dr. H. Nijmeijer
Dr.ir. R.H.B. Fey
Dr.ir. P.W.J.M. Nuij
Dr.ir. J.J.C. Remmers

Eindhoven, May 2016

Abstract

In the design process of high-tech precision equipment most emphasis is on requirements under operating conditions. While operating requirements become more strict, the complexity and vulnerability increases. During the transport from manufacturer to customer site the external disturbance level is significantly higher than under operation. Delicate precision equipment is very vulnerable for this kind of input and will be damaged without a proper transport casing. NTS Group designs and builds transport tools to safely transport this kind of equipment. In this thesis, the isolation system of a transport tool is considered. More specifically, the use of non-linear passive isolation components is explored both analytically and experimentally.

The performance of the floor excited isolation system is assessed by the vibration isolation and shock absorption capabilities. Two passive components are analysed and compared: viscoelastic elastomer components are chosen for their vibration isolation performance and friction based wire rope isolators for their shock absorption properties. Next, the elastomer and wire rope isolator are connected in series (i.e. the hybrid configuration) to gain performance for both vibration isolation and shock absorption.

The non-linear amplitude dependent wire rope behaviour is modelled by the modified Iwan model, whereas the linear elastomer is described by the (linear) generalized Maxwell model. These models are also implemented in the model of the hybrid configuration. Simulations with harmonic floor excitation and conditioned free falls are made to gain insight into the characteristic behaviour of the isolation systems. Quasi-static, shaker, and drop test experiments are performed to identify and validate the models. The qualitative behaviour of the isolators is accurately described and the models provide a good approximation of the quantitative behaviour.

Inputs described by PSD spectra of the floor acceleration are used to compare the isolation systems for realistic vibrational input. Secondly, the maximum absolute acceleration values resulting from the conditioned free fall simulations are compared. Several hybrid systems, with varying stiffness ratio of wire rope to elastomer component, are considered. The damping and isolation properties of the linear elastomer system are good, however the shock performance is limited by its linear character. For the non-linear wire rope and hybrid systems the damping and isolation performance is highly dependent on the specific input. The shock absorption performance of the hybrid systems is bounded by the performance of the elastomer and wire rope system.

The use of well designed non-linear passive elements increases the overall performance of the isolation system. However, there is still a trade-off between the vibration isolation and shock absorption performance.

Glossary

List of Acronyms

Acronym	Description
2D	Two Dimensional
3D	Three Dimensional
DCT-lab	The Dynamics and Control Technology Laboratory (TU/e)
DEM	Discrete Element Method
FEM	Finite Element Method
FRF	Frequency Response Function
GA	Genetic Algorithm
GHM	Golla-Hughes-McTravis
HOSIDF	Higher Order Sinusoidal Input Describing Function
ODE	Ordinary Differential Equation
PSD	Power Spectral Density
RMS	Root Mean Square
SDOF	Single Degree of Freedom
SQP	Sequential Quadratic Programming

Nomenclature

List of roman symbols

Symbol	Description	Unit
a	Acceleration	$[m/s^2]$
b	Modulating parameter Bouc-Wen model	$[-]$
c	Exponential modulating parameter Bouc-Wen model	$[m^{-1}]$
d	Damping constant	$[Ns/m]$
e	Optimization error	$[-]$
f	Frequency	$[Hz]$
f_0	Undamped eigenfrequency	$[Hz]$
f_n	Sample frequency	$[Hz]$
g	Gravitational constant ($9.81 m/s^2$)	$[m/s^2]$
g_1	Linear stiffness term parallel spring Iwan model	$[N/m]$
g_2	Quadratic stiffness term parallel spring Iwan model	$[N/m^2]$
g_3	Cubic stiffness term parallel spring Iwan model	$[N/m^3]$
h	Drop height	$[m]$
k	Stiffness	$[N/m]$
k_{bw1}	Linear stiffness term Bouc-Wen model	$[N/m]$
k_{bw2}	Quadratic stiffness term Bouc-Wen model	$[N/m^2]$
k_{bw3}	Cubic stiffness term Bouc-Wen model	$[N/m^3]$
k^*	Complex stiffness standard mechanical models	$[N/m]$
m	Mass	$[kg]$
n	Model order	$[-]$
n_{bw}	Hysteretic parameter Bouc-Wen model	$[-]$
par	Parameter list	$[-]$
r	Convergence parameter Time-stepping method	$[-]$
r_k	Global stiffness ratio hybrid, wire rope to elastomer	$[-]$
s	Laplace operator	$[rad/s]$
t	Time	$[s]$
v	Velocity	$[m/s]$
x	Position (deflection)	$[m]$
\dot{x}	Velocity	$[m/s]$
\ddot{x}	Acceleration	$[m/s^2]$
z	Hysteretic force Bouc-Wen model	$[N]$
F	Force	$[N]$
F_c	Coulomb friction force	$[N]$
H	Complex frequency response	$[-]$
$Im()$	Imaginary part	$[-]$
N	Number of elements	$[-]$
$Re()$	Real part	$[-]$
S	PSD spectrum	$[-]$
U_{in}	Control voltage shaker system	$[V]$

List of greek symbols

Symbol	Description	Unit
α	Hysteretic parameter Bouc-Wen model	$[N/m]$
β	Hysteretic parameter Bouc-Wen model	$[N^{1-m}/m]$
γ	Hysteretic parameter Bouc-Wen model	$[N^{1-m}/m]$
ζ	Damping ratio	$[-]$
η	Loss factor	$[-]$
τ	Time constant	$[s]$
ω	Angular frequency	$[rad/s]$
ω_0	Undamped angular eigenfrequency	$[rad/s]$

List of subscripts

Subscript	Description
b	Base (floor)
bw	Bouc-Wen model parameter
eff	Effective
el	Generalized Maxwell model parameter
in	Intermediate mass
$Jenkin$	Jenkin element parameter
m	Machine (top mass)
$meas$	Measured variable
$model$	Modelled variable
wr	Iwan model parameter

Contents

Abstract	iii
Glossary	v
1 Introduction	1
1.1 Transport tool	1
1.2 Objectives and outline	2
2 Vibration and shock reduction	3
2.1 Damping, vibration isolation, and shock reduction	3
2.2 Viscoelastic components	4
2.3 Friction based isolators	5
2.4 Particle dampers	6
2.5 Other passive damping techniques	6
2.6 Active damping	6
2.7 Scope of the remainder of the thesis	7
3 Wire rope isolators	9
3.1 Friction based isolation	9
3.2 Modelling	9
3.2.1 Bouc-Wen model	10
3.2.2 Iwan model	10
3.3 Simulation aspects	14
3.3.1 Parallel Coulomb-spring element	14
3.3.2 Parallel series Iwan model	15
3.4 Vibration and shock analysis	16
3.4.1 Vibrations: symmetric wire rope isolator behaviour	17
3.4.2 Vibrations: asymmetric wire rope isolator behaviour	20
3.4.3 Shock	24
3.5 Summary	26
4 Elastomer isolators	27
4.1 Viscoelasticity	27
4.2 Modelling	28
4.2.1 Standard mechanical models	28
4.3 Vibration and shock analysis	30
4.3.1 Vibrations	30
4.3.2 Shock	31
4.4 Summary	32
5 Hybrid isolators	33
5.1 Modelling	33
5.2 Simulation aspects	34
5.3 Vibration and shock analysis	35
5.3.1 Vibrations: symmetric hybrid isolator behaviour	35

5.3.2	Vibrations: asymmetric hybrid isolator behaviour	39
5.3.3	Shock	43
5.4	Summary	44
6	Experiments	45
6.1	Measurement hardware	45
6.2	Wire rope isolator	46
6.2.1	Quasi-static experiment	46
6.2.2	Shaker experiment	48
6.2.3	Drop test	49
6.3	Elastomer isolator	51
6.3.1	Quasi-static experiment	51
6.3.2	Shaker experiment	52
6.3.3	Drop test	54
6.4	Hybrid isolator	55
6.4.1	Quasi-static experiment	55
6.4.2	Shaker experiment	56
6.4.3	Drop test	58
6.5	Summary	59
7	Model identification and validation	61
7.1	Wire rope isolator	61
7.1.1	Identification of the model	61
7.2	Elastomer isolator	63
7.2.1	Identification of the model	63
7.3	Hybrid isolator	67
7.4	Summary	67
8	Performance of the isolation system of a transport tool	69
8.1	Transport tool and requirements	69
8.2	Vibration isolation	70
8.3	Shock absorption	73
8.4	Summary	74
9	Conclusions and recommendations	75
9.1	Conclusions	75
9.2	Recommendations for further research	76
	Bibliography	79
	Appendix	85
A	Additional simulation results wire rope analysis	85
A.1	Simulations parallel Coulomb-spring element	85
A.2	System parameters	88
A.3	Symmetric isolation system	88
A.4	Asymmetric isolation system	89
A.5	Analysis shock	90
B	Parameters elastomer analysis	91
B.1	System parameters	91
C	Additional simulation results hybrid analysis	93
C.1	Symmetric isolation system	93
C.2	Asymmetric isolation system	94

D	Measurement setups	95
D.1	Measurements hardware	95
D.1.1	Quasi-static setup	95
D.1.2	Dynamical shaker setup	96
D.1.3	Drop test setup	98
D.2	Technical drawings drop test setup	100
D.3	Product sheets isolators	108
E	Additional measurement results	111
E.1	Measurements wire rope isolator	111
E.1.1	Shaker experiment	111
E.1.2	Drop test	114
E.2	Measurements elastomer isolator	115
E.2.1	Shaker experiment	115
E.2.2	Drop test	116
E.3	Measurements hybrid isolator	117
E.3.1	Shaker experiment	117
E.3.2	Drop test	118
F	Model validation	119
F.1	Wire rope isolator	119
F.2	Elastomer isolator	122
F.3	Hybrid isolator	123
	Acknowledgements	127

Chapter 1

Introduction

The performance requirements of precision equipment increases. As a result, also the structure of these machines becomes more complex. Consequently, the allowable environmental disturbance levels due to vibrations, temperature variation, and particle pollution become stricter. This thesis considers the dynamical isolation of a machine from environmental vibrations and shocks.

The design and controls of high-tech precision equipment ensure that high demands are met under operating conditions. However, the equipment is also vulnerable during transport. There is vibrational input disturbance from the floor, representing the mean of transportation, e.g. a truck or airplane. During loading and unloading incidental shock related events occur. The system has to be isolated from floor vibrations and shocks have to be absorbed. A vibration isolation system is needed to achieve this. The combination of the minimum required amount of vibration isolation, shock absorption properties, and other constraints, such as the maximum allowable deflection of the isolation elements results in contradictory system requirements.

In the first section of this introduction, a more detailed description of a transport tool designed by NTS Group for transport of delicate precision equipment is given, with particular focus on the dynamical isolation system. In the second section, the objectives of this thesis is described and the outline is provided.

1.1 Transport tool

NTS Group developed a transport tool in which an optical device is protected from vibration and shock. This optical device consists of many delicate lens components with vulnerable clamp and glue connections. Because of the very low mechanical damping of these elements, one has to ensure not to overexcite the internal dynamics of these optical components. The vibration isolation system basically consists of a fourth order system (two layers of isolation components) to isolate vibrations and absorb shocks. With this system it is possible to safely transport the optical device.

The tool is equipped with one layer of viscoelastic elements tuned to a resonance frequency of approximately 5 Hz and a second layer with viscoelastic elements tuned to 20 Hz . For robustness and simplicity passive elements are chosen. Elastomer isolators have a good performance and are well predictable in terms of dynamical behaviour. The resonance frequency tuning is based on the response to vibrational input. With this configuration, also the shock requirements are met. For increasing performance demands, it is not possible to comply with the requirements for both shock absorption and vibration isolation.

The overall (i.e. combined shock and vibration isolation) performance of the transport tool could be even further increased by making use of different types of (non-linear) isolators. A well designed passive isolation system combines and optimally uses the properties of the separate components.

1.2 Objectives and outline

The main objective of this thesis is to explore the use of a new so-called hybrid isolator in floor excited vibration isolation systems, in order to combine the vibration isolation properties of an elastomer isolator (for small signal input) and the shock absorption properties of a wire rope isolator (for large signal input). Here, a hybrid isolator is defined as an elastomer and wire rope isolator in series. The sub objectives to explore the use of a hybrid isolator are:

- Modelling of the wire rope, elastomer, and hybrid isolator.
- Numerical analysis of the wire rope, elastomer, and hybrid isolation systems.
- Experiments with different types of excitation.
- Model identification and validation.
- Comparison of the identified isolation systems.

In chapter 2, an introduction in vibration isolation and shock absorption systems is given and a brief literature overview of different types isolators is presented. In the last section, the scope of this thesis is further substantiated. The next chapters discuss the modelling and simulation of three different types of isolators, i.e. wire rope isolators (chapter 3), elastomer isolators (chapter 4), and hybrid isolators (chapter 5). In these chapters, inputs in terms of both vibrations and shocks are considered. The main goal of the analysis in these chapters is to gain detailed insight in the characteristic isolator behaviour. The model parameters used, are chosen close to the expected experimental values.

The knowledge obtained in chapters 3-5 is used to design three experiments. The separate isolators are examined by quasi-static measurements, and the isolation systems by small signal input (vibrations) and large signal input (shock). The results of these quasi-static, vibrational, and shock experiments are presented in chapter 6. In chapter 7, the experimentally obtained data is used to identify model parameters and to validate the derived models.

In chapter 8, simulations with NTS specifications are done to assess and compare the performance of the different isolation systems for a realistic application. Lastly, in chapter 9, the final conclusions and recommendations for future research are presented.

Chapter 2

Vibration and shock reduction

In literature, vibration isolation and shock absorption is widely discussed [25,44,63,64,73]. Vibration and shock reduction is a broad area of interest for among others; damping of structures, vehicle suspension performance, and isolation of high-tech machines.

There are many different types of vibration isolators and shock absorbers available. A number of them are discussed in this chapter: viscoelastic dampers, friction based isolators, particle dampers, and controlled isolation systems. The last category comprises (semi-)active systems; the other types of isolators are passive. There are many more isolation solutions, which are not considered in this report.

This chapter is organized as follows. In the first section, the concepts of damping, vibration isolation, and shock absorption are briefly discussed and illustrated. In the next sections, the different types of isolators are discuss separately, on the basis of existing studies. The last section involves a short summary of the different isolator types and focusses on the scope of the remainder of the thesis.

2.1 Damping, vibration isolation, and shock reduction

An isolation system basically consists of a mass, a spring, and a damper. A schematic overview is shown in figure 2.1. The spring component stores energy, whereas the damper element dissipates energy. In isolation systems, both damping and isolation are important phenomena. To illustrate both effects the transmissibility diagram of a floor motion excited system is explained. The transfer function is given by:

$$\frac{x_m(s)}{x_b(s)} = \frac{ds + k}{ms^2 + ds + k} \quad (2.1)$$

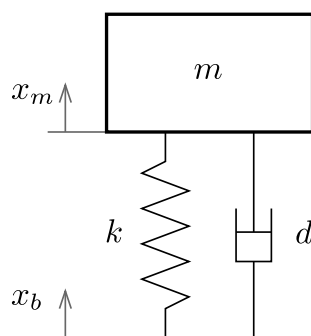


Figure 2.1: Schematic overview mass-spring-damper system.

The frequency response function (FRF) of the transfer function is shown in the Bode diagram in figure 2.2 [51, 52]. A mass of $m = 1 \text{ kg}$, damping constant of $d = 2 \cdot 10^{-5} \text{ N s/m}$ (undamped) or $d = 0.2 \text{ N s/m}$ (damped), and stiffness of $k = 1 \text{ N/m}$ are used. Frequencies above the eigenfrequency are suppressed, in other words isolation is achieved. The resonance peak of the undamped system is lowered by adding damping. However, damping has a negative influence on the isolation properties of the system because it reduces the isolation at high frequencies.

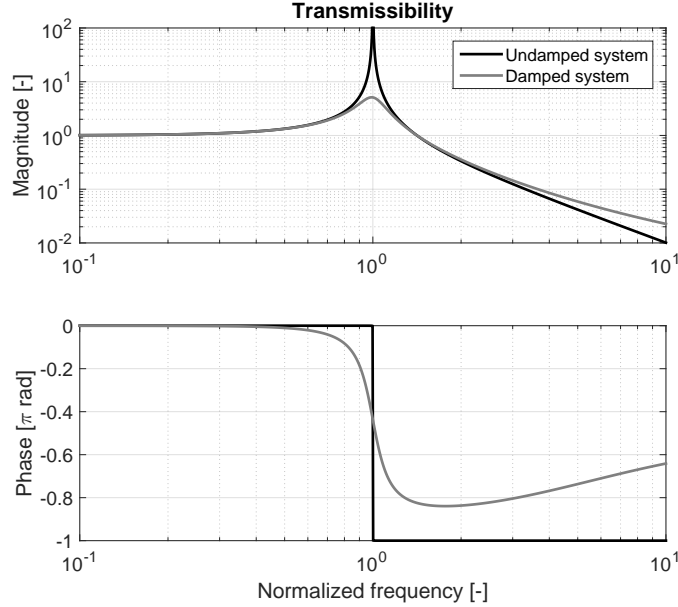


Figure 2.2: Transmissibility (FRF) linear system.

In this example, a linear spring and dashpot damper are used. These elements approximate the behaviour of real-life isolators. Using linear elements enables simple and fast analysis in both time domain and frequency domain. The frequency response of a system, as shown in figure 2.2, is a good measure to analyse the response of a linear system to periodic vibrations. For shock however, time domain analysis is more suitable.

The shock absorption performance is mainly assessed by the peak acceleration level, which is directly related to force. To a minor extent, also deflection is important regarding design space and available spring travel. Considering a system as shown in figure 2.1 without damping (i.e. $d \approx 0$), shock is an instantaneous change in velocity over the isolator (i.e. a step in $\dot{x}_m(t) - \dot{x}_b(t)$). A soft spring results in a low acceleration and a large deflection. Whereas the response of a stiff system shows a small deflection and high acceleration, i.e. the same energy is stored in less deflection. Adding damping means removing mechanical energy from the system, which is obviously beneficial for both decreasing the acceleration and deflection levels.

2.2 Viscoelastic components

An important and commonly used type of vibration isolators is made of rubber-like materials, elastomers. This type of materials is characterized by a combination of viscous and elastic behaviour: viscoelasticity. Both solids and liquids can show viscoelastic behaviour. The behaviour is strongly dependent on temperature and frequency. In this thesis, the temperature is assumed to be constant. Relaxation and creep phenomena will not be considered in detail. Frequency however, affects both the stiffness and dissipation properties and will be taken into account [45, 62, 65].

Viscoelastic models can be divided in two different types of models: physical and (semi-)empirical. Empirical models are defined in the frequency domain to match the frequency dependency of the viscoelastic component. The Golla-Hughes-McTravis (GHM) [20, 43, 76] and fractional derivative model [1, 3, 21, 60] are two examples of this type of models. They are widely used in finite element models (FEM) and modal analysis.

Physical models are based on the internal mechanical behaviour of the viscoelastic material. Such a model consists of spring and dashpot elements. The most elementary configurations are a spring and dashpot in series or in parallel, i.e. respectively the Maxwell or Voigt model. Note that the Voigt model represents a linear viscously damped system, as shown in figure 2.2. A more elaborate model is the generalized Maxwell model, which consists of a single spring in parallel with several Maxwell elements. This model is, as well as the empirical models, capable of accurately describing the frequency dependent behaviour. The advantage of the generalized Maxwell model, compared to empirical models, is the clear physical meaning of the model parameters [57, 65]. All models mentioned in this section result in linear input-output behaviour (for a specific frequency).

2.3 Friction based isolators

Another type of isolators is based on energy dissipation by friction. The behaviour of such isolators is highly non-linear. The simplest form of a friction based isolator is a Coulomb element with a spring in parallel. In these kinds of systems stick-slip behaviour occurs. In case of small input the friction causes the Coulomb element to stick and the isolator behaves rigidly. In case of large input the Coulomb element will slide and the spring becomes active. Characteristic hysteretic loops are formed [2, 16, 34, 47, 59].

Wire rope isolators are commonly used as shock absorbers in maritime and machine environments. Figure 2.3 shows an example of a wire rope isolator. The main loading direction is vertical. As a result the cables bend and show elastic behaviour. At the same time the different strands develop an internal friction force and eventually start rubbing for larger inputs. This hysteretic behaviour is excitation amplitude dependent. Further, hardening behaviour is observed for tension, whereas during compression softening occurs. Wire rope isolators are robust and not very sensitive to temperature or other environmental disturbances.



Figure 2.3: An example of a helical wire rope isolator.¹

¹SOCITEC catalogue 2015.

Hysteretic behaviour can be described by the Bouc-Wen model. This empirical model describes various hysteretic phenomena. A modified version, to include the asymmetric behaviour, is already applied in several wire rope isolator studies. The model parameters are not directly related to the physical behaviour. In general, the model identification process is complex and may be also badly conditioned [32,48,49,69,82].

A finite element model (FEM) of wire rope isolators exhibits a complex geometry and many contact points between the strands. High computation power is needed to perform these kind of simulations and the contact modelling of all individual strands may be practically infeasible [6,9,10].

Friction models consisting of series and parallel combinations of spring and Coulomb elements are well capable of describing hysteretic behaviour. The stiffness and friction parameters are directly related to the hysteretic loops in the force characteristic. Iwan and Masing proposed general forms of these friction models. A modified form is needed to describe the asymmetric soft-hardening behaviour in the main loading direction, i.e. tension-compression behaviour [8,26,27,67,68,70,71].

2.4 Particle dampers

Particle or impact dampers are another interesting type of vibration dampers. A conventional impact damper consists of one solid particle, which can move freely in an enclosure. This damping system is attached to the machine; a spring connects the machine to the floor or its base. The damping is a result of the linear and angular momentum exchange during particle-wall impacts. An impact damper is effective in a narrow frequency range and produces much noise. In a particle damper, the single solid particle is replaced by multiple smaller solid particles; there is particle-wall and particle-particle interaction. The behaviour is more smooth, the effective frequency range is broader, and the noise level is significantly reduced [12,18,19,31,56].

A special kind of particle dampers comprises a moving piston in a container with multiple solid particles. Downstroke of the piston forces the particles underneath aside, resulting in much piston-particle, particle-particle, and particle-wall interaction. Upstroke the particles freely fill the piston space. During the downstroke the force is high, upstroke there is almost no force [4,72].

Elementary models describe the interaction between particles themselves and between particles with the wall. The discrete element method (DEM) is used to model the position and interaction of the particles. Contact and friction laws describe the interaction forces [11,42,54,66].

2.5 Other passive damping techniques

Next to the small number of passive isolators discussed in the previous sections, there are many more passive techniques to isolate vibrations and absorb shocks [25,44,63,64,73]. Examples are: non-linear viscoelastic mounts, metal springs, composite material springs, hydromounts, and pneumatic isolators. These isolators are not discussed in this report.

2.6 Active damping

In the previous sections, only passive vibration isolators are considered. Semi-active or active isolation systems can be even more effective. In semi-active systems, the stiffness or damping is controlled by low power actuators. In active systems, (high power) actuators provide the stiffness and damping. While the performance of well-designed (semi-)active systems increases, the robustness decreases and the complexity increases [30,73].

An example of semi-active damping is a mass-spring-damper system with switchable stiffness. During shock the system has a low stiffness and in subsequent free vibration the system switches between high and low stiffness. During motion from the equilibrium position the stiffness is high, whereas the stiffness is low while moving to the equilibrium position; this switching results in effective damping [35]. Another approach is controlling the stiffness using electromagnetic components. More specifically, the system is tuned to high static and low dynamic stiffness [83].

Also in other studies semi-active dampers are used. Different control strategies are applied in order to minimize the transmissibility from base to machine. There is a significant effect seen for periodic inputs. However, for random input the effect is small [37, 39]. By choosing a system with constant springs and controllable dampers in mixed parallel and series configuration, it is possible to control both the stiffness and damping of the isolation system [38].

Active isolation systems require high actuation power and a well-tuned control strategy. Basically an extra actively controlled isolation component is added. The controller uses real time position and motion information to determine the actuation force. With active isolation systems it is possible to both isolate vibrations and to follow a desired trajectory [7, 13, 30].

2.7 Scope of the remainder of the thesis

Different types of isolators are discussed in this chapter. Both passive and (semi-)active isolator systems are explained. For robustness and simplicity passive components are preferred. Compared to separate passive components, (semi-)active components can result in a better performance for both vibration isolation and shock absorption. The current transport tool is equipped with (passive) elastomer isolators; the system is very robust, but the combined shock absorption and vibration isolation performance is limited by the linearity of its components. A more elaborated passive system, consisting of different non-linear passive components, is possibly also capable of achieving high performance, while robustness is ensured. In this thesis, different passive components are combined (which results in a so-called hybrid system), to study the main systems performance in terms of floor vibration isolation and shock absorption.

Viscoelastic components, e.g. elastomer mounts, perform well in terms of vibration isolation and resonance damping. However, there is always a trade-off between these performance indicators and shock absorption. Friction based wire rope isolators form a proven and robust solution for shock absorption due to the non-linear hysteretic behaviour. Particle dampers are less suitable to this type of isolation systems and more applicable for structural damping purposes. Therefore, a hybrid system consisting of an elastomer and a wire rope component is analysed in the remainder of this report. The aim is to optimize the hybrid isolator in such a way, that the damping and vibration isolation properties of the elastomer and vibration isolation and shock absorption properties of the wire rope isolator are combined and preserved in the hybrid design.

Hereto, firstly the dynamical behaviour and modelling of the separate wire rope and elastomer components is described, followed by the hybrid analysis.

Chapter 3

Wire rope isolators

In this chapter, the behaviour and modelling of wire rope isolators are discussed. A suitable model includes the highly non-linear characteristics: hysteresis, softening, hardening, and asymmetry. In section 2.3, already a brief introduction is given on friction-based isolators and their modelling. In this chapter, the modelling and dynamical behaviour of a wire rope isolation system is considered in more detail.

In the first section, friction based isolation characteristics are briefly discussed. In section 3.2, two models are described. First the Bouc-Wen model is discussed and secondly the Iwan model. Next to model accuracy itself, the implementation of a model is an important aspect. The model parameters have to be identified unambiguously by measurements and the model should be suitable for dynamical simulations. In the third section, the use of these non-smooth models in dynamical analysis is discussed. Simulations with a wire rope isolator system will be done for both periodic and shock excitation in section 3.4. A short summary is presented in the last section.

3.1 Friction based isolation

Wire rope isolators show both compliant and frictional behaviour. The bending of the wire strands results in compliant behaviour. The rubbing between the strands results in friction forces. Both phenomena characterize the force-displacement relation. The damping properties are determined from the resulting so-called hysteretic behaviour. This also implies that the response of a wire rope isolator is highly non-linear.

A single Coulomb element is the most basic friction element. If the load is below the maximum friction force, F_c , the resulting displacement is zero (stick), for a higher external force sliding occurs (slip). The force-relative velocity characteristic of the Coulomb element is discontinuous and therefore, as a result, the behaviour is highly non-linear.

Friction based isolators are characterized by a high static stiffness and a low dynamic stiffness. For the elementary Coulomb element the static stiffness is infinite, whereas the dynamic stiffness is zero.

3.2 Modelling

There are multiple difficulties in modelling wire rope isolators. Firstly, the most important part is discussed: deriving a suitable model, which accurately describes all aspects of the non-linear behaviour. Secondly, the simulation program or method must be able to solve the resulting highly non-linear equation of motion of the wire rope isolation system. In this section, two different models are described; the simulation programs and methods are discussed in section 3.3.

In section 2.3, already a brief overview was given of the available models. A distinction between physical and empirical models was made. The empirical Bouc-Wen model describes hysteretic behaviour in general. As different studies show, this model is suitable for wire rope isolators [48, 49, 69].

Two types of physical models were mentioned in the previous chapter: finite element models (FEM) and Iwan models. Finite element models are relatively big and cumbersome because of complexity in contact and friction modelling and therefore not efficient for dynamical analysis [6, 9, 10]. The Iwan model is directly related to the hysteretic characteristic of a wire rope isolator. The modelling method is successfully applied to wire ropes and wire cables [8, 67, 68].

3.2.1 Bouc-Wen model

The Bouc-Wen model builds on the model of Bouc [5], which was later extended by Wen. The general form of a hysteretic force is given by [80]:

$$F_{bw}(t) = kx(t) + z(t) \quad (3.1)$$

$$\dot{z}(t) = \alpha\dot{x}(t) - \beta|\dot{x}(t)|z(t)|z(t)|^{n_{bw}-1} - \gamma\dot{x}(t)|z(t)|^{n_{bw}} \quad (3.2)$$

where x is the deflection, k represents a linear stiffness, z is the hysteretic part of the force and the hysteretic model parameters are given by α , β , γ , and n_{bw} . The model in this form describes a symmetric hysteretic system without softening or hardening behaviour. Symmetry is defined here as identical behaviour in tension and compression.

Some small modifications to the original model are made to include asymmetry and soft-hardening, which is already done for wire rope isolators [48, 49, 69]. The isolator force is now given by following equations:

$$F_{bw}(t) = b^{cx(t)}(F_{bw,1}(t) + z(t)) \quad (3.3)$$

$$F_{bw,1}(t) = k_{bw,1}x(t) + k_{bw,2}\text{sgn}(x(t))x(t)^2 + k_{bw,3}x(t)^3 \quad (3.4)$$

$$\dot{z}(t) = \alpha\dot{x}(t) - \beta|\dot{x}(t)|z(t)|z(t)|^{n_{bw}-1} - \gamma\dot{x}(t)|z(t)|^{n_{bw}} \quad (3.5)$$

The stiffness parameters $k_{bw,2}$ and $k_{bw,3}$ are introduced to include the soft-hardening behaviour in the model. The exponential parameters b and c in (3.3) result in an asymmetric description. To ensure numerical stability of the $|z(t)|^{n_{bw}-1}$ term, (3.5) is rewritten to:

$$\dot{z}(t) = \dot{x}(t)\{\alpha - [\gamma + \beta\text{sgn}(\dot{x}(t)\text{sgn}(z(t)))]|z(t)|^{n_{bw}}\} \quad (3.6)$$

The stiffness parameters are related to the actual physics of the wire rope isolator, the other hysteretic model parameters have no direct relation with the physical behaviour. This, in combination with the highly non-linear character of (3.6), complicates the identification process of the model parameters. Time domain identification methods, based on the Gauss-Newton algorithm, are most efficient and robust using a two or three stage scheme [69]. Mixed time-frequency domain methods can identify the model parameters in one stage [49, 69]. Other identification approaches are based on the differential evolution method [32] or on an artificial neural network [82]. The differential evolution method makes no use of derivatives, thus handling non-linearity is no problem. An artificial neural network is a self-learning algorithm, which needs prior training.

3.2.2 Iwan model

Iwan proposed two types of model structures consisting of linear springs and Coulomb friction elements [26, 27]. The parallel-series structure represents a parallel composition of a spring and several spring and Coulomb elements in series. The series-parallel structure consists of a spring and parallel spring and Coulomb elements in series. Both structures are visualized in figure 3.1.

Both Iwan models, with properly chosen parameters, describe the same behaviour. The order of the model, n , is an indication for the smoothness of the characteristic hysteretic loop. The parallel-series model expresses the force, F_{wr} , as a function of the deflection, x , whereas the series-parallel model describes the deflection as a function of the force. Normally, in a dynamical system the force is determined

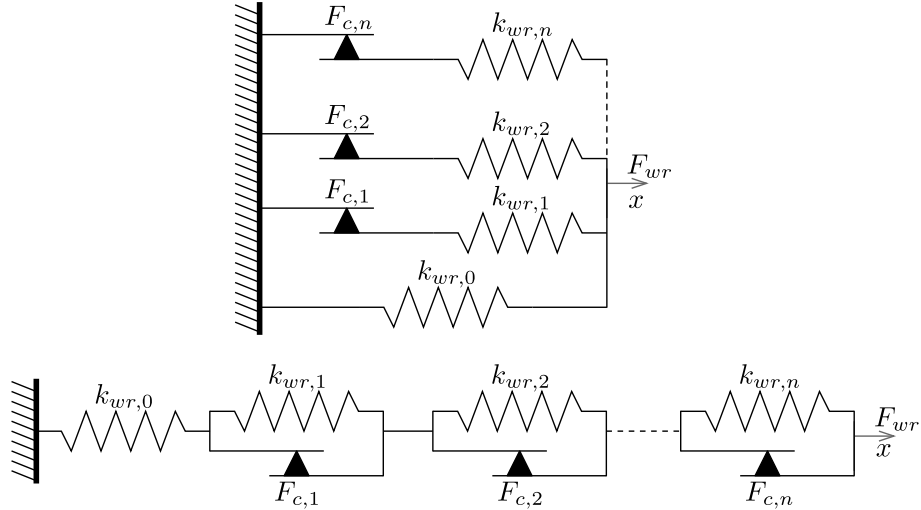


Figure 3.1: Iwan models; top: Parallel-series, below: Series-parallel.

from the displacement. This is according the parallel-series model. Masing also developed a model, which is identical to the parallel-series Iwan model [67,68,71]. The series spring Coulomb elements are so-called Jenkin elements. Figure 3.2 shows a single Jenkin element, the force through a Jenkin element is F_{Jenkin} . Then the force through the symmetric wire rope is expressed by:

$$F_{wr,sym}(t) = k_{wr,0}x(t) + \sum_{i=1}^n F_{Jenkin,i}(t) \quad (3.7)$$

The characteristic force through a single Jenkin element is expressed in terms of its time derivative [67,68]. In this form, only one equation is sufficient to describe the behaviour of both the spring and friction element:

$$\dot{F}_{Jenkin}(t) = \frac{1}{2}k\dot{x}(t)[\text{saturation} + \text{re-activation}] \quad (3.8)$$

$$\text{saturation} = 1 - \text{sign}(F_{Jenkin}(t)^2 - F_c^2) \quad (3.9)$$

$$\text{re-activation} = -\text{sign}(\dot{x}(t)F_{Jenkin}(t)) \cdot (1 + \text{sign}(F_{Jenkin}(t)^2 - F_c^2)) \quad (3.10)$$

where the sign function is described by:

$$\text{sign}(a) = \begin{cases} -1 & \text{if } a < 0 \\ 0 & \text{if } a = 0 \\ 1 & \text{if } a > 0 \end{cases} \quad (3.11)$$

The first part of (3.8) represents the behaviour of the spring with linear stiffness k . The saturation part (3.9) saturates the force when the maximum friction force F_c is reached and the Coulomb element starts to slide. In the last part of (3.8) the spring element is re-activated when the direction of the deflection changes (3.10). Figure 3.3 shows the resulting hysteretic force characteristic of a Jenkin element. The stiffness k is indicated by the slope of the loop, at the Coulomb friction force F_c the force through whole element, F_{Jenkin} , saturates.

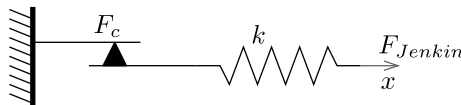


Figure 3.2: Schematic overview Jenkin element.

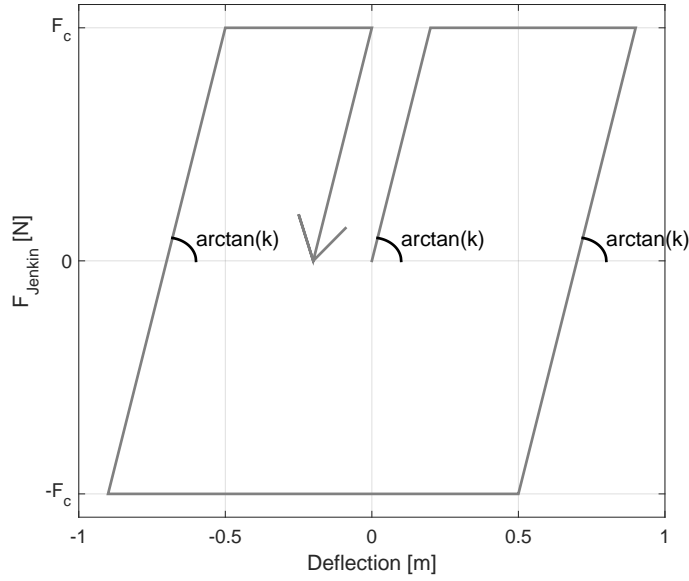


Figure 3.3: Hysteretic force loop of one Jenkin element.

The hysteretic force characteristic of a parallel-series Iwan model consisting of two Jenkin elements and a single spring is shown in figure 3.4. Starting from the origin, for small deflections the stiffness is high. When the first maximum Coulomb friction force is reached, one Jenkin element starts to slide and the stiffness (slope) decreases. When the second maximum friction force is reached, both Jenkin elements slide and the stiffness is further decreased to the stiffness of the single spring. When the direction of the force changes, the Jenkin elements stick and their spring components are reactivated. Increasing the number of Jenkin elements, i.e. the order of the model, results in a more smooth characteristic. This model is defined as a symmetric model, because the behaviour in compression and tension is identical.

The Iwan model in this form cannot describe non-linear softening, hardening or asymmetry behaviour. A non-linear stiffness is introduced to allow for these effects. The non-linear spring force is described by a linear, a quadratic, and a cubic term:

$$F(t) = g_1x(t) + g_2x(t)^2 + g_3x(t)^3 \quad (3.12)$$

The quadratic term ensures asymmetry. Both the quadratic and cubic term may result in softening and/or hardening behaviour. Note that, depending on the set of parameters, the local stiffness may become negative for a certain deflection, which results in unstable behaviour. In this research, however, this does not occur for the practical range of deflections. The non-linear force-displacement relation (3.12) can be applied to all springs in the model or only the single parallel spring. Because the Jenkin elements already start to slide for relatively small deflections, the effect of the non-linear stiffness terms in those springs is small. Figure 3.5 shows the hysteretic loops of the parallel-series Iwan model where only the spring in parallel has been modelled non-linearly. Hysteresis, softening, hardening, and asymmetry are all described by this modified Iwan model. The force through the asymmetric wire rope is given by:

$$F_{wr,asym}(t) = g_1x(t) + g_2x(t)^2 + g_3x(t)^3 + \sum_{i=1}^n F_{Jenkin,i}(t) \quad (3.13)$$

Both the modified Bouc-Wen and Iwan models are able to describe this hysteretic behaviour of the wire rope isolators. However, the advantage of the modified Iwan model is a more physically based structure. The model parameters are directly related to the force-displacement characteristic. This results in a better understanding and a less complex identification process. Therefore, the modified Iwan model is used in the remainder of this thesis.

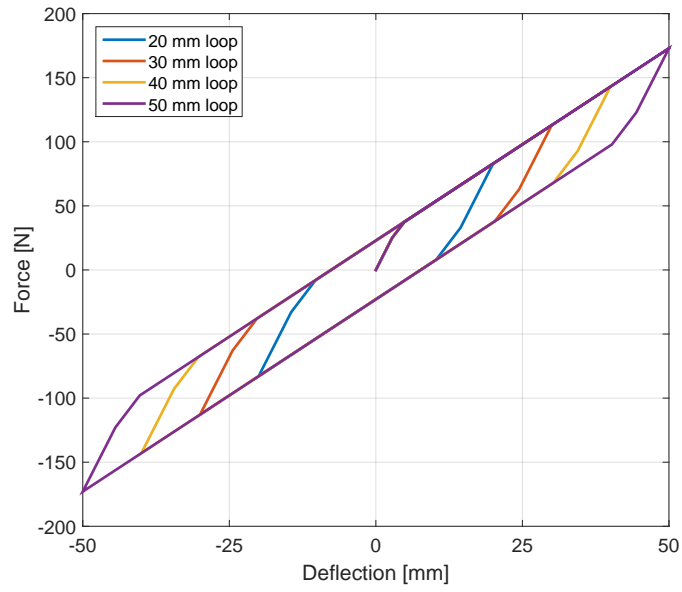


Figure 3.4: Hysteretic loop symmetric Iwan model, order 2.

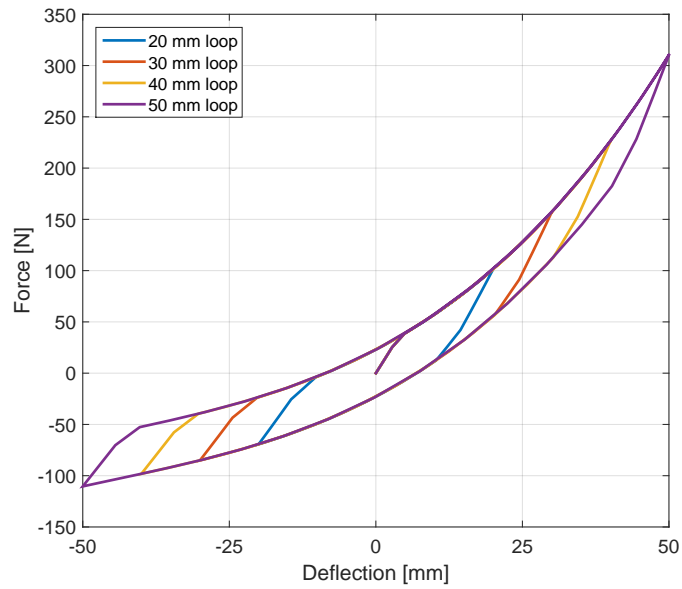


Figure 3.5: Hysteretic loop asymmetric Iwan model, order 2.

3.3 Simulation aspects

Both the hysteretic terms of the Bouc-Wen (3.6) and Iwan model (3.8) are highly non-linear. A pure sign function is non-smooth and contains a jump discontinuity around zero. The sign functions in the models result in continuous, but non-smooth behaviour. Two methods are investigated to implement the behaviour in a simulation model. As stated earlier, only the modified Iwan model is considered.

MATLAB Simulink is a tool to model and simulate dynamical systems in the time domain. Accuracy and robustness are only ensured for continuous and smooth models. Simulink translates a block model into code, which is solved by a standard ODE solver. A standard ODE solver cannot deal with non-smooth functions. It is also possible to write a simulation code in the regular MATLAB environment. Then the model has to be written as a set of coupled first order differential equations. Approximation of the discontinuity by a smooth function enables use of Simulink, but also results in less accuracy and stiff differential equations [36].

There are also several numerical techniques, which can simulate the dynamics of non-smooth systems. For example, the switch model defines a smooth vector field around the discontinuous region and the dynamics can be simulated by switching between the smooth vector fields [36]. Alternatively, using an event-driven approach, it is detected when the discontinuous region is reached or left. Each state is separately solved [36,58]. A completely different and more accurate approach to solve dynamic systems with unilateral constraints is time-stepping. This numerical technique describes the equations of motion on the level of linear and/or angular momentum and hence the discontinuity disappears [24,28,29,36,74,75,81]. To assess its accuracy and efficiency the numerical time-stepping method is further analysed and compared to using MATLAB Simulink in section 3.3.1.

There are several approaches to analyse the response of non-linear systems in the frequency domain (linear analysis methods cannot be directly applied). In this report, the response to harmonic floor excitation will first be simulated in the time domain and will subsequently be described by higher order sinusoidal input describing functions (HOSIDF's) [50,61]. The time response is filtered and each harmonic component, relative to the input frequency, is analysed separately. For non-linear systems this is done for both different input frequencies and input amplitudes. For linear systems only the first harmonic component is non-zero and there is no amplitude dependency. For symmetric non-linear systems (i.e. identical behaviour in compression and tension) only the odd components are non-zero and for asymmetric non-linear systems both odd and even higher harmonic components exist in the output.

In order to reach steady-state, a small amount of parallel (viscous) damping is applied, resulting in an equivalent damping ratio of less than 0.5 %. Physically, this damping accounts for the internal viscous damping of the isolator material, damping by the air, and energy loss via the support.

3.3.1 Parallel Coulomb-spring element

A model of a mass connected to a parallel Coulomb element and a spring under base excitation is considered. The equation of motion of this system is given by:

$$m\ddot{x}_m + kx_m + F_c \operatorname{sgn}(\dot{x}_m - \dot{x}_b) = kx_b \quad (3.14)$$

$$\operatorname{sgn}(a) = \begin{cases} -1 & \text{if } a < 0 \\ [-1, 1] & \text{if } a = 0 \\ 1 & \text{if } a > 0 \end{cases} \quad (3.15)$$

Using time-stepping the sgn function can be described exactly, note that $\operatorname{sgn}(0) \neq \operatorname{sign}(0)$ (3.11). In Simulink the sgn function can only be approximated by a sign block or a smooth hyperbolic function. The output of the sign block is given by:

$$\operatorname{sign}_{\text{block}}(a) = \operatorname{sign}(a) = \begin{cases} -1 & \text{if } a < 0 \\ 0 & \text{if } a = 0 \\ 1 & \text{if } a > 0 \end{cases} \quad (3.16)$$

The sign block is not able to describe the friction force at zero velocity (i.e. stick phase). A smooth hyperbolic function also cannot describe the friction force at zero velocity exactly, but solves the discontinuity problem. Both result in approximations of the actual system behaviour.

For $m = 10 \text{ kg}$, $k = 9000 \text{ N/m}$, and $F_c = 1000 \text{ N}$, the Simulink and time-stepping methods are compared by studying the free vibration response ($x_b = 0$, $x_m(0) = 1$, and $\dot{x}_m(0) = 0$) and the response to harmonic base excitation ($x_b = x \cdot \sin(2\pi ft)$). The same integration time step Δt is used for both methods. For time-stepping, much computational effort is required when the Coulomb element is sticking, i.e. the friction force at zero velocity has to be determined. The computational effort of Simulink does not depend on the state of the friction element. In appendix A.1, some simulation results are shown, table 3.1 lists the integration time step and computational times for both numerical analysis methods and both response types. Note that the time-stepping method employs a convergence parameter r , which influences the computational time. The error criterion tolerance of the fixed point iteration is set to $1 \cdot 10^{-8}$.

In the free vibration response the Coulomb element slips till the vibration is fully damped. As a result, both time-stepping and Simulink provide an accurate response in that phase, as indicated by figure A.1. When the vibration is fully damped, there is a position offset and a non-zero friction force. Time-stepping is able to describe this phenomena, while Simulink is not. Figure A.2 shows the response of the Simulink simulations is slowly drifting to $x_b = 0$. The simulation times are comparable, because the system is mainly in slip. In the base excitation simulations different input frequency and input amplitudes are used. In order to reach steady-state small parallel damping is introduced ($d = 10 \text{ Ns/m}$). The eigenfrequency of the system is 5 Hz . Small excitation causes the system to remain in stick. For $x = 0.1 \text{ m}$ and $f = 1 \text{ Hz}$ the system is in stick, as shown in figure A.3. The top mass response equals the base motion input. Time-stepping is able to accurately describe the system for this kind of behaviour. Simulink is not, the top mass oscillates around the actual response. The simulation time of time-stepping is around 1000 times larger, because it has to determine the friction force at each time instance. For large excitation the system is in slip, this is shown for $x = 0.1 \text{ m}$ and $f = 50 \text{ Hz}$ in figure A.4. Note that the (non-linear) top mass response is not harmonic (i.e. single sinusoidal). Both time-stepping and Simulink accurately describe the system's behaviour for this kind of input. The simulation time of time-stepping is 10 times higher compared to Simulink.

Table 3.1: Comparison computational times simulation.

	Method	Time [s]
Free vibration $\Delta t = \frac{1}{2048} \text{ s}$	Time-stepping, $r = 0.1$	0.44
	Time-stepping, $r = 0.5$	0.15
	Time-stepping, $r = 1.0$	0.12
	Simulink	0.30
Base excitation $\Delta t = \frac{1}{512f} \text{ s}$	Time-stepping, $r = 0.5$	160 - 17000
	Simulink	14

When the system is in slip both time-stepping and Simulink provide accurate results, Simulink is 10 times faster. Time-stepping can also accurately describe the behaviour in stick, but is very time consuming. Considering both accuracy and computational effort, Simulink should only be used when an approximation of the behaviour suffices. For high accuracy, time-stepping should be used.

3.3.2 Parallel series Iwan model

In the parallel series Iwan model the Jenkin elements are placed in parallel with a spring element (figure 3.1). In a Jenkin element, a Coulomb element is placed in series with a spring. Basically, in a Jenkin element, stick-slip behaviour causes saturation on its spring force, as described by (3.8). In principle, this behaviour can be simulated by Simulink. The discontinuity in the friction force disappears and a C^0 continuous force description remains. In many cases this kind of non-linearity can be solved by Simulink, with a properly chosen solver and solver settings. The time consuming time-stepping approach is not required to gain accuracy. Hence, the parallel series Iwan model is used for further analysis.

3.4 Vibration and shock analysis

Apart from the small parallel viscous damper, the modified Iwan model consists of spring and Coulomb elements only. This means the response of the isolator is only input amplitude and not input frequency dependent (i.e. when the viscous damping is neglected). In contrary, a dynamical system which includes a mass and wire rope isolator is both amplitude and frequency dependent. A base excited system consisting of a top mass and a wire rope isolator is shown in figure 3.6. In sections 3.4.1 and 3.4.2, 3D frequency-input amplitude-response amplitude diagrams will be used to visualize the machine response to harmonic floor vibrations (in steady-state). The response to shock is examined by time simulations of a conditioned free fall in section 3.4.3. The performance criterion for shock is the maximum absolute acceleration of the mass, called the rest shock level.

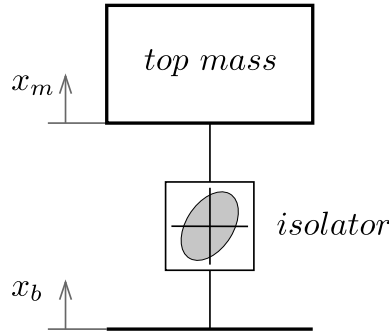


Figure 3.6: Schematic overview isolation system.

Systems with both symmetric (figure 3.4) and asymmetric (figure 3.5) characteristics are used. The parameters of both the symmetric and asymmetric systems are listed in appendix A.2. The mass of 8 kg is chosen to achieve a resonance frequency of around 5 Hz for small amplitude input. A wire rope model of order 2 is analysed. To give an impression of the model description, the differential equations to describe a order n_{wr} symmetric wire rope system are given by:

$$\begin{aligned}
 m\ddot{x}_m &= -\left(k_{wr,0}(x_m - x_b) + \sum_{i=1}^{n_{wr}} F_{Jenkin,i}\right) \\
 \dot{F}_{Jenkin,1} &= \frac{1}{2}k_{wr,1}(\dot{x}_m - \dot{x}_b)[\text{saturation} + \text{re-activation}] \\
 &\vdots \\
 \dot{F}_{Jenkin,n_{wr}} &= \frac{1}{2}k_{wr,n_{wr}}(\dot{x}_m - \dot{x}_b)[\text{saturation} + \text{re-activation}]
 \end{aligned} \tag{3.17}$$

The detailed equations to describe the saturation and re-activation of the Jenkin elements are presented in section 3.2. In sections 3.4.1 and 3.4.2, the system is excited by harmonic (i.e. single sinusoidal) input in time simulations. The initial conditions are set to zero, i.e. $x_m = 0$ and $\dot{x}_m = 0$. The unfiltered peak-peak/2 response of the machine position to the base position, x_m/x_b , is analysed. For a linear system this would resemble the transmissibility. In our case of a non-linear system the term transmissibility can no longer be used. An excitation frequency range from 1 Hz to 100 Hz is analysed. The symmetric system is analysed over an excitation amplitude range from 10^{-5} m to 10^0 m. To ensure stability of the asymmetric wire rope model, the maximum excitation amplitude for the asymmetric isolation system is limited to 10^{-2} m. Furthermore, HOSIDF's can be used to get insight in detailed non-linear aspects of the response behaviour. To efficiently and accurately determine the HOSIDF's, a fixed integration time step Simulink solver is used: the ode3 solver.

3.4.1 Vibrations: symmetric wire rope isolator behaviour

First a system with the symmetric wire rope isolator as characterized in figure 3.4 is analysed. Figure 3.7 shows the frequency-amplitude magnitude diagram of the peak-peak/2 value. The frequency dependency is similar to a linear system; stiffness dominated behaviour for low frequencies, a resonance at 5 Hz, followed by a -2 mass slope for high frequencies. The equivalent stiffness of the wire rope isolator decreases for higher input amplitudes, this causes a decrease in the resonance frequency. Around the stiffness transition region friction forces result in effective damping.

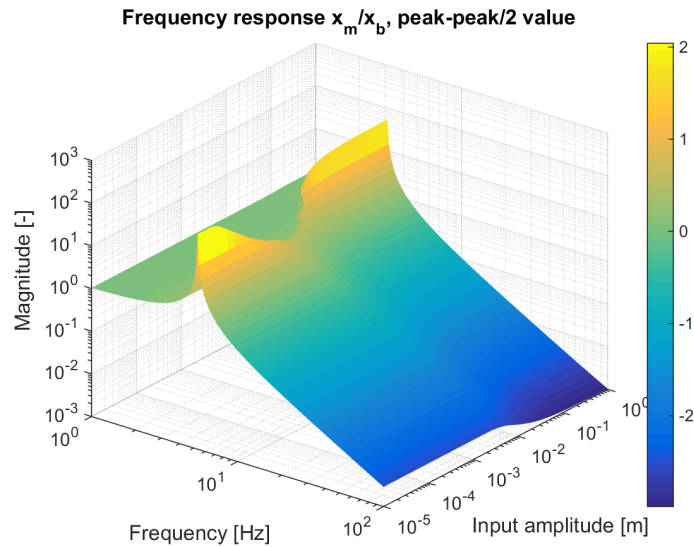


Figure 3.7: Frequency-amplitude diagram, magnitude peak-peak/2, symmetric.

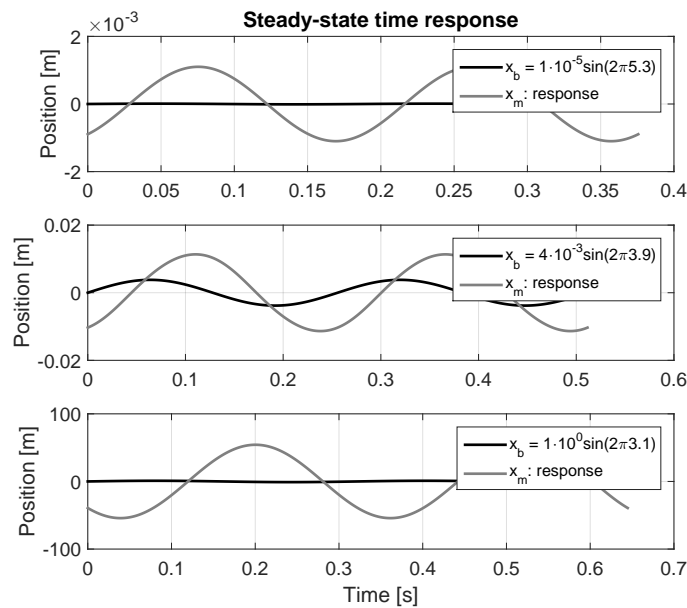


Figure 3.8: Steady-state time histories top mass position for different inputs, symmetric.

The steady-state time histories of three specific inputs are shown in figure 3.8. Two periods of input x_b and the steady-state response x_m are shown for inputs at the resonance frequency for low, intermediate, and high excitation amplitudes. A first analysis shows all responses are close to harmonic. The top and bottom plots, corresponding to respectively a low and a high excitation amplitude, indicate very light damping. The middle plot, corresponding to an intermediate excitation amplitude, shows heavy damping. These observations underline the analysis of the peak-peak/2 diagram in figure 3.7.

Figure 3.9 shows the frequency-amplitude magnitude diagram of the first harmonic component of the response. The magnitude is very similar to the peak-peak/2 magnitude, since the first harmonic is dominant and the system is locally close to linear. This was already indicated by the analysis of the peak-peak/2 magnitude diagram (figure 3.7) and time histories (figure 3.8). For low excitation amplitudes only the internal damping affects the isolator properties near resonance. For higher excitation amplitudes (in the transition region) the friction elements become active. However, when even further increasing excitation amplitudes the influence of the friction damping decreases again. The hysteretic loops are stretched, and thus the effective damping decreases.

This is further analysed in a 2D diagram, where three excitation amplitude cross sections of the magnitude and phase are shown, see figure 3.10. The magnitude-frequency diagram shows a clear overview of the aforementioned excitation amplitude dependent effects, in addition, the resonance frequency (effective stiffness) decreases significantly for increasing excitation amplitude, and the friction damping is only effective for intermediate excitation amplitudes. The phase transition around the resonance frequency for intermediate amplitudes is asymmetric. Below the resonance there is stick, and above the resonance the friction elements slip.

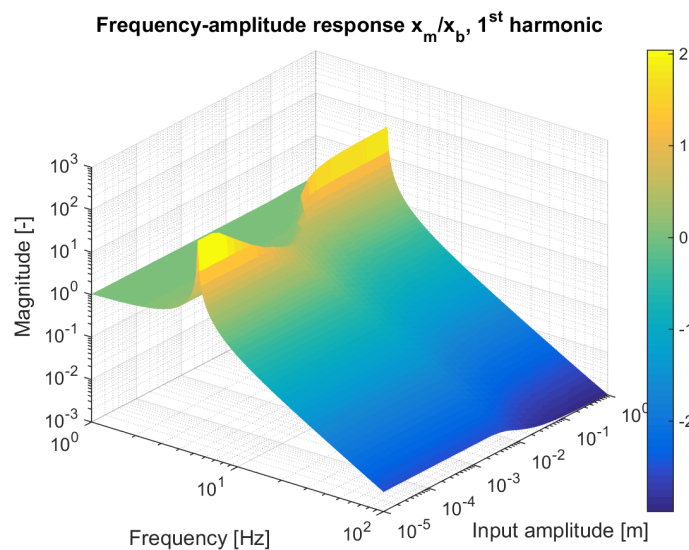


Figure 3.9: Frequency-amplitude diagram, magnitude 1st harmonic, symmetric.

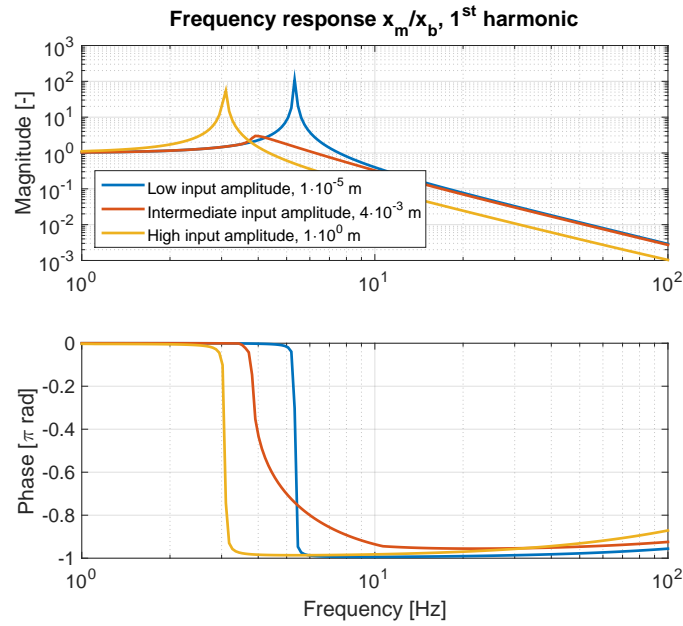


Figure 3.10: Frequency response diagram, 1st harmonic, symmetric.

For a symmetric system the even higher harmonic components are zero (appendix A.3). The odd components indicate symmetric non-linearity. Figure 3.11 shows the top view of the magnitude diagram of the third harmonic response component. For low excitation amplitudes, the system behaviour is linear. Increasing the excitation amplitude leads to local slip around the resonance frequency; only in that area friction elements start to slide. The non-linear region broadens for increasing excitation amplitude. From a certain amplitude of around $1 \cdot 10^{-1} \text{ m}$ global slip occurs. Higher even and odd harmonics show similar as respectively the second and third harmonic, their magnitudes decrease gradually. Further, note that no bifurcations are detected in the time simulations.

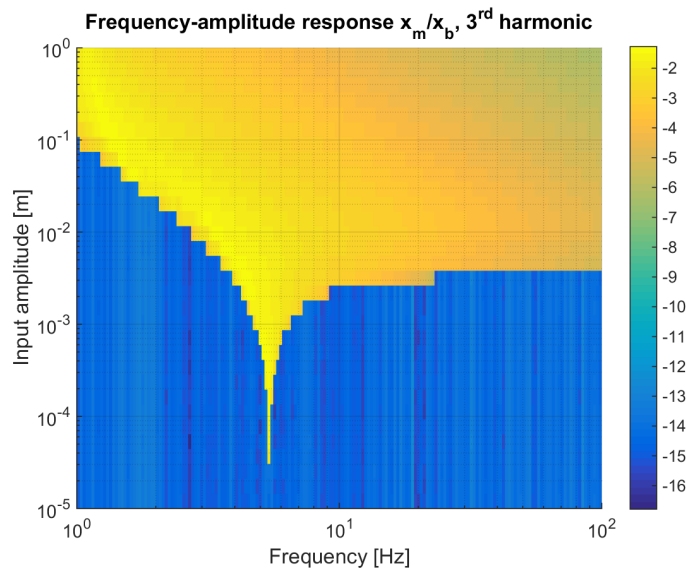


Figure 3.11: Frequency-amplitude diagram, magnitude 3rd harmonic, symmetric.

3.4.2 Vibrations: asymmetric wire rope isolator behaviour

A similar analysis is done for a system with the asymmetric wire rope isolator with the characteristic as shown in figure 3.5, the mass is still equal to 8 kg . Note that a different excitation amplitude range is used compared to the symmetric analysis, because the non-linear stiffness characteristic becomes unstable for too large (and unrealistic) excitation amplitudes. The 3D magnitude diagram of the peak-peak/2 value, shown in figure 3.12, shows similar trends as seen in the symmetric system (figure 3.7). For low excitation frequencies, the system is stiff, followed by a resonance near 5 Hz and a -2 mass slope for higher excitation frequencies. The resonance frequency is decreasing for increasing excitation amplitude, whereas the damping is increasing. These phenomena are, as mentioned before, caused by the slipping of the friction elements. A further increase in excitation amplitude results in a decrease in damping. The hysteretic loops are stretched, and thus the effective damping (related to the ratio of the surface of the hysteretic loop and the total vibrational energy) decreases.

Similar to the the steady-state time plots of the symmetric system in figure 3.8, time histories of simulations of the asymmetric system are shown in figure A.6 in appendix A.4. The time histories underline the analysis of the peak-peak/2 magnitude. The top plot, corresponding to a low excitation amplitude, indicates very light damping. The response in the middle plot, corresponding to an intermediate amplitude, shows heavy damping. A further increase in excitation amplitude, shown in the bottom plot, leads to an decrease in damping again. Further, note that the response for all three excitations is close to harmonic.

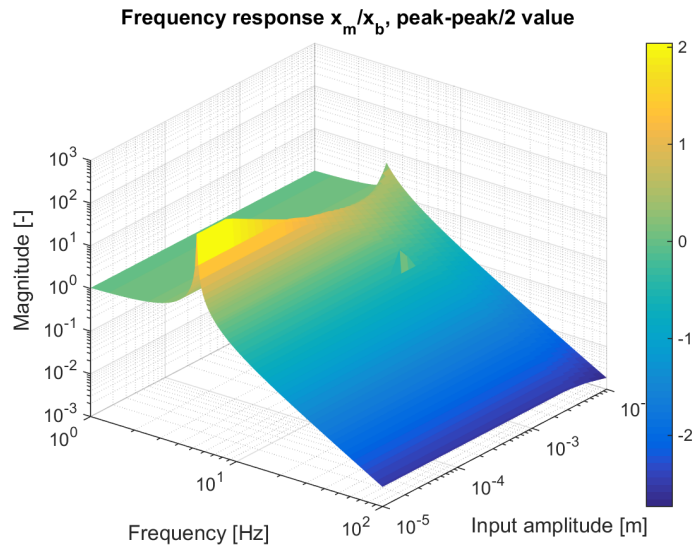


Figure 3.12: Frequency-amplitude diagram, magnitude peak-peak/2, asymmetric.

The magnitude of the first harmonic component is shown in figure 3.13. The magnitude of this first harmonic is very similar to the peak-peak/2 magnitude in figure 3.12. Together with the analysis of the the time histories (figure A.6), this indicates that the first harmonic is dominant. Figure 3.14 shows 2D frequency magnitude and phase diagrams of the first harmonic component for three excitation amplitudes. Clearly, the resonance frequency decreases for increasing excitation amplitude, due to the decrease in effective stiffness. Again, there is significant damping for intermediate excitation amplitudes and to smaller extent for high excitation amplitudes. Note that the intermediate and high excitation amplitude values are relatively close. The asymmetric phase transition around the resonance frequency indicates a stick-slip transition. For low excitation amplitudes, there is no friction induced damping. Here, the small amount of damping comes from the internal viscous damping.

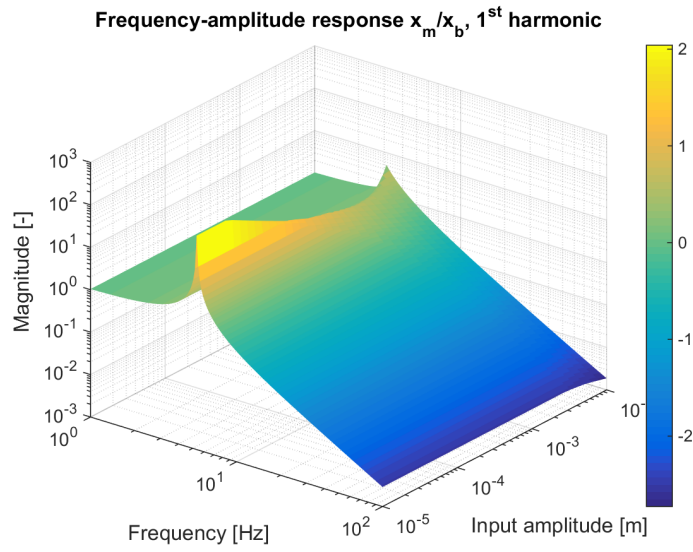


Figure 3.13: Frequency-amplitude diagram, magnitude 1st harmonic, asymmetric.

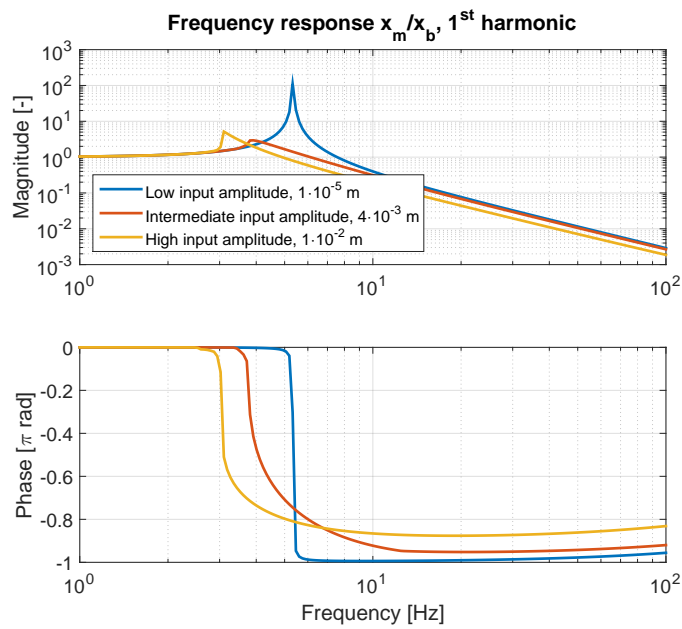


Figure 3.14: Frequency response diagram, 1st harmonic, asymmetric.

The non-linear asymmetric behaviour results in both even and odd harmonic response components. Top views of the magnitude diagrams of the second and third harmonic are shown in figure 3.15 and figure 3.16, respectively. Around the resonance frequency and for higher excitation amplitudes the influence of higher order harmonics increases. The isolator force and deflection are maximal for these inputs. A small isolator force and consequently a small deflection results in a less asymmetric response (magnitudes of even components are small) and sticking friction elements (magnitudes of higher order odd components are small). Some extra peaks appear at lower frequencies: a peak at $1/2$ the resonance frequency in both the second and third component and a peak at $1/3$ of the resonance frequency in the third harmonic component is observed. These peaks may result in superharmonic resonances. However, these are not observed in figure 3.12. Note the the the peaks at the system resonance are amplitude dependent due to the stick-slip behaviour. The peaks at $1/2$ and $1/3$ of the resonance frequency are amplitude independent, because here the system is still in stick (for this amplitude range).

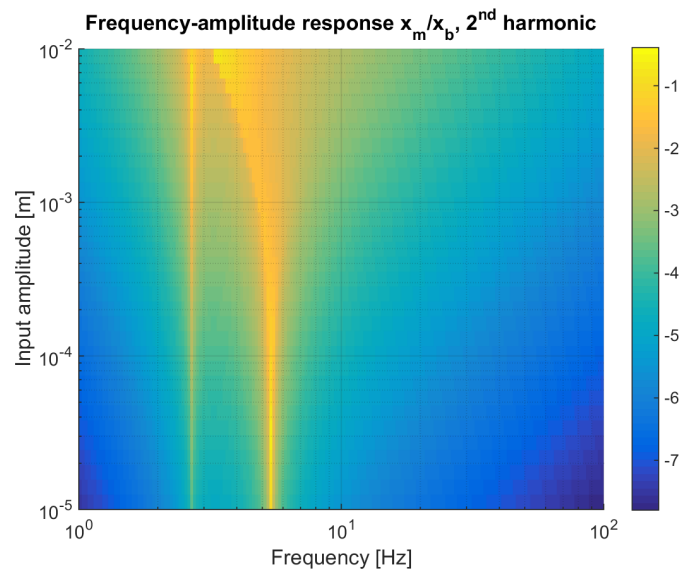


Figure 3.15: Frequency-amplitude diagram, magnitude 2nd harmonic, asymmetric.

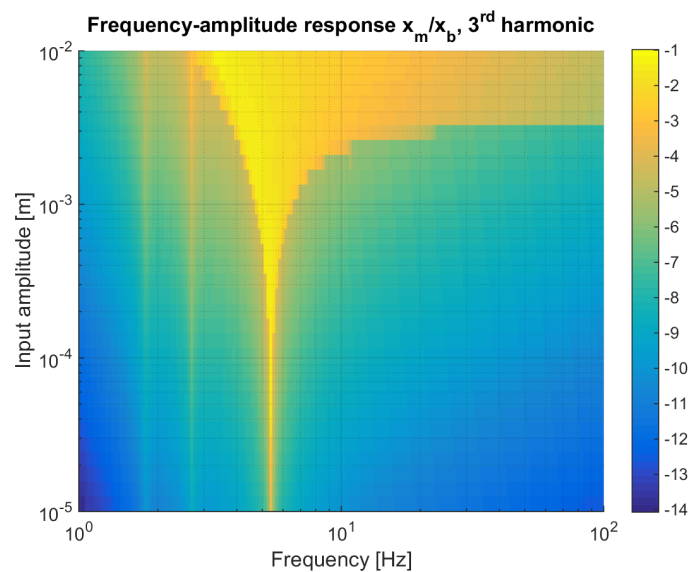


Figure 3.16: Frequency-amplitude diagram, magnitude 3rd harmonic, asymmetric.

Figure 3.12 shows an interesting small peak response at an input of around 11 Hz and $1 \cdot 10^{-3} \text{ m}$, just before the stick-slip transition (indicated by figure 3.16). The peak appears near twice the resonance frequency. A detailed time analysis for this input shows a half subharmonic response. The lowest harmonic component in the response is not the input frequency, but half that frequency. This is illustrated by the steady-state time signals of the position, velocity, and acceleration of the top mass over two periods of input, see figure 3.17. Clearly, the base frequency of the top mass response is half that of the floor input.

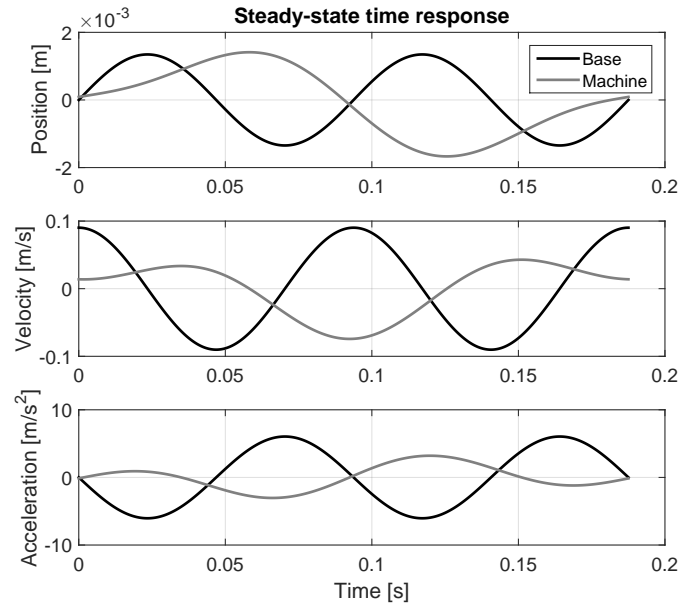


Figure 3.17: Steady-state time response top mass.

A frequency domain analysis of the top mass displacement (position) time response (i.e. the top plot of figure 3.17) results in figure 3.18. Indeed, next to a constant bias (due to hysteresis and asymmetry), harmonics, and superharmonics response components, also half subharmonic components are present. The magnitude of higher order harmonics generally decreases with increasing order. The half subharmonics only exist for specific excitation amplitude and frequency combinations, i.e. only locally there is periodic doubling. This is caused by the asymmetric softening and hardening behaviour. Similar behaviour occurs in dynamic systems with piecewise linear stiffness [15, 79]. Figure 3.19 shows the frequency-amplitude magnitude diagram of the half subharmonic component. The existence of this component is clearly local. The increase in damping for higher excitation amplitudes destroys the half subharmonic response.

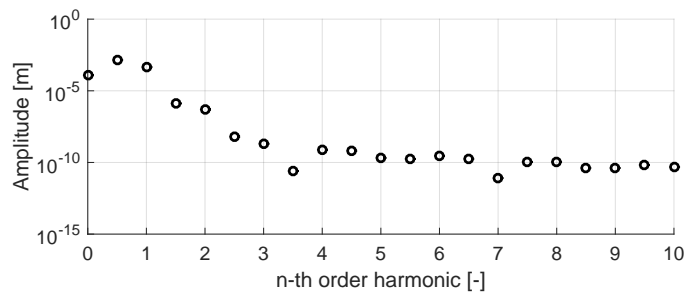


Figure 3.18: Frequency spectrum of position time response of the top mass.

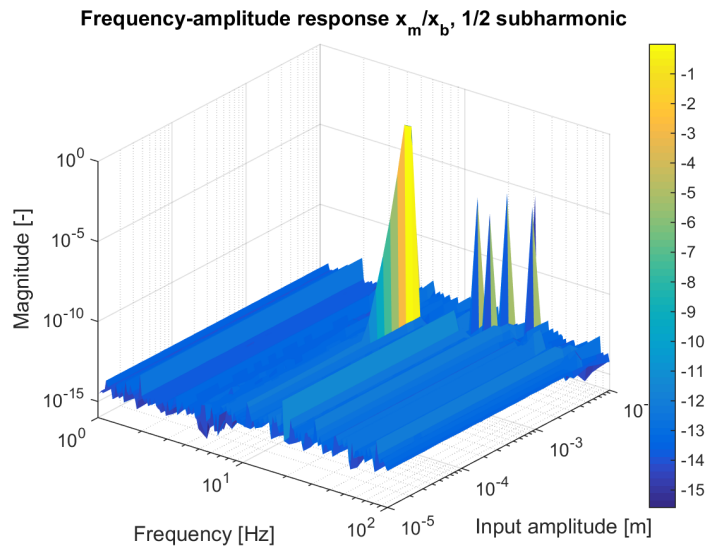


Figure 3.19: Frequency-amplitude diagram, magnitude half subharmonic, asymmetric.

3.4.3 Shock

The shock absorption properties are examined by a conditioned free fall. The performance criterion is the maximum acceleration of the top mass, which is directly related to the force exerted to the latter. Using the energy balance of the system, the drop height of the free top mass h can be related to its initial velocity v_0 :

$$mgh = \frac{1}{2}mv_0^2 \quad (3.18)$$

$$v_0 = -\sqrt{2gh} \quad (3.19)$$

In the coming time simulations, the base is assumed to stand still, whereas the top mass is given an initial velocity according to (3.19), as shown in figure 3.20. Note that in real-life experiments the isolator itself has a mass and a second bottom mass exist below the isolator during the free fall. This second mass causes the isolator to relax and oscillate during the free fall. This also results in a small change in the initial velocity at moment of impact, which is however only significant for small drop heights. These effects are not included in the simulations in this section. Therefore, this free fall simulation is referred to as conditioned free fall.

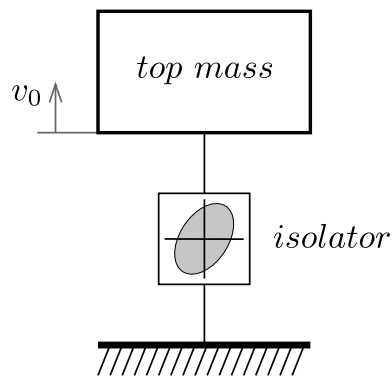


Figure 3.20: Schematic overview isolation system for shock.

For lightly damped symmetric systems the critical time is the moment when the mass reaches its bottom death point, at this time both the deflection and the acceleration are maximal. For undamped linear systems the maximum acceleration can be determined by the energy conservation law:

$$\frac{1}{2}mv_0^2 = \frac{1}{2}kx_0^2 \quad (3.20)$$

First the maximum deflection, x_0 , is determined:

$$x_0 = \sqrt{\frac{m}{k}}v_0 = \frac{1}{\omega_0}v_0 \quad (3.21)$$

Then, using the equation of motion:

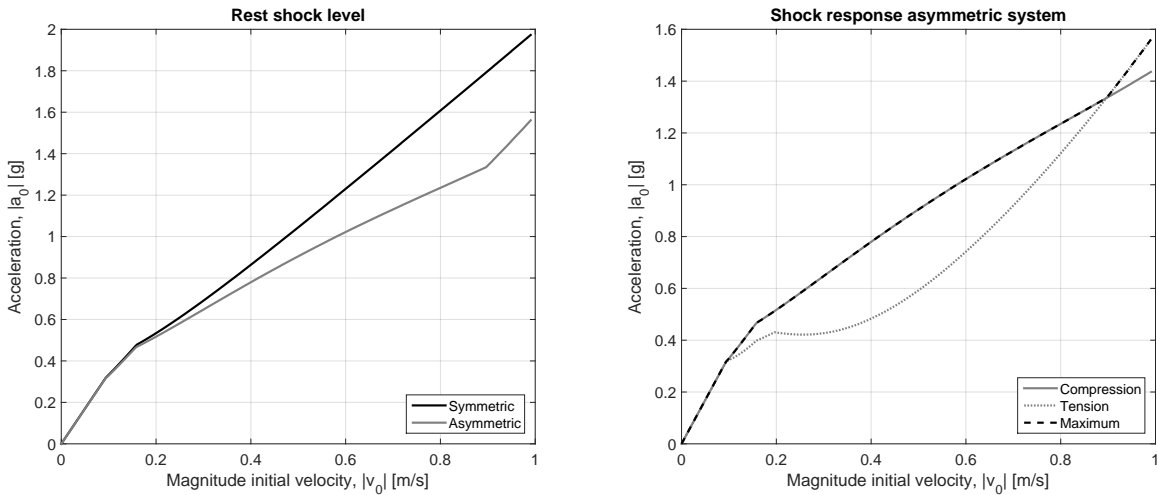
$$ma = -kx \quad (3.22)$$

the maximum acceleration, a_0 , is determined:

$$a_0 = -\omega_0v_0 \quad (3.23)$$

The maximum acceleration is proportional with the initial velocity and the eigenfrequency, while the maximum deflection is proportional with the initial velocity and the inverse of the eigenfrequency. For linear systems, there is always a trade-off in minimizing acceleration and deflection.

A drop height range up to 5 cm is analysed for both the symmetric and asymmetric wire rope system. Figure 3.21a shows the maximum absolute acceleration $|a_0|$, i.e. the rest shock level, as function of the absolute initial velocity $|v_0|$. For velocities up to 0.09 m/s the systems behave like a linear system: the response is proportional to the initial velocity. For higher velocities, the friction elements start to slide and the equivalent local stiffness decreases. Above 0.15 m/s the maximum acceleration is linear with the initial velocity for a symmetric wire rope isolator. For the asymmetric isolator this line flattens, which is caused by the softening behaviour during compression. Slipping and softening during compression are obviously beneficial for shock absorption, because these phenomena result in energy dissipation and a decreased maximum absolute acceleration.



(a) Rest shock level as function of velocity, symmetric and asymmetric system.

(b) Maximum absolute acceleration in tension and compression, asymmetric system.

Figure 3.21: Shock response wire rope systems.

Above an initial velocity of around 0.9 m/s , the rest shock level of the asymmetric system starts to increase again. Below this velocity the acceleration in the compression phase is critical. Above this velocity the acceleration in the subsequent tension phase is critical. The asymmetric hardening during tensioning results in less deflection, however in a higher force and acceleration. Figure 3.21b shows the maximum absolute acceleration in both compression and tension for the asymmetric case. Above 0.9 m/s not enough energy is absorbed during compression and the acceleration in tension becomes critical.

A decrease in acceleration obviously leads to an increase in deflection. Figure A.7 in appendix A.5 shows the maximum deflection in compression as function of velocity; as expected the deflection of the asymmetric system is larger. The relation between the rest shock level and the drop height is also visualized in appendix A.5 (figure A.8); in the linear case, the acceleration is dependent on the square root of the drop height (see (3.19) and (3.23)). In the non-linear case, friction and softening induced effects are already visible at small drop heights.

3.5 Summary

The Bouc-Wen and Iwan models have been discussed in detail. The conventional versions of these models describe only a part of the non-linear hysteretic behaviour. Modified versions of both the Bouc-Wen and Iwan models are needed to describe hysteresis, softening and hardening, and asymmetric behaviour of wire rope isolators. The more physical background of the Iwan model results in a less complex identification process. Because of the parallel series structure of the Iwan model, MATLAB Simulink and regular ODE solvers can be used to model and analyse the behaviour. Therefore, no advanced numerical techniques are required.

A floor excited wire rope isolation system is assessed for both harmonic (i.e. single sinusoidal) and shock excitation. Firstly, time domain responses of the system excited by harmonic floor displacement are calculated. From the resulting steady-state responses, the peak-peak/2 and HOSIDF's are determined. These results are visualized in 3D frequency-excitation amplitude-magnitude response diagrams. The stiffness of a wire rope isolator initially decreases for increasing response amplitude. In this transition region the friction induced damping of the wire rope spring is very effective. Bifurcations or coexisting stable solutions are not expected in the steady-state behaviour, due to the significant amount of damping in the feasible response amplitude range.

Shock behaviour is examined by a conditioned free fall. The relaxation and dynamics of the wire rope spring, during the actual fall are not considered in the simulations. The characteristic decrease in stiffness and increase in damping basically are the key advantages of using wire rope isolators to absorb shocks. The rest shock level is lowered, while there is significant damping to damp the oscillation.

In the next two chapters the behaviour of respectively an elastomer and a hybrid isolator are analysed. Again, the isolation systems are assessed with respect to both vibrational and shock behaviour.

Chapter 4

Elastomer isolators

Viscoelastic materials are well known and frequently used vibration isolators. Cross-linked polymers, i.e. rubbers, are used in the majority of isolation systems. In contrast to friction based wire rope isolators, their behaviour is not amplitude dependent. However, they are more dependent on environmental conditions such as temperature. In general, viscoelastic isolators are considered more effective for small amplitude inputs, i.e. vibrations, whereas friction based isolators are considered to be more effective for higher input amplitudes, i.e. shocks.

This chapter involves the modelling of an elastomer isolator and the analysis of its vibration and shock isolation capacity. The system analysis is done similar to the analysis of the wire rope isolators in section 3.4.

In the first section of this chapter, viscoelastic behaviour is characterized. In section 4.2, detailed insight in the modelling of viscoelastic materials is given. In the third section, the vibrational and shock behaviour of an isolation system with an elastomer mount is analysed. In the last section, a short summary of the obtained results and insights is provided.

4.1 Viscoelasticity

Viscoelastic isolators are in most cases made out of rubberlike polymer materials, called elastomers. Viscoelasticity encompasses both viscous and elastic behaviour. Elasticity ensures stiffness, whereas due to the viscosity energy is dissipated. Viscoelastic behaviour is frequency and temperature dependent. Important characteristics of viscoelastic materials are relaxation and creep. Excitation amplitude dependency is mainly related to the design and geometry of the isolator and is not considered here.

The viscoelastic behaviour can be described by a frequency dependent complex Young's modulus, consisting of a storage modulus (real part) and a loss modulus (imaginary part). The magnitude of the complex modulus and the ratio of the imaginary and real part are measures for respectively stiffness and damping. Elastomer isolators are only effective in the glass transition region, where the loss modulus and the loss factor are non-zero. Change in the operating temperature can drive the polymer towards the glassy or liquid region. In this thesis, the temperature is considered to be constant, so the glass transition frequency region is fixed. Two other important phenomenon in viscoelasticity are creep and relaxation. Relaxation describes the change in stress under constant deformation and creep the change in deformation under constant loading. The timescale of vibrations and shocks is in the order of seconds or milliseconds, whereas the timescale of creep and relaxation is in the order of days or months. In the actual design of a viscoelastic isolator creep and relaxation must be considered, but this is not needed for dynamical analysis [45, 64, 65, 77].

4.2 Modelling

In section 2.2, already some viscoelastic models were briefly discussed for describing the complex frequency dependent Young's modulus: GHM models [20], fractional derivative models [3,62], and standard mechanical models such as generalized Maxwell models [57, 65]. The first two types of models are empirical and defined in the frequency domain. Because of their non-linear character there may be not a straight forward method to convert them to the time domain. The standard mechanical models consist of series and parallel combinations of linear spring and dashpot elements and can be described both in the frequency and time domain. Further, the physical character of these models simplifies the model parameter identification process.

4.2.1 Standard mechanical models

The most elementary standard mechanical models consist of one spring and one dashpot element. The series representation is described by Maxwell. Voigt describes the parallel decomposition. Figure 4.1 shows both the Maxwell and Voigt model [57, 65].

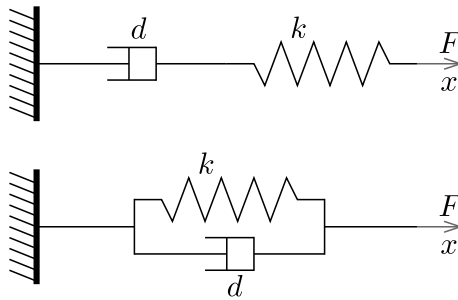


Figure 4.1: Top: Maxwell model, below: Voigt model.

The complex Young's modulus of viscoelastic material is directly related to the stiffness by the isolator dimensions, for a geometry with a homogeneous cross section. The complex stiffness of the Maxwell model can be described linearly in the Laplace domain:

$$k(s)^* = \frac{kds}{ds + k} \quad (4.1)$$

where k and d represent the stiffness of the spring and constant of the dashpot, respectively. The complex stiffness of the Voigt model is given by:

$$k(s)^* = ds + k \quad (4.2)$$

In general, viscoelastic fluids are described by the Maxwell model, while viscoelastic solids are described by the Voigt model. However, these elementary models give only a first approximation of the material behaviour. The use of multiple components increases the accuracy of the model [57, 65].

A viscoelastic elastomer isolator is considered to behave like a viscoelastic solid. The more complex generalized Maxwell model for viscoelastic solids (also referred to as multiple standard model) consists of n Maxwell elements and a single spring in parallel, as shown in figure 4.2. The complex stiffness of this model is given by:

$$k(s)^* = k_{el,0} + \sum_{i=1}^n \frac{k_{el,i}d_{el,i}s}{d_{el,i}s + k_{el,i}} \quad (4.3)$$

The loss factor of this viscoelastic model, the measure of dissipation, is given by:

$$\eta(s) = \frac{Im(k(s)^*)}{Re(k(s)^*)} \quad (4.4)$$

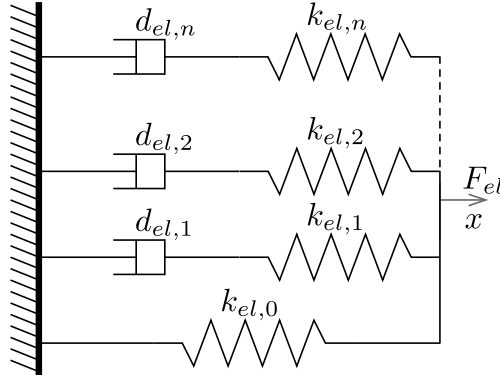


Figure 4.2: Schematic overview Generalized Maxwell model.

Moreover, for a loss factor up to 0.4, an equivalent dimensionless damping ratio can be estimated [65]:

$$\zeta \approx \frac{1}{2}\eta(\omega_0) \quad (4.5)$$

The characteristic complex stiffness and loss factor of a generalized Maxwell model are shown in figure 4.3. Approximately one Maxwell element is needed to describe one decade of frequency. For the model shown, 10 elements are used. For low frequencies the viscoelastic material behaves like a soft spring without dissipation. In figure 4.2 this is represented by the single spring with stiffness $k_{el,0}$. For high frequencies the material is very stiff. Again, there is no dissipation. All spring elements are active and the dashpots are fixed. Only in the intermediate frequency region the dashpot elements are active and energy is dissipated. In figure 4.3 the effect of shifting damping region is visualized. Note that not only the damping region, but also the stiffness curve is shifted. Both material choice and temperature determine the glass transition region and thus the effective damping region in terms of frequency. Note that the response of this (linear) viscoelastic model is not input amplitude dependent.

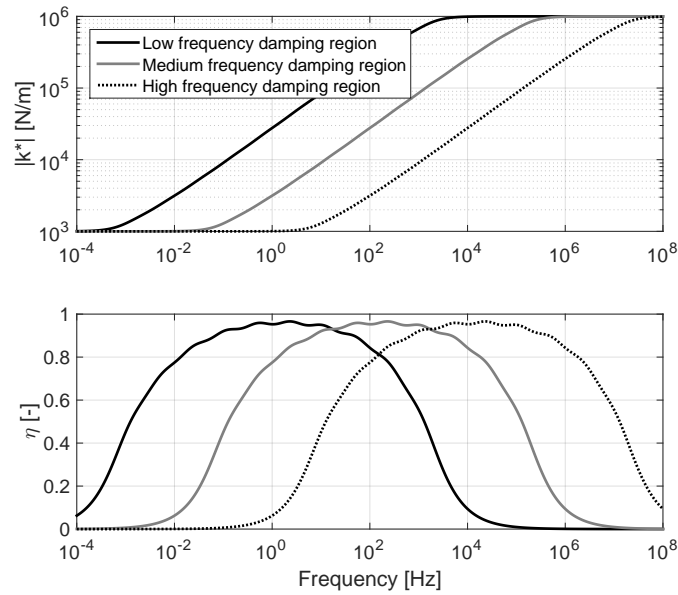


Figure 4.3: Complex stiffness and loss factor, generalized Maxwell model $n = 10$.

Figure 4.3 can also be interpreted as the Bode diagram of a viscoelastic isolator. The complex stiffness (4.3) is the transfer function of the deflection to force. The loss factor is a scaled phase: a loss factor equal to zero represents a phase of zero, a loss factor of one corresponds with a phase of 45 deg:

$$\eta = \tan(\phi) \quad (4.6)$$

Finally, the equation of motion of a floor excited elastomer isolation system (in the frequency domain) is given by:

$$ms^2 X_m(s) = -\left(k_{el,0} + \sum_{i=1}^n \frac{k_{el,i} d_{el,i} s}{d_{el,i} s + k_{el,i}}\right) (X_m(s) - X_b(s)) \quad (4.7)$$

4.3 Vibration and shock analysis

In this section, the dynamical analysis of elastomer isolators in a single degree of freedom (SDOF) vibration isolation system is considered, similar to the analysis of the wire rope isolation system in section 3.4. A floor excited isolation system consisting of a base, viscoelastic isolator, and top mass is considered. For a linear elastomer isolator, the vibration analysis can be done in the frequency domain and visualized in a Bode diagram. Since the isolator system is linear, there is no amplitude dependency. The shock simulations of this SDOF system are done in the time domain by a conditioned free fall. Shock response behaviour is assessed by the rest shock level.

The location of the glass transition region in terms of frequency is determined by environmental conditions, e.g. temperature and the specific choice of material. Therefore, different isolator configurations, with shifted glass transition region (in frequency), are analysed with respect to floor vibrations and shocks. The three different characteristics as presented in figure 4.3 are used. The mass (5 kg) is chosen to achieve an eigenfrequency of around 5 Hz for solid grey characteristic in figure 4.3. Note that the eigenfrequency of the solid black and dotted black characteristics differs. The other model parameters are listed in table B.1 in appendix B.1.

4.3.1 Vibrations

The three curves in the Bode diagrams figure 4.4 show the transmissibility (frequency response x_m/x_b) of the floor excited isolation system with elastomer isolator characteristics corresponding to the three elastomers in figure 4.3. This figure gives an overview of the behaviour over a broad frequency range. The eigenfrequency is in the high damping range of the solid black and the solid grey characteristic of figure 4.3, but in the low damping range of the dotted black characteristic.

Shifting the glass transition region from medium frequencies (solid grey curve) to lower frequencies (solid black curve) results in higher stiffness at 5 Hz and consequently a higher eigenfrequency (i.e. the mass is kept constant). For the solid black curve, the eigenfrequency is still heavily damped. The damping region (-1 slope) ends at 10^4 Hz. For higher frequencies this is more profitable in terms of isolation (-2 slope). When the whole damping region is located below the eigenfrequency, at the resonance and for higher frequencies only the behaviour of a mass-spring system would be observed.

A glass transition frequency region at higher frequencies (dotted black curve) obviously results in a lower eigenfrequency. The eigenfrequency is just within the damping region and the damping is low. This also leads to -1 slope in the frequency region up to 10^8 Hz, which is clearly not profitable for isolation. Damping is only desired around the eigenfrequency.

When comparing the three curves in figure 4.4, it can be observed that there is a trade-off between good isolation at low and high frequencies.

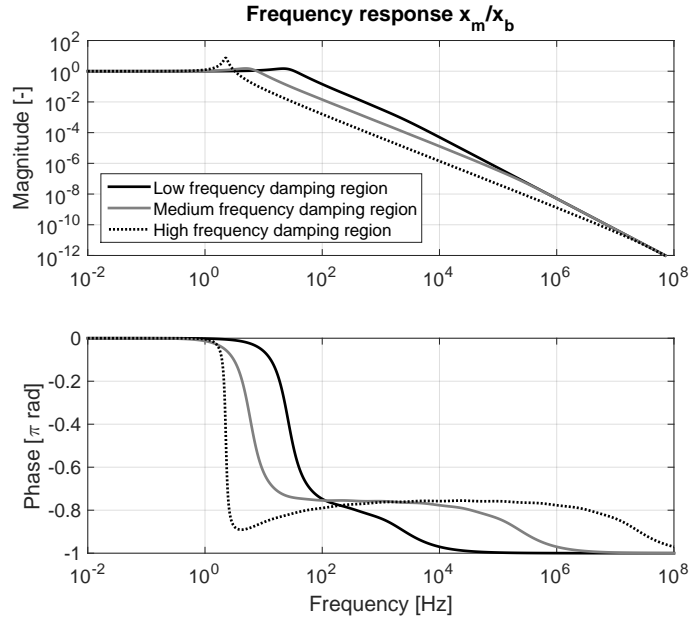


Figure 4.4: FRF elastomer isolation system, using generalized Maxwell model $n = 10$.

4.3.2 Shock

Time simulations, where the base is standing still and the machine has an initial (drop) velocity v_0 , are made to examine the shock performance of the viscoelastic damper. Note again that the relaxation and dynamics in air are not considered in these simulations, so these simulations slightly differ from a real free fall. The initial velocity is again determined from the drop height using the energy balance (3.19), as discussed in section 3.4.3. Again, the three viscoelastic system damper with the complex stiffness characteristics from figure 4.3 and corresponding frequency response functions from figure 4.4 (top mass 5 kg) are used in this analysis.

The rest shock level $|a_0|$ as function of the absolute initial velocity $|v_0|$ is shown in figure 4.5. Because the elastomer isolation system is linear and the damping is relatively low, the dependency of the rest shock level on the initial velocity is close to proportional. The stiffness and eigenfrequency are not changing for higher excitation amplitudes or drop heights. For an undamped system the slope of the curve of the rest shock level versus absolute initial velocity equals the undamped eigenfrequency (3.23). The elastomer isolation systems exhibit light damping, the slope for these systems approximates the damped eigenfrequency of the system. In contrast, the maximum deflection is decreasing with increasing eigenfrequency. In terms of rest shock level and deflection there is always a trade-off for linear systems.

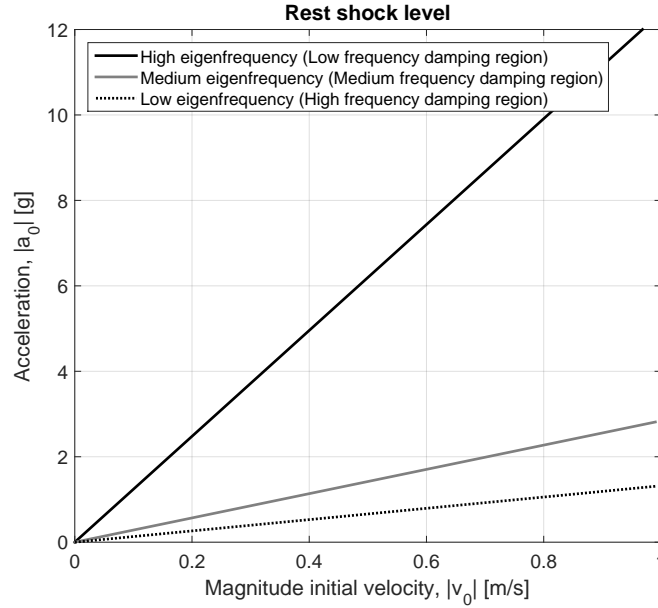


Figure 4.5: Maximum absolute acceleration free fall as function of velocity.

4.4 Summary

The behaviour of viscoelastic materials is strongly frequency dependent. Different dynamical models describe this behaviour properly. For the dynamical analysis in this thesis the model must be applicable in both the frequency and time domain. Standard mechanical models are linear in the frequency domain, so these models can directly be transformed to the time domain. The generalized Maxwell model consists of several series spring-dashpot components in parallel and is a suitable model to describe an elastomer isolator. Because of the linear character of this viscoelastic model, the system properties do not differ for vibrations (small amplitudes) and shocks (large amplitudes). Temperature dependency, excitation amplitude dependency, and relaxation and creep are not considered in this model, because in this report constant temperature is assumed, large deflections of the viscoelastic material are not considered, and the time scale in vibration and shock behaviour is much smaller than the time scale in relaxation and creep.

Viscoelastic damping is only effective in the frequency dependent glass transition region. A shift of this region affects the resonance frequency, the resonance damping, and high frequency isolation. These effects can be nicely shown in a linear Bode diagram. The goal is designing a system with only damping around the resonance, in order to preserve the isolation properties. The damping region, i.e. the glass transition frequency region, is mainly determined by the physical material properties and temperature.

Time simulations of a conditioned free fall give a good insight in the response to shock; the damped eigenfrequency is the primary system property which affects the response. The (almost) proportional relation between rest shock level and initial velocity is mainly characterized by the damped eigenfrequency.

The next chapter describes the modelling and simulation of a hybrid isolator system.

Chapter 5

Hybrid isolators

In chapters 3 and 4, the modelling and dynamic analysis for respectively a wire rope and an elastomer isolator is presented. The analysis showed that the wire rope isolators are performing well in terms of vibrations isolation and shock absorption for large deformations, whereas the viscoelastic elastomers are capable of damping and isolation of small amplitude vibrations. It is expected that placing a wire rope isolator and elastomer mount in series results in a beneficial combination of the shock and vibration isolation properties of the wire rope isolator, and the damping and vibration isolation properties of the viscoelastic elastomer. This hybrid isolator is modelled and analysed in this chapter.

The isolator models used in chapters 3 and 4 have to be combined in order to perform a dynamical analysis of the hybrid damper. The obtained analysis results are used to compare the individual isolators and the hybrid isolator. The analysis approach of the hybrid isolation system is equal to the approach in previous chapters.

In the first section of this chapter, the modelling of a hybrid damper is described. Section 5.2 focusses on some simulation issues with respect to the hybrid isolation system. In section 5.3, the analysis of the vibration and shock behaviour of the hybrid isolator are presented. In the last section, the obtained results are summarized.

5.1 Modelling

The concept of this hybrid composition is the utilization of the (large response signal) shock absorbing properties of the wire rope isolator and the (small response signal) damping properties of the elastomer isolator. For vibrations with low amplitudes the wire rope spring remains in its stick regime and is stiff with low damping. The resonance damping is generated by the (less stiff) elastomer. For high amplitude input and response (i.e. shock) the wire rope spring can generate much friction induced damping. In the latter situation, the wire rope isolator has to be dominant, so its stiffness has to be lower compared to the elastomer. Because the behaviour of the wire rope isolator is non-linear and its stiffness is amplitude dependent, these apparently contradictory requirements can be satisfied.

The Iwan model of the wire rope spring and the generalized Maxwell model of the elastomer isolator have to be coupled. Figure 5.1 gives a schematic overview of the coupled system. A small intermediate mass is introduced, which may represent (part of) the masses of the isolators and the coupling mass in the real setup. Because the intermediate coupling mass is relatively small compared to the top mass, its dynamics affect the system behaviour only for high frequencies. Moreover, for low frequencies the equation of motion of the intermediate mass effectively represents a force equilibrium. The differential equations describing the dynamics of the hybrid system, with a generalized Maxwell model of order n_{el} and symmetric Iwan model of order n_{wr} , are given by:

$$\begin{aligned}
m\ddot{x}_m &= -\left(k_{el,0}(x_m - x_{in}) + \sum_{i=1}^{n_{el}} k_{el,i}(x_{el,i} - x_{in})\right) \\
\dot{x}_{el,1} &= -\frac{k_{el,1}}{d_{el,1}}(x_{el,1} - x_{in}) + \dot{x}_m \\
&\vdots \\
\dot{x}_{el,n_{el}} &= -\frac{k_{el,n_{el}}}{d_{el,n_{el}}}(x_{el,n_{el}} - x_{in}) + \dot{x}_m \\
m_{in}\ddot{x}_{in} &= \left(k_{el,0}(x_m - x_{in}) + \sum_{i=1}^{n_{el}} k_{el,i}(x_{el,i} - x_{in})\right) - \left(k_{wr,0}(x_{in} - x_b) + \sum_{j=1}^{n_{wr}} F_{Jenkin,j}\right) \\
\dot{F}_{Jenkin,1} &= \frac{1}{2}k_{wr,1}(\dot{x}_{in} - \dot{x}_b) [\text{saturation} + \text{re-activation}] \\
&\vdots \\
\dot{F}_{Jenkin,n_{wr}} &= \frac{1}{2}k_{wr,n_{wr}}(\dot{x}_{in} - \dot{x}_b) [\text{saturation} + \text{re-activation}]
\end{aligned} \tag{5.1}$$

where $x_{el,i}$ is a state of the generalized Maxwell model. The detailed equations to describe the saturation (3.9) and re-activation (3.10) of the Jenkin elements are presented in section 3.2.

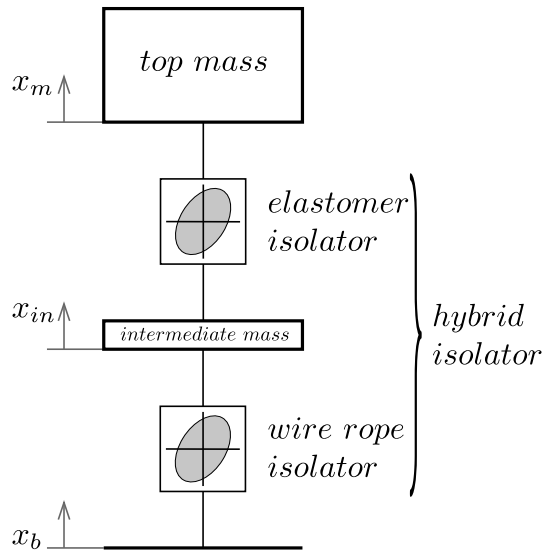


Figure 5.1: Schematic overview hybrid isolation system.

5.2 Simulation aspects

The hybrid model consists of the Iwan model (parameter values of table A.1 in appendix A.2), the medium frequency damping region generalized Maxwell model (parameters values of table B.1 in appendix B.1), and two masses. The top mass (2 kg) is chosen to achieve a first resonance frequency of 7.5 Hz for small response amplitudes. The intermediate mass equals one percent of the top mass, i.e. 0.02 kg. This results in a second resonance frequency of approximately 120 Hz. The equations of motion (5.1) are directly implemented in the regular MATLAB environment. Variable integration time step solvers in the regular MATLAB environment are able to determine the response at user defined time instances, where variable step solvers in Simulink are not. To efficiently filter the time response to determine the HOSIDF's, a fixed time step of the response is needed. In the regular MATLAB environment, this can be achieved by both fixed and variable integration time step solvers (i.e. all MATLAB solvers).

With $n_{el} = 10$ and $n_{wr} = 2$, the first order system model consists of 16 states in total. The generalized Maxwell model describes the elastomer behaviour over a broad frequency range and the time scales of its states have a very wide distribution. Therefore, equation (5.1) with our parameter values is very stiff. MATLAB provides stiff (implicit) solvers (i.e. ode15s, ode23s, ode23t, ode23tb, and ode15i) to

simulate (5.1) in a reasonable timeframe. However, numerical problems arise at moments in time where the friction elements start to slip. The C^0 continuous behaviour of the Jenkin elements cannot be handled by the implicit solvers, because they use backward differentiation. A hyperbolic tangent function is used to smoothen the stick-slip transitions. After optimization, the stiff ode15s solver from MATLAB is most efficient and used for the simulations in next section.

5.3 Vibration and shock analysis

The hybrid system model is analysed for vibrations and shocks, just as has been done for the individual wire rope spring and the individual elastomer isolator. Both the symmetric and the asymmetric system are analysed.

5.3.1 Vibrations: symmetric hybrid isolator behaviour

Firstly, the vibrational response of the symmetric system to a harmonic input is analysed. Figure 5.2 shows the frequency-excitation amplitude diagram of the peak-peak/2 value. Isolation properties are preserved over the whole excitation amplitude range. The resonance frequency is decreasing for increasing input amplitude, because then the friction elements start to slide and stiffness is lost. For high excitation amplitudes, the damping is less. In this region, the wire rope isolator is dominant. Apparently, the friction damping is less effective than the viscoelastic damping (for this set of model parameters). At low excitation amplitudes the resonance is significantly damped. Here, the elastomer is dominant due to its low stiffness. The hybrid isolator ensures both resonance damping and vibration isolation over a wide input range.

The steady-state time histories of three specific inputs are shown in figure 5.3. Two periods of input x_b and the steady-state response x_m are shown for inputs at the resonance frequency for low, intermediate, and high excitation amplitudes. A first analysis shows all responses are close to harmonic. From top to bottom, a slight decrease in resonance damping is observed. These observations underline the analysis of the peak-peak/2 diagram in figure 3.7.

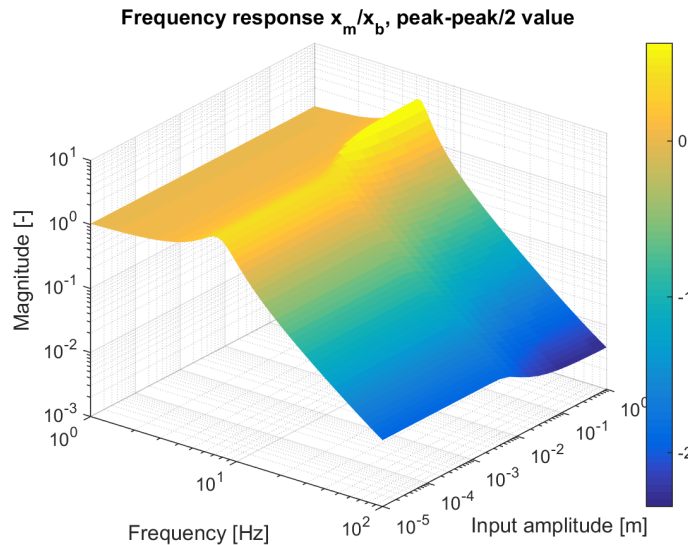


Figure 5.2: Frequency-amplitude diagram, magnitude peak-peak/2, symmetric.

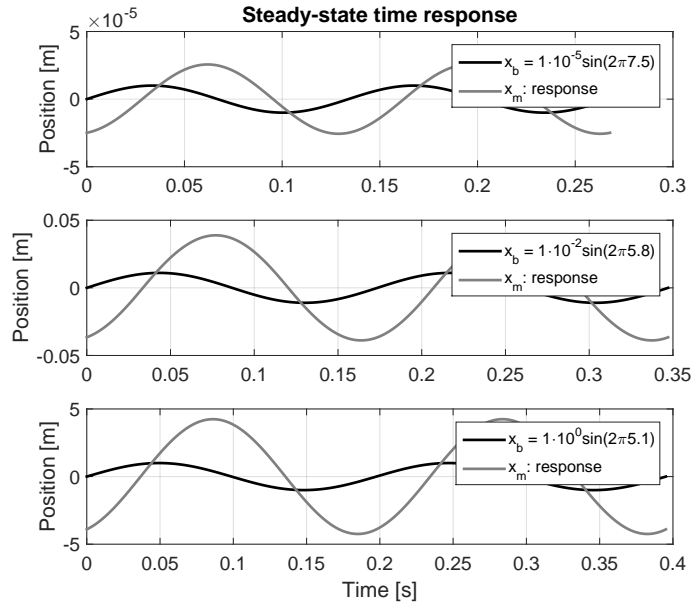


Figure 5.3: Steady-state time histories top mass position for different inputs, symmetric.

The magnitude diagram of the first harmonic component is shown in figure 5.4. Comparing figure 5.4 with figure 5.2, leads to the conclusion that the first harmonic is dominant in the vibrational response. Amplitude cross sections of the magnitude and phase of the first harmonic component are shown in figure 5.5. The system exhibits both resonance damping and vibration isolation, independent of the input amplitude. The stiffness, indicated by the resonance frequency, and the resonance damping are decreasing for increasing excitation amplitude.

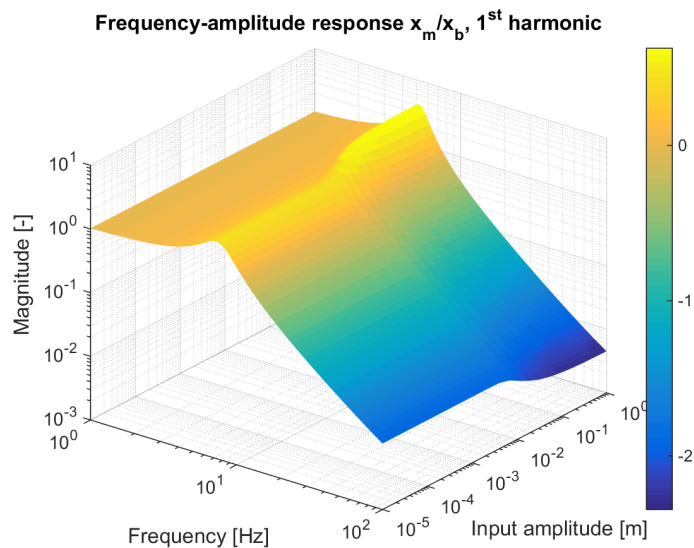


Figure 5.4: Frequency-amplitude diagram, magnitude 1st harmonic, symmetric.

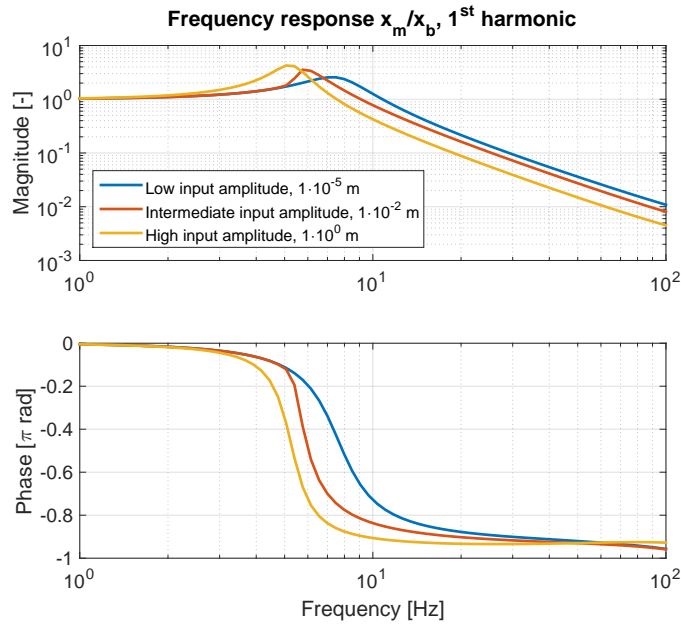


Figure 5.5: Frequency response diagram, 1st harmonic, symmetric.

The magnitudes of the even components are negligible for this symmetric system (appendix C.1). The magnitudes of the third component (top view shown in figure 5.6) are also negligible for low input amplitudes, where all friction elements stick and the behaviour is linear. For high input amplitudes, the friction elements start to slip. The local slip for lower input amplitudes around the resonance frequency seen in the wire rope isolation system (figure 3.11) is not present in this hybrid configuration. In the low input amplitude region, for the hybrid isolator, the elastomer dampens the response around the resonance frequency.

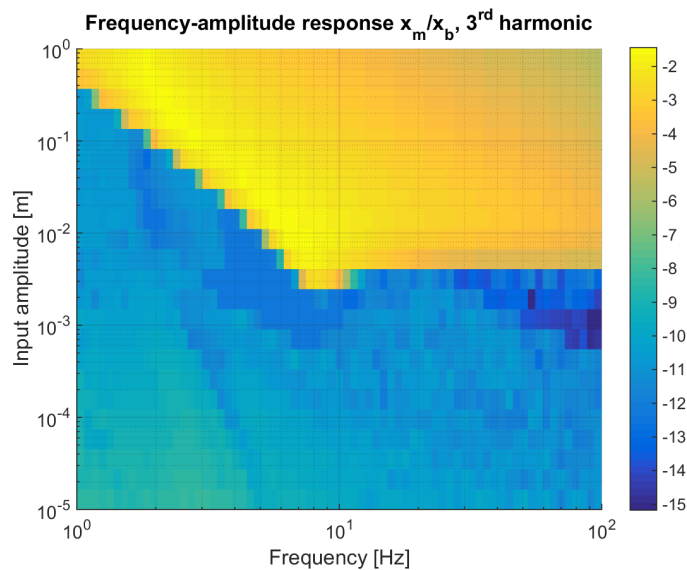


Figure 5.6: Frequency-amplitude diagram, magnitude 3rd harmonic, symmetric.

The low excitation amplitude behaviour, where the friction elements stick, can be described by a linear model in the frequency domain. Figure 5.7 shows the Bode diagram of the complex stiffness of the isolators. The elastomer behaviour is clearly recognized. The linear model of the wire rope isolator consists of an effective spring and viscous damper in parallel. The viscous damping value is low, there is no significant dissipation below 100 Hz. The elastomer and the wire rope stiffness in series results in the hybrid characteristic. The phase diagram clearly shows two separate damping regions around 1 Hz and 10⁴ Hz; in between the damping level is significantly lower.

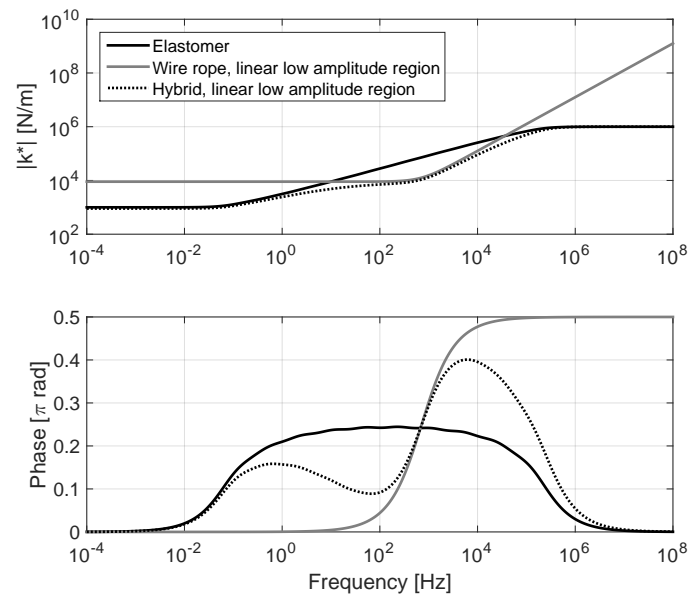


Figure 5.7: Bode diagram hybrid isolator components for small input amplitude (linear behaviour).

The hybrid complex stiffness is used in an isolation system. Figure 5.8 shows the transmissibility FRF of the hybrid system over a broad frequency range, assuming an input amplitude small enough to guarantee linear behaviour. The resonance is significantly damped, followed by a -2 slope. Around 10⁴ Hz the damping increases again. Note that the system response from 1 to 100 Hz is most significant. At higher frequencies, higher internal dynamics, which are not modelled, affect the behaviour significantly.

The behaviour of the hybrid isolation system is summarized for both low and high input amplitudes in the low, the resonance, and the high input frequency (around 100 Hz) regions in table 5.1.

Table 5.1: Summary hybrid behaviour.

INPUT	Low frequency	Resonance frequency	High frequency
Small amplitude	Elastomer dominant, due to relative low stiffness	Elastomer dominant; significant damping	Wire rope dominant; isolation ensured
High amplitude	Elastomer dominant, due to relative low stiffness	Wire rope dominant; relatively less damping	Wire rope dominant; isolation ensured

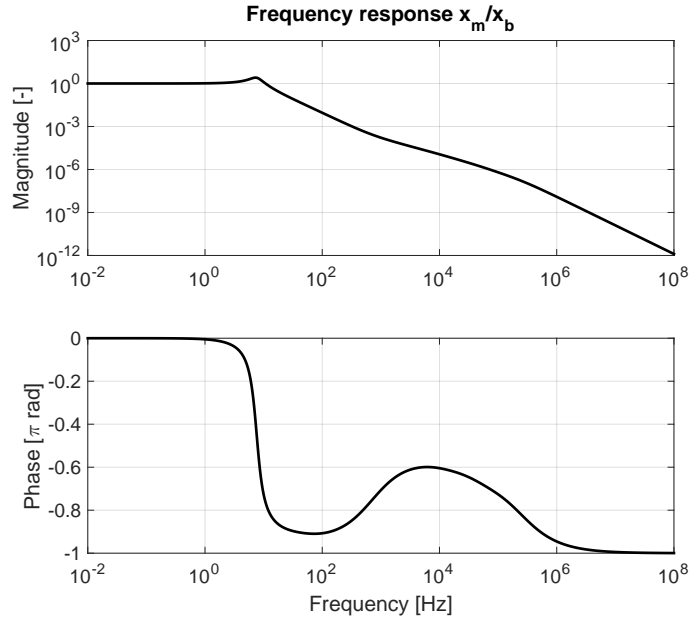


Figure 5.8: Transmissibility diagram hybrid isolation system for small input amplitude (linear behaviour).

5.3.2 Vibrations: asymmetric hybrid isolator behaviour

The harmonic floor excitation is also applied to the asymmetric hybrid system. Note that a different amplitude range is used, due to loss of stability of the asymmetric wire rope isolation model for high amplitude responses. The behaviour for low input amplitudes is not completely linear, in contrast the linear response of the symmetric hybrid system. For the asymmetric case, still the friction element stick. However, the asymmetric model contains a non-linear spring. For higher excitation amplitudes, the friction elements start to slip and the resonance frequency decreases. The damping at smaller excitation amplitudes is determined by the elastomer. As the wire rope stiffness decreases for increasing input amplitude, the wire rope isolator becomes dominant and consequently the damping decreases (the friction damping is less effective than the viscoelastic damping). Three time histories are shown in figure C.2 in appendix C.2. Similar to the symmetric analysis, the response is close to harmonic and an decrease in damping is observed for increasing input amplitude.

The magnitude diagram of the first order harmonic is shown in figure 5.10. The similarities with the peak-peak/2 value (figure 5.9) indicate that the first component is dominant. The isolation properties are consistent over the whole excitation amplitude range due to the influence of the wire rope component. For low excitation amplitudes, isolation is even ensured in combination with significant resonance damping. Cross sections of the magnitude and phase of the first harmonic component are plotted in a 2D frequency response diagram for three different input amplitudes, see figure 5.11. Again it can be seen that the resonance frequency and the resonance damping decrease for increasing input amplitude. For lower input amplitudes, the elastomer is dominant. The influence of the wire rope isolator increases with increasing excitation amplitude. The wire rope contribution positively affects isolation over whole amplitude range.

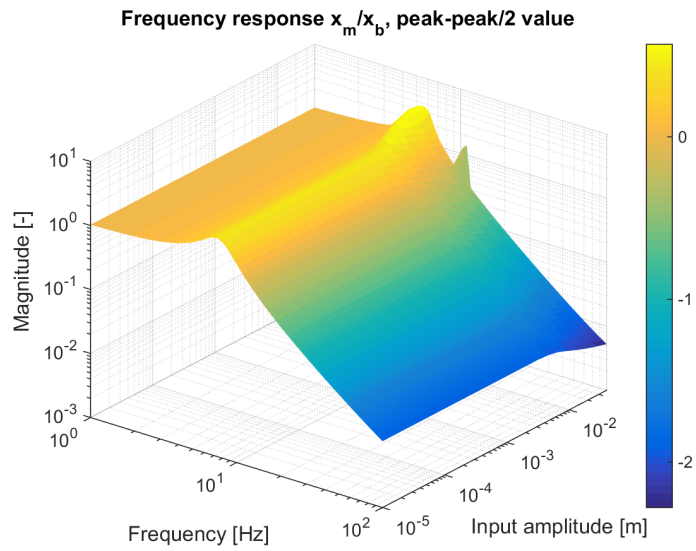


Figure 5.9: Frequency-amplitude diagram, magnitude peak-peak/2, asymmetric.

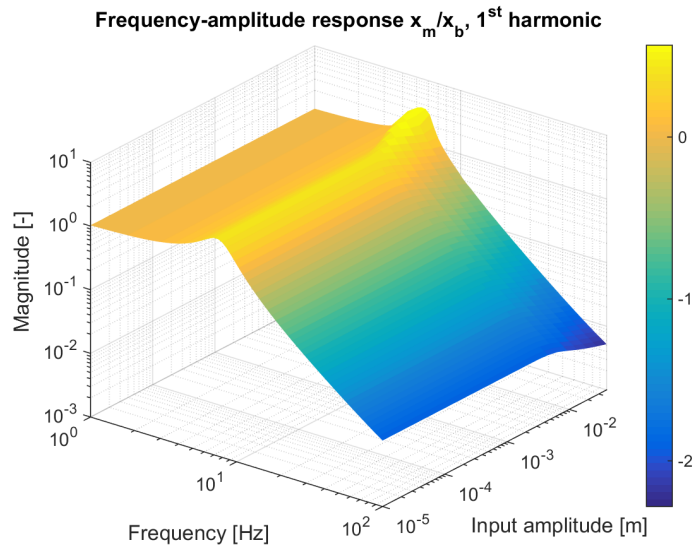


Figure 5.10: Frequency-amplitude diagram, magnitude 1st harmonic, asymmetric.

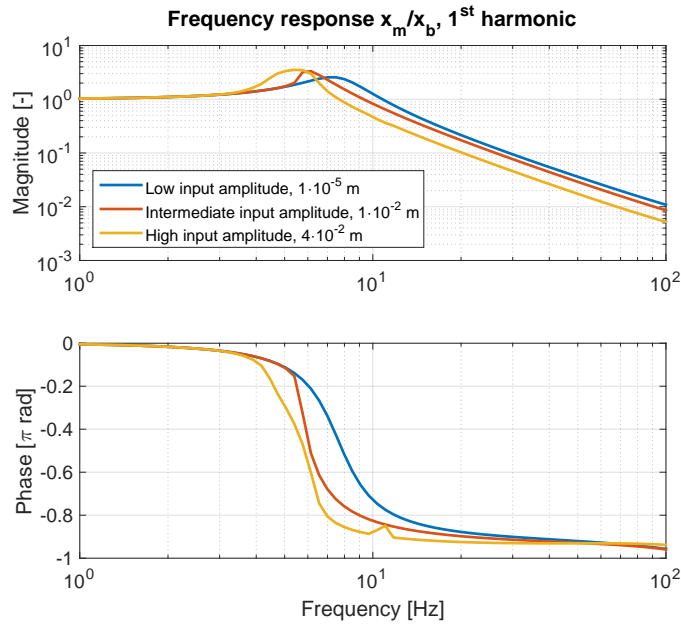


Figure 5.11: Frequency response diagram, 1st harmonic, asymmetric.

The non-linear stick-slip phenomena and softening, hardening, and asymmetric characteristics of the wire rope spring result in the presence of higher order harmonic response components. Top views of the magnitude diagrams of the second and third harmonic are shown in figure 5.12 and figure 5.13. The even components are mainly related to the asymmetry, their contribution is frequency and amplitude dependent. Their magnitude is increasing around the resonance frequency and for increasing input amplitude. The odd harmonics are mainly related to the friction induced behaviour and, therefore, their magnitude is small for low frequencies and/or small input amplitudes. The friction elements slip for higher frequencies and/or input amplitudes, where there is an abrupt magnitude increase. For smaller input amplitudes the magnitude of the third harmonic component is already gradually increasing, due to the asymmetry. There is no local slip around the resonance frequency for smaller input amplitudes.

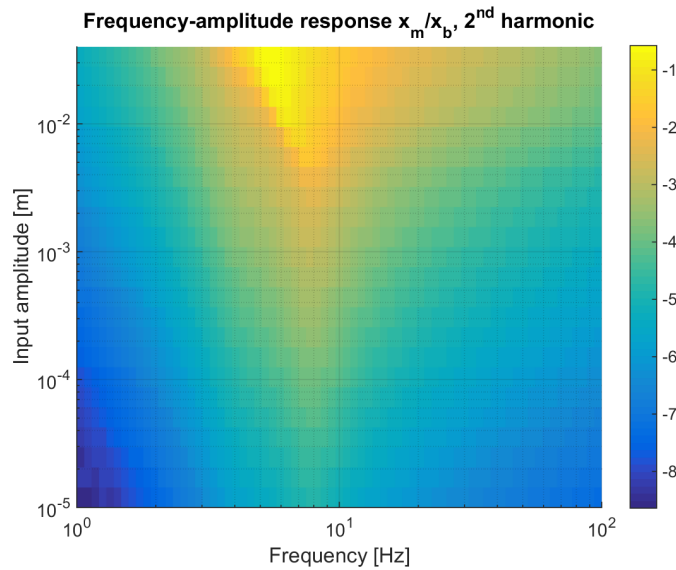


Figure 5.12: Frequency-amplitude diagram, magnitude 2nd harmonic, asymmetric.

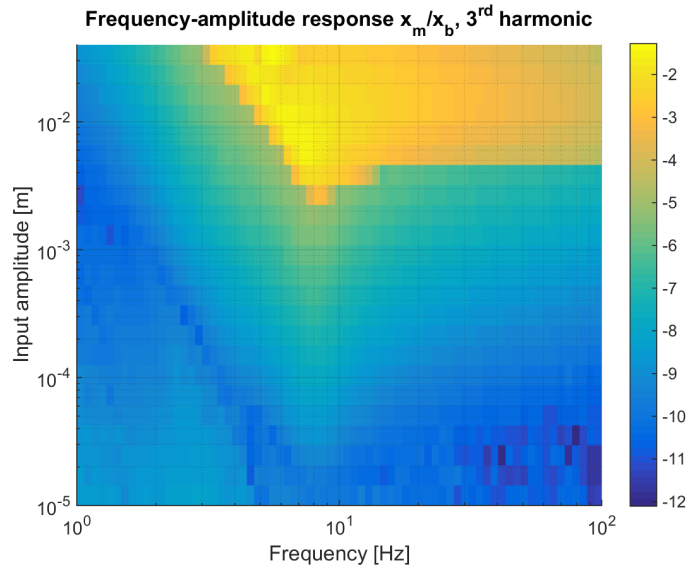


Figure 5.13: Frequency-amplitude diagram, magnitude 3rd harmonic, asymmetric.

A small peak in the response magnitude appears in all harmonic components around 10 *Hz* at the maximum excitation amplitude, i.e. at about twice the resonance frequency. Further analysis shows half subharmonics in the response signal. This half subharmonic resonance was also seen in simulations with the separate asymmetric wire rope isolation system in section 3.4.2. It is caused by the asymmetric behaviour. Figure 5.14 shows the 3D magnitude diagram of the half subharmonic. The occurrence of half subharmonics is clearly a local effect, which can possibly also occur for higher input amplitudes than presented in figure 5.14. As mentioned in section 3.4.2, the wire rope isolator exhibits significant damping, therefore this local phenomenon is not expected in practical application.

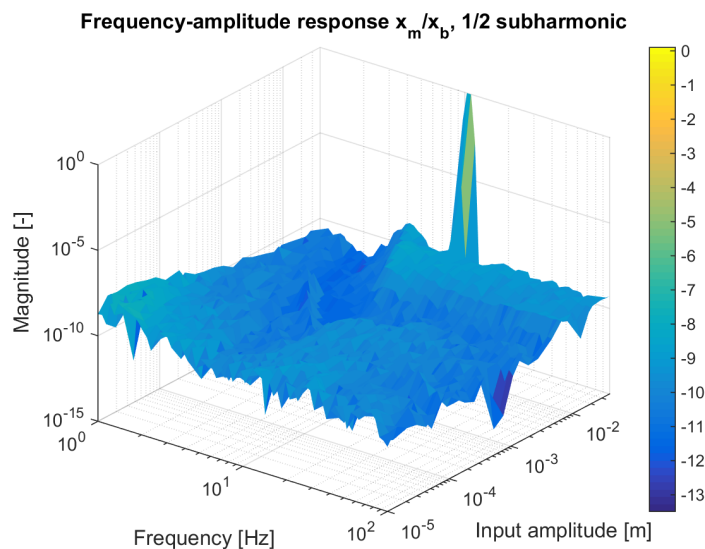
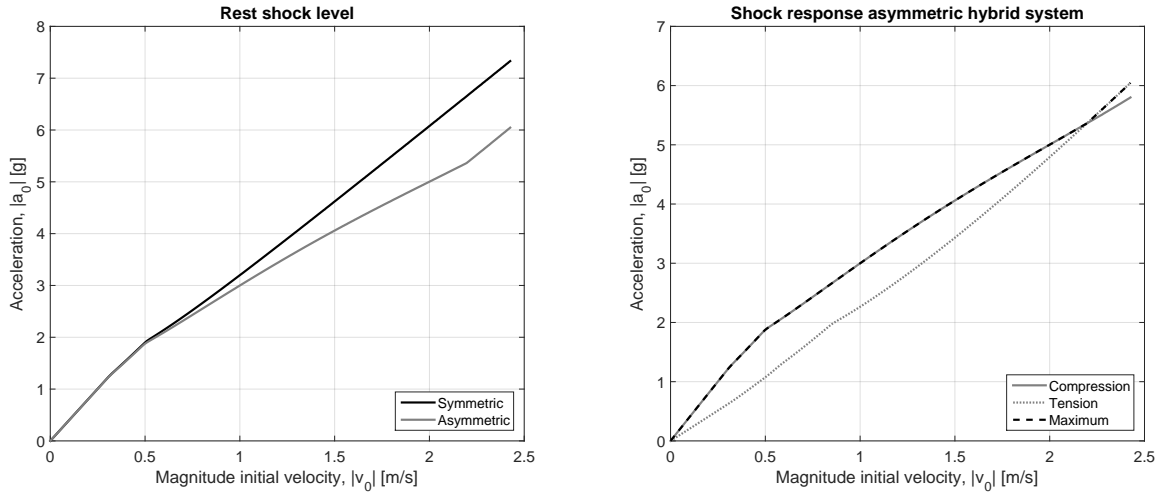


Figure 5.14: Frequency-amplitude diagram, magnitude half subharmonic, asymmetric.

5.3.3 Shock

Conditioned free fall simulations are done for both the symmetric and asymmetric hybrid isolation system. Figure 5.15a shows the rest shock level as function of the initial top mass velocity. Note that again the relaxation and dynamics during the fall in the air are not considered in these simulations, which is the reason that it is called a conditioned free fall. The characteristic is similar to the behaviour of the wire rope isolation systems (figure 3.21). To include all non-linear aspects of the hybrid isolator, the maximum velocity and consequently maximum acceleration are higher.

In figure 5.15a, the slope of the rest shock level decreases stepwise due to the increased effect of slipping of the friction elements for higher velocities. Further, for the asymmetric system, the slope decreases gradually, which represents the softening behaviour of the wire rope isolator under compression. However, near 2.2 m/s the slope increases again. This effect is again caused by the hardening in subsequent tensioning and was already seen in section 3.4.3. Note that all three effects are induced by the wire rope isolator behaviour; the elastomer behaviour is not amplitude dependent. The effective rest shock level reduction due to slipping and softening of the hybrid isolation system is less compared to the wire rope isolation system, due to the series coupled (linear) elastomer isolator.



(a) Rest shock level as function of velocity, symmetric and asymmetric system.

(b) Maximum absolute acceleration in tension and compression, asymmetric system.

Figure 5.15: Shock response hybrid systems.

Figure 5.15b shows both the maximum acceleration level during compression and subsequent tension for the asymmetric system. The curve of the compression acceleration clearly shows the slipping and softening behaviour. Above 2.2 m/s acceleration in tension is dominant.

The contributions of the wire rope isolator and the elastomer isolator to the deflection of the hybrid isolator in compression and tension are shown in figure 5.16. Up to initial velocities of 0.3 m/s , the wire rope isolator behaves linearly. Due to slipping and softening, the wire rope isolator deflects more than the elastomer isolator during shocks with higher initial velocities. The asymmetric softening behaviour has significant influence on the behaviour in compression: the wire rope deflection is significantly increased. The deflection in subsequent tension is only slightly influenced, the non-linear hardening effect is decreased due to frictional dissipation.

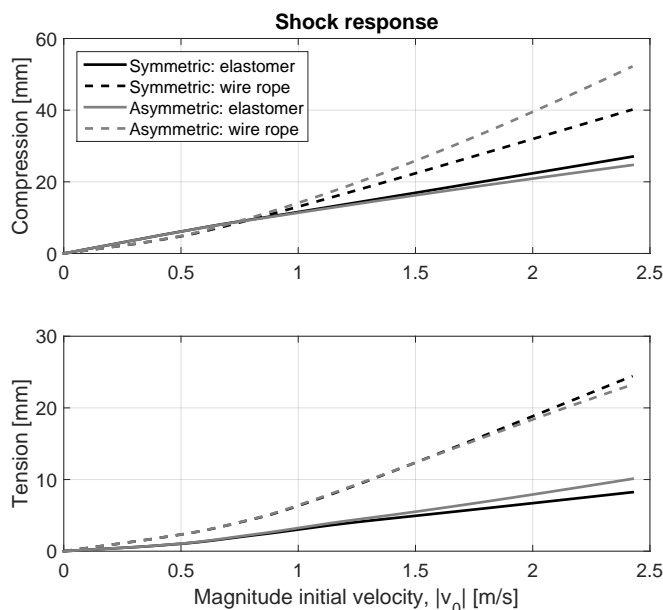


Figure 5.16: Maximum deflection free fall as function of velocity.

5.4 Summary

The modelling of a series hybrid damper system concerns two important aspects. Firstly, an intermediate mass between both isolation components is introduced. This mass is chosen small to avoid strong influence on the dynamics in the interesting frequency range. The dynamic behaviour of the hybrid isolation system is described by a set of 16 first order differential equations. The implicit MATLAB solver `ode15s` (for stiff differential equations) is used to simulate the dynamic model. The stick-slip transition in the Jenkin elements is smoothed to make the problem solvable for the implicit stiff solver. The stiffness of the wire rope components compared to the elastomer stiffness is higher for small response amplitudes and smaller for high response amplitudes.

The dynamic behaviour of the hybrid system is analysed for both harmonic (i.e. single sinusoidal) and shock excitation. For small input amplitude harmonic excitation, the resonance frequency is nicely damped. Here, the elastomer is dominant. High input amplitude excitation leads to relatively less resonance damping (and a decreased resonance frequency), in this case the wire rope isolator behaviour is more dominant. The high frequency isolation properties around 100 Hz are achieved for both small and high input amplitudes, due to dominance of the wire rope isolator.

For small drop heights the hybrid system behaves linearly: the maximum acceleration is proportional with the initial (impact) velocity and the elastomer and wire rope components store and absorb approximately the same amount of energy. Above a certain impact velocity, the friction elements in the wire rope isolator start to slide: the wire rope stiffness decreases and more energy is absorbed by the wire rope spring. This causes the slope of the acceleration versus initial velocity curve to decrease. Softening behaviour of the asymmetric system during compression of the wire rope spring enlarges this effect. Due to the hardening behaviour in subsequent tensioning, the decreasing slope of the acceleration-initial velocity curve of the asymmetric systems evolves eventually in an increasing slope for larger initial velocities.

Chapter 6

Experiments

Experiments are performed to validate and identify the isolator (system) models for a certain configuration of the isolators, which differs to some extent from the configurations (i.e. parameter values) presented in chapters 3-5. Three different types of experiments are done on three different setups. The goal of the first experiment is deriving the (quasi-)static behaviour of the wire rope isolator, the elastomer isolator, and the hybrid isolator. The second experiment analyses the response to floor vibrations and the last experiment examines the shock response of the three isolators. In the quasi-static experiments, only the isolator itself is considered. In the other two experiments, the whole isolation system (isolator with suspended mass) is analysed.

The quasi-static and shock experiments are performed at NTS. The quasi-static tests are done by use of an existing setup. A drop test setup has been designed and built to analyse shock behaviour. The vibrational experiments have been performed at the DCT lab of the TU/e with an existing shaker setup. All measurements have been repeated three times to check repeatability.

In section 6.1, firstly the setups are further discussed. In the next three sections, the measurement results of respectively the wire rope, elastomer, and hybrid isolator are presented. In section 6.5, a short summary of the measurement analysis is given.

6.1 Measurement hardware

For each of the three experiments, a different setup is used. The quasi-static and shaker setup are existing measurement setups at respectively NTS and the TU/e. For the shock experiment a new setup has been designed and built at NTS. In this section, the setups are briefly discussed. More detailed information and pictures are presented in appendix D.1.

In the first type of experiment, the isolation elements are compressed and extended with a velocity close to zero, i.e. the quasi-static behaviour is derived. Both static and hysteretic force-deflection characteristics can be measured (relaxation effects are neglected). The goal is to determine the static stiffness of the elastomer and the hysteretic characteristic of the wire rope isolator. The hybrid isolator is not measured, but its (static) characteristic can be directly derived from the components measurements. The isolator is mounted in a lathe (a schematic overview is shown in figure 6.1), which provides stiff boundary conditions. A (small) axial velocity of the linear guidance of the lathe can be accurately prescribed. The displacement x of the guidance is manually controlled by a spindle, where both the displacement x and force F are measured. A detailed description is given in D.1.1.

The dynamic behaviour of the isolation systems is measured on an existing shaker setup at the DCT-lab of the TU/e, a schematic overview of the setup is shown in figure 6.1. The shaker prescribes the base motion of the isolation system. Two type of measurements are made: white noise and harmonic (base) excitation. The random noise input is only applied to the elastomer isolation system and used to derive an estimate of the (linear) FRF of the elastomer system. Harmonic excitation is used to be able

to describe the response by HOSIDF's and to visualize (non-linear) behaviour in frequency-amplitude diagrams. The top mass velocity v_m , the base position x_b , the base velocity v_b , and control voltage U_{in} are measured. A more detailed description of the shaker setup and important aspects of the HOSIDF's approach are presented in D.1.2.

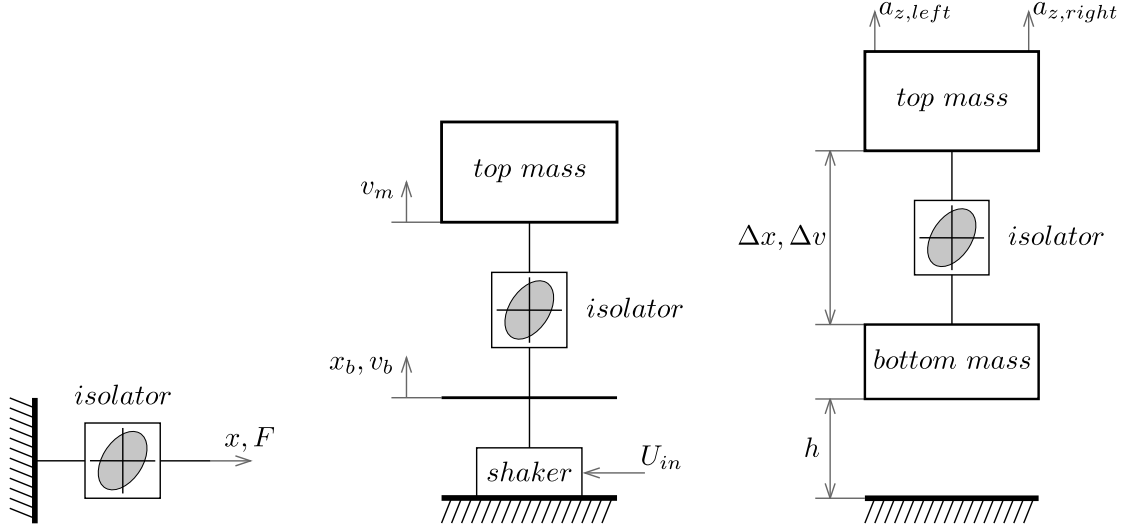


Figure 6.1: Schematic overview quasi-static (left), shaker (middle), and drop test (right) setups.

Shock experiments are done on a drop test setup, which has been designed and built at NTS. The setup consists of a frame with two linear guides and a release mechanism, a schematic overview is shown in figure 6.1. The frame is made from standard aluminium profiles. The base and top mass of the isolation system can only translate vertically due to linear guidance. The assembly (with parts list of the design and technical drawings of the parts) is shown in appendix D.2. The vertical accelerations of the top mass (i.e. $a_{z,left}$ and $a_{z,right}$) and velocity and displacement over the isolator (i.e. Δv and Δx) are measured. A more detailed description of this setup is given in D.1.3. Furthermore, a high speed camera is used to capture the behaviour visually.

The isolator components are chosen from the Socitec catalogue. The smallest elastomer mount is chosen, i.e. BFL-12, which is designed for a nominal loading of 5 kg , with an indicated static stiffness of $12 \cdot 10^3 \text{ N/m}$. The wire rope isolator is chosen from the half-helical series with the smallest cable diameter. The desired static stiffness must be slightly higher than the elastomer stiffness, which resulted in the choice of the HH8-38TCM model. The maximum static load for this isolator is 137 kg with an indicated stiffness of $21 \cdot 10^3 \text{ N/m}$. The product sheets of both isolators are shown in appendix D.3.

6.2 Wire rope isolator

6.2.1 Quasi-static experiment

The quasi-static measurements yield the characteristic hysteretic loops. Two types of measurements are performed; small deflection input loops and large deflection input loops. The upper limit for the small input displacement magnitude is related to the vibrational behaviour: from the product sheet, see section D.3, a maximum vibrational input of 4.5 mm is obtained. Based on this information, the small input displacement range is set from 0.05 mm to 4.5 mm . The large deflection measurements are related to the global behaviour and shock response. The maximum displacement amplitude is chosen around 40 % of the maximum shock input displacement. This results in a displacement amplitude range from 1 mm to 15 mm . Due to the different time scales of real shock and this quasi-static experiment, this safety margin is used. Both types of measurements are performed three times.

Figure 6.2 shows the hysteretic loops derived from one of the small displacement input (vibration related) measurements. The stick-slip transition phenomena already starts at microlevel and is smooth. The deflection is applied manually and thus not applied linearly as function of time. This causes the small spikes. This small amplitude measurement already indicates a slight softening effect in compression and a slight hardening effect in tension. The dotted line represents the static stiffness indicated by the supplier. Apparently, the global stiffness is indicated by this value. The large amplitude quasi-static behaviour is visualized in figure 6.3. Asymmetric softening and hardening behaviour is clearly indicated.

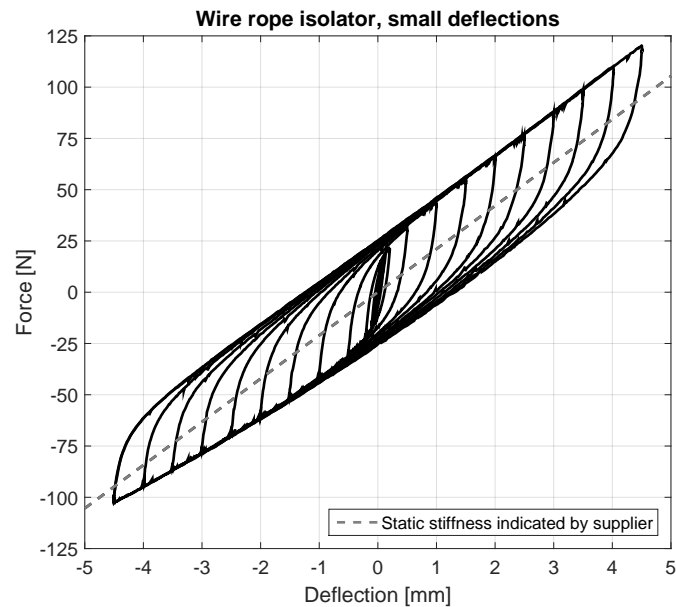


Figure 6.2: Quasi-static measurement wire rope isolator, small input deflections.

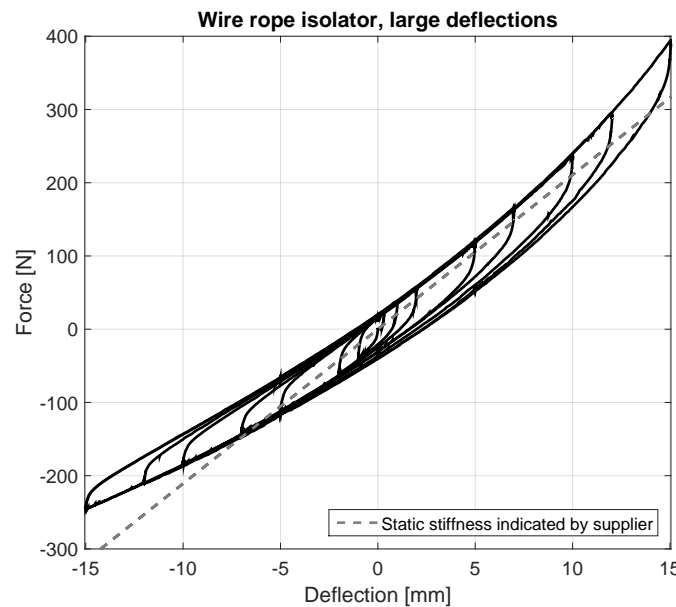


Figure 6.3: Quasi-static measurement wire rope isolator, large input deflections.

6.2.2 Shaker experiment

Next, the wire rope isolator is tested on the dynamical shaker setup. Now, the ratio of the velocity response of the top mass and the base velocity (v_m/v_b) is further visualized and analysed by frequency-input amplitude response diagrams. In this analysis the higher harmonics in the velocity base signal v_b are neglected, and the magnitude of the first harmonic is denoted by $\sim v_b$. A detailed analyses of the (limitations of the) input signal is presented in appendix E.1.1. The masses of the system's top mass and isolator are respectively 2.98 kg and 0.21 kg (listed in appendix D.1.2). Figure 6.4 shows the magnitude diagram of the first harmonic of the velocity ratio. For small input amplitudes, the resonance frequency is high (65 Hz) and the system's behaviour is close to undamped. An increase in input amplitude results in a decrease in resonance frequency and increase in damping; the cable strands start to slide. Amplitude cross sections of the magnitude and phase of this first harmonic, as shown in figure 6.5, clearly indicate these effects. The resonance frequency is halved, while the close to undamped system evolves into a heavily damped system.

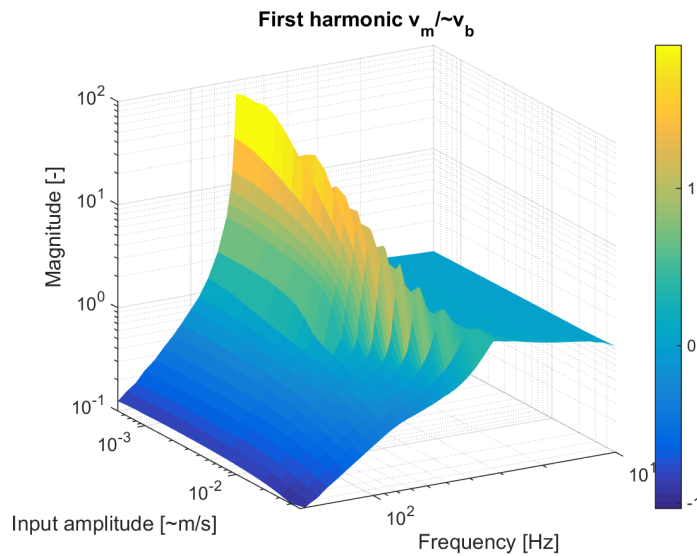


Figure 6.4: Frequency-amplitude diagram $v_m/\sim v_b$, magnitude 1st harmonic.

The higher harmonics in the system response may originate from both the periodic (not pure harmonic) input of the shaker table and the non-linear character of the isolation system itself. These two sources cannot be distinguished in the frequency-amplitude diagrams. Figure 6.6 shows the magnitude diagram of both the second and third harmonics response components (to the first harmonic of v_b) of the isolation system ($v_m/\sim v_b$). A top view of the magnitude-amplitude diagrams is shown, where blue indicates a low magnitude and yellow a high magnitude. Although these higher harmonic responses are not fully caused by the non-linear behaviour of the isolation system, still some aspects of this non-linear behaviour may be observed. At low input amplitudes, peaks appear around 30 Hz (in the third harmonic), 45 Hz (in the second harmonic), and 65 Hz (in both harmonics). Note that the 25 Hz and 50 Hz peaks originate from the power supply. The 65 Hz peak coincides with the resonance of the isolation system. The 30 Hz and 45 Hz peaks can originate from the resonance of the coupled shaker and isolation systems (i.e. respectively $1/3$ and $1/2$ of the 90 Hz resonance), or they can represent a second superharmonic (30 Hz) and a half subharmonic of the third superharmonic (45 Hz) of the isolation system resonance (i.e. respectively $1/2$ and $2/3$ of 65 Hz), which was also seen for the piecewise linear system in [15].

In figure 6.6, the magnitudes of the peaks decrease for increasing input amplitude to $3 \cdot 10^{-3} \text{ m/s}$ due to the improved signal to noise ratio. For a further increase in input amplitude, the peaks broaden and the frequency of the peaks decreases. This behaviour is mainly seen in the third harmonic component and is an indication for the increased (non-linear) stick-slip behaviour of the wire rope spring, which confirms

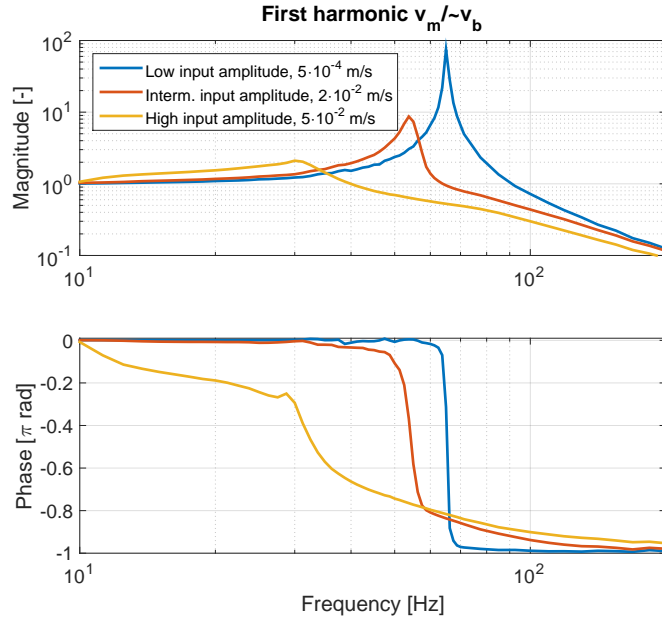


Figure 6.5: Frequency response diagram $v_m/\sim v_b$, 1st harmonic.

the observations from the first harmonic component. The second harmonic only shows a small increase in peak magnitude for increasing amplitude. This even component is mainly related to the asymmetric soft-hardening behaviour, which contribution is small due to the relatively small base input amplitude (figure 6.2).

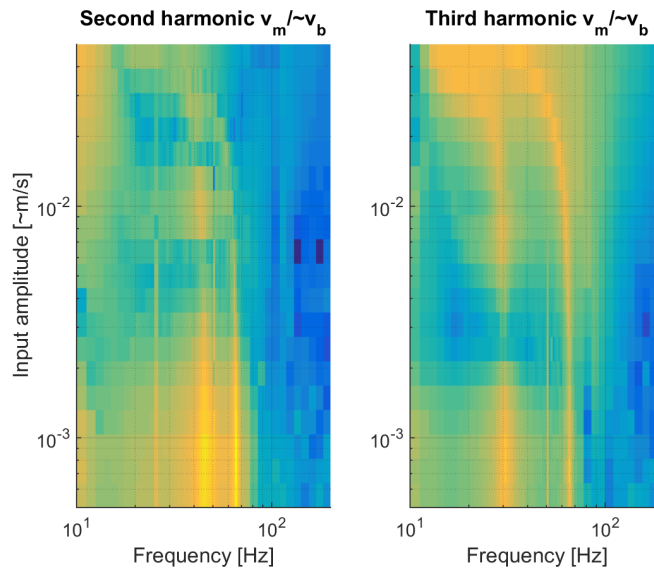


Figure 6.6: Frequency-amplitude diagram $v_m/\sim v_b$, magnitude 2nd and 3rd harmonic.

6.2.3 Drop test

In the third wire rope experiment, the wire rope isolation system is tested on the drop test setup to examine the response to shock. The isolation system consists of a bottom mass (of 7.88 kg), a wire rope isolator (of 0.21 kg) and a top mass. Several experiments are performed, in which the drop height is varied (i.e. 1-14 cm) for two different top masses (i.e. 4.33 kg and 7.39 kg). The relative displacement

and velocity over the isolator and the absolute acceleration of the top mass are measured. The mass and drop height values are also listed in appendix D.1.3. In this section, both the light and heavy mass systems are considered for a drop from 8 cm. The time responses of the isolator deflection, the relative velocity over isolator, and the absolute vertical top mass acceleration (the mean value of the two accelerometers) are shown for three repeated measurements. Note that the velocity and acceleration signal are filtered by a moving average over 5 data points (i.e. 2.4 ms). To preserve the phase properties, the signal is filtered in both directions. Marked time instances are visualized by time frames made by the high speed camera, which are shown in appendix E.1.2. More clear images and slow motion movies are available on the attached dvd.

Figure 6.7 shows the time responses of the light (4.33 kg) mass (high resonance frequency) system. The mass ratio of the bottom to the top mass is around 2. The relatively heavy bottom reduces effects of bouncing.

- At t_1 the system is released. Up to the moment of impact (t_2), the system relaxes and shows some minor dynamics. Note that these dynamics are related to the bottom mass-isolator-top mass system, and thus also depend on the bottom mass value. Due to the wire rope friction the behaviour from t_1 to t_2 is heavily damped.
- At t_2 , the time of impact, there is a step in the relative velocity. Hereafter, some small rotational bouncing occurs of the bottom mass on the ground plate, because of small misalignments.
- At t_3 , the isolator is maximally compressed, a peak in deflection and acceleration is observed.
- At t_4 , the isolator is maximally stretched. Note that the bottom mass is lifted from the ground plate (detached) at this time (this is more clearly seen in the movie). Further, the deflection during stretching is less compared to deflection during compression (t_3). However, due to the soft-hardening behaviour of the wire rope isolators the accelerations at t_3 and t_4 are similar in absolute value.
- At t_5 , the isolator is again in compression, however the bottom mass is still in air (clearly seen in the movie).
- At t_6 , a second (smaller) impact takes place between the bottom mass and the ground plate, while the isolator is slightly stretched. From this time on, the bottom mass remains on the ground plate and the oscillation is damped out.

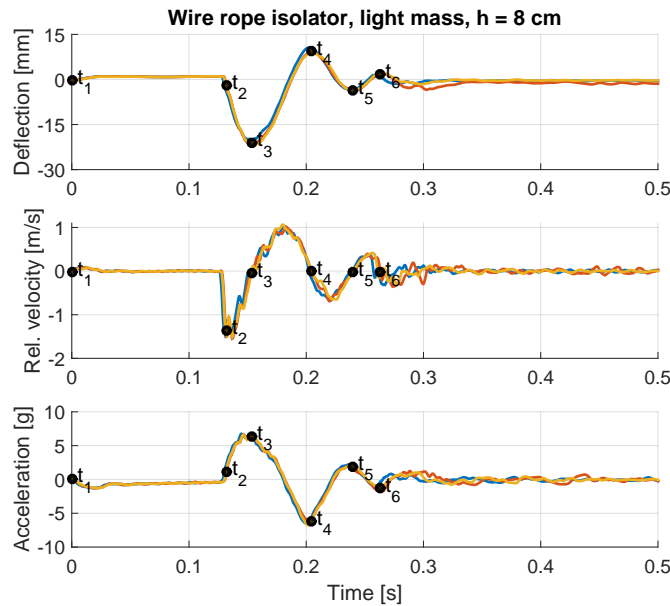


Figure 6.7: Time response free fall wire rope isolator, light mass (i.e. 4.33 kg), $h = 8$ cm.

The dynamic behaviour of the heavy (7.39 kg) mass (low resonance frequency) system is shown in figure 6.8. The ratio of the bottom to the top mass is around 1. More re-bouncing from the bottom plate is expected for this configuration. The resonance frequency of the system is lower. This results in a higher deflection peak and a lower acceleration peak, as indicated in (3.21) and (3.23) for the linear case.

- At $t = 0$, the system is released and consequently relaxes.
- At t_1 , the bottom mass hits the ground plate and there is a step in the relative velocity.
- At t_2 , the bottom mass is loose from the ground plate due to a heavy re-bounce. The isolator, however, is almost maximally compressed.
- At t_3 , the isolator is maximally compressed and the bottom mass is on the ground plate again.
- At t_4 , the isolator is maximally stretched, the bottom mass is lifted (detached) from the ground plate again. Although the deflection in stretching is less compared to the deflection in compression (t_3), the absolute acceleration of the top mass is higher. Compared to the light mass system, the deflection in stretching is higher, thus the asymmetric soft-hardening effect is stronger.
- At t_5 , the isolator is again in compression, whereas the bottom mass is still in the air.
- At t_6 , during stretching the bottom mass hits the ground plate. From this time on, the bottom mass remains on the ground plate and the oscillation is damped out.

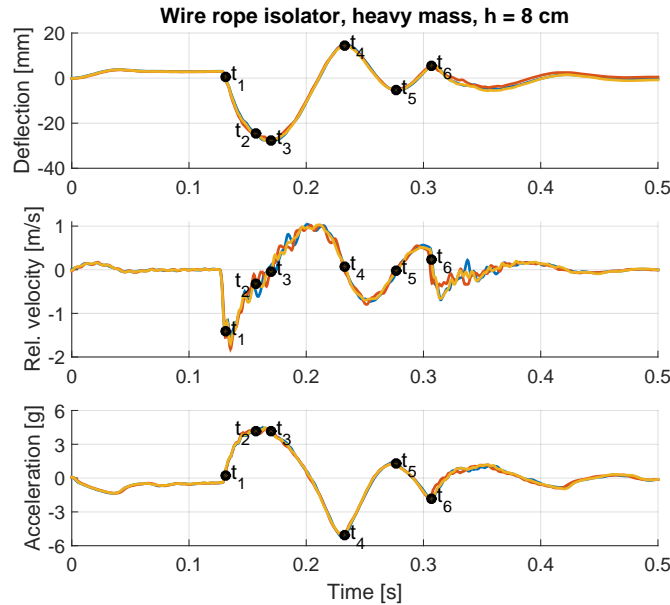


Figure 6.8: Time response free fall wire rope isolator, heavy mass (i.e. 7.39 kg), $h = 8 \text{ cm}$.

When studying figure 6.7 and figure 6.8, it may be concluded that the repeatability of the experiments is good.

6.3 Elastomer isolator

6.3.1 Quasi-static experiment

The quasi-static measurements are used to determine and validate the static stiffness of the Socitec BFL-12 elastomer mount. Further, possible amplitude dependent behaviour can be detected. The elastomer is quasi-statically compressed and stretched with amplitudes from 1 mm up to 8 mm . This corresponds with a maximum load of around 1.7 times the maximum static load and 20 % of the maximum shock deflection (accordingly to the product sheet in appendix D.3). Each measurement with constant amplitude is performed three times. Figure 6.9 shows the different measurements in one force deflection diagram. The measurements nicely overlap.

Around the origin the measured stiffness is around 15 % higher compared to the stiffness indicated in the product sheet (12 N/mm), the latter being indicated by the black dotted line. A deviation of 15 % is not uncommon for rubber components. Moreover, note that temperature dependency is not considered. Further, the behaviour in tension up to 8 mm is linear. In compression, a small softening effect is seen. During loading cycles, small narrow loops are formed due to the small but non-zero deflection velocity. There are no significant hysteretic effects seen in the quasi-static measurement results.

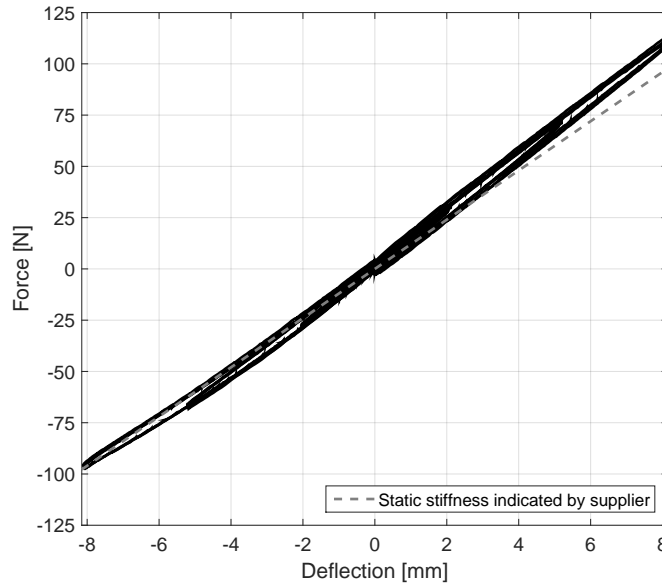


Figure 6.9: Quasi-static measurement Socitec BFL-12 elastomer.

6.3.2 Shaker experiment

Two types of vibrational measurements are performed on the dynamical shaker setup. Both harmonic input and white noise input are applied. Linearity of the elastomer linearity is assessed by the harmonic input measurements. White noise inputs are used for the identification of the (linear) model parameters. The system's top mass and isolator mass values for the harmonic input measurements are respectively 0.99 kg and 0.53 kg. In the measurements with white noise input, the top mass is varied from 0.99 kg to 6.40 kg, the mass values are summarized in appendix D.1.2.

Firstly, harmonic (voltage) input is applied to determine the the HOSIDF's. In the following analysis, the higher harmonics in the velocity base signal are neglected, and the magnitude of the first harmonic is denoted by $\sim v_b$. A detailed analyses of the (limitations of the) input signal is presented in appendix E.2.1. The magnitude and phase of three input amplitude cross sections of the first order harmonic of the ratio ($v_m/\sim v_b$) are shown in the frequency response diagram of figure 6.10. In the magnitude plot, a typical response of a linear isolation system is shown: stiff behaviour for low frequencies, a damped resonance, and high frequency isolation. The shift in eigenfrequency for varying input amplitude is negligible and, consequently, a linear amplitude independent model suffices. In line with these observations it is noted that the higher harmonics in the velocity response of the top mass (mainly) result from the higher harmonics in base velocity and not from non-linear behaviour of the elastomer isolator.

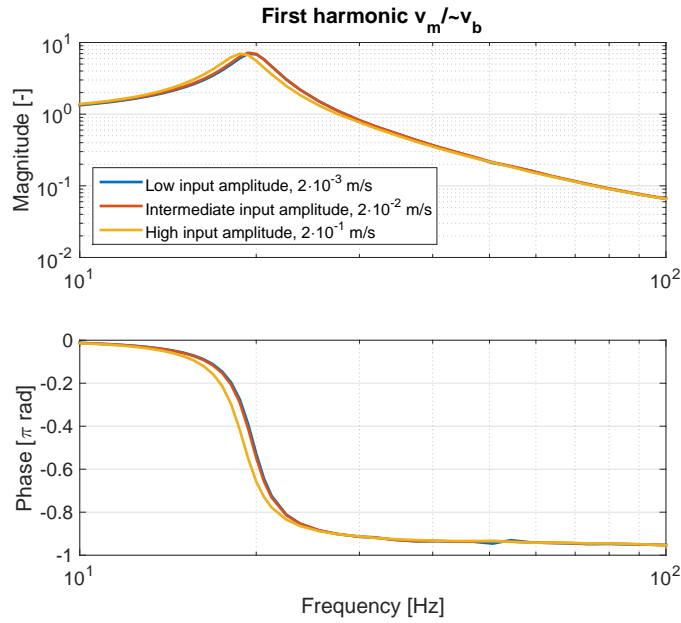
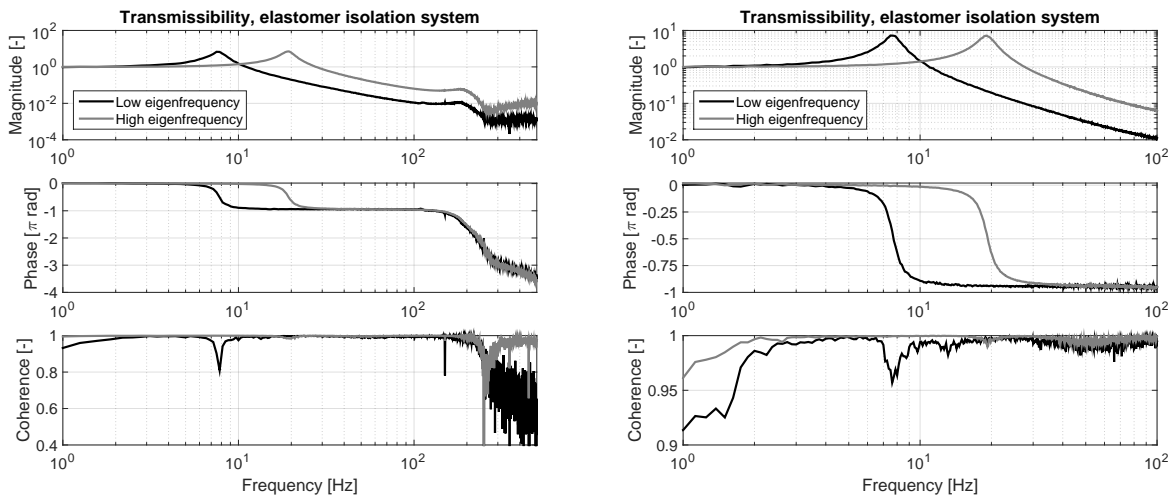


Figure 6.10: Frequency response diagram $v_m/\sim v_b$, 1st harmonic.

Because linear behaviour is now experimentally established, the system is now excited with white noise input to experimentally determine the transmissibility. The eigenfrequency is alternated by varying the top mass, in total eight different systems are measured in the range from 0.99 kg to 6.40 kg. Figure 6.11a shows the transmissibility FRF's of the 0.99 kg and 6.40 kg top mass isolation systems for a frequency up to 500 Hz. Up to frequencies of 100 Hz, the FRF's clearly indicate a system with only one mass with a resonance at respectively 7.5 Hz and 19 Hz. Around 200 Hz an unexpected resonance appears. The coherence is still sufficient, so non-linear behaviour or high disturbance noise is not dominant. Probably, the second mode appears due to distributed mass effects in the elastomer, which also has a non-uniform cross section. Note that this second resonance frequency does not depend on the value of the top mass. For a more uniform cross section of another type of elastomer, this second eigenfrequency can be much higher. Therefore, from now on only the frequency range of 1 Hz to 100 Hz is considered.



(a) Frequency range up to 500 Hz.

(b) Frequency range up to 100 Hz.

Figure 6.11: Transmissibility (FRF), white noise input.

Figure 6.11b shows a zoom of figure 6.11a for the frequency range 1-100 Hz . The decrease in maximum frequency enables an increase in excitation amplitude. This is possible due to the significant bandwidth decrease of the white noise excitation signal. From the eight systems considered, again only the two systems with lowest and highest mass are shown. The transmissibility curves in figure 6.11b indicate an isolation system with one moving mass and the coherence is approaching 1. The measurement data presented in figure 6.11b is therefore qualified to identify the massless generalized Maxwell elastomer model.

6.3.3 Drop test

The third elastomer experiment is done on the drop test setup, where the shock response is investigated. Measurements with two different top masses (i.e. 4.37 kg and 7.42 kg) and varying drop heights (1-14 cm) are performed. The value of the bottom mass is 7.83 kg for both systems and the weight of the elastomer isolator is 0.53 kg . In appendix D.1.3 the masses and drop height range are summarized. The 6 cm drop height measurements of both systems are presented in this section. The measurements are repeated three times. Similar to the wire rope shock analysis, also here both (filtered) time responses and specific time frames (appendix E.2.2) are shown. More clear images and slow motion movies are available on the attached dvd.

Figure 6.12 shows the time responses of the light, 4.37 kg , mass (high eigenfrequency) system. The mass ratio of the bottom to the top mass is around 2.

- At t_1 , the system is released and starts to relax.
- At t_2 , the isolator is oscillating in the air. In contrast to the wire rope system, the oscillations are more lightly damped.
- At t_3 , the isolation system hits the ground plate, which results in a step in the relative velocity.
- At t_4 , the elastomer is fully compressed. A peak in the elastomer compression and the top mass acceleration appears.
- At t_5 , the elastomer is maximally stretched. In absolute value the maximum stretch is less compared to the maximum compression (t_4). Note that the bottom mass is lifted from the ground plate at this time (detachment). The detachment is clearly shown in the movie.
- At t_6 , the elastomer is again in compression, while the bottom mass is back on the ground plate. Subsequently, the oscillation is slowly damps out.

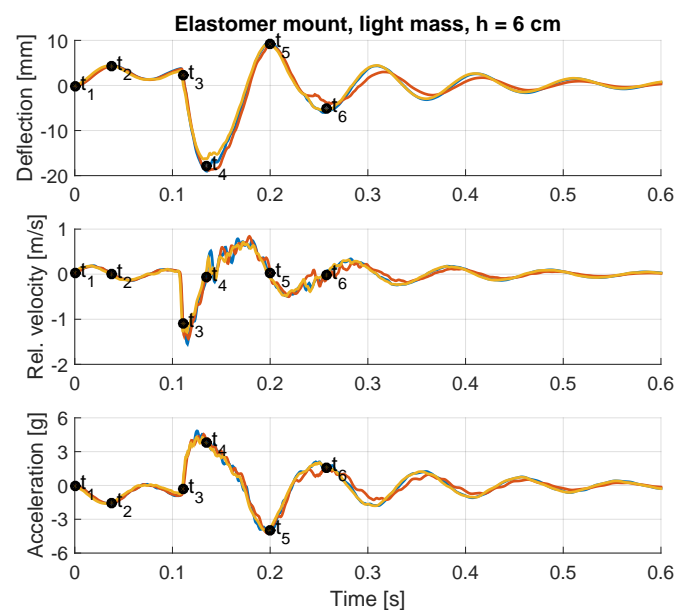


Figure 6.12: Time response free fall elastomer isolator, light mass (i.e. 4.37 kg), $h = 6$ cm .

The shock behaviour of the heavy, 7.42 kg , mass (low eigenfrequency) system is shown in figure 6.13. The ratio of the bottom to the top mass is around 1 and again more re-bounce from the ground plate is expected for this configuration. The eigenfrequency of the system is lower and therefore a higher deflection peak and a lower acceleration peak are expected.

- At t_1 , the system is released and consequently relaxes.
- At t_2 , the system is oscillating. Again, this behaviour is more lightly damped, compared to the wire rope case.
- At t_3 , the isolation system hits the ground plate and there is a step in the relative velocity.
- At t_4 , the deformation of the elastomer is not axisymmetrical (causing rotational oscillations of the top mass compared to the bottom mass) and out-of-plane. The out-of-plane elastomer stiffness is small compared to its vertical stiffness. The resulting behaviour is undesired. The decrease in effective stiffness results in a decrease in vertical top mass acceleration.
- At t_5 , the elastomer is maximally compressed and only deflected vertically.
- At t_6 , the elastomer is maximally stretched without rotation. The vibrational behaviour from t_5 to t_6 differs from the behaviour from t_6 onwards. The oscillation frequencies seem to differ (deflection plot) and the slope of the acceleration changes sign between t_5 and t_6 . This indicates non-linearity (softening) for higher compression values.

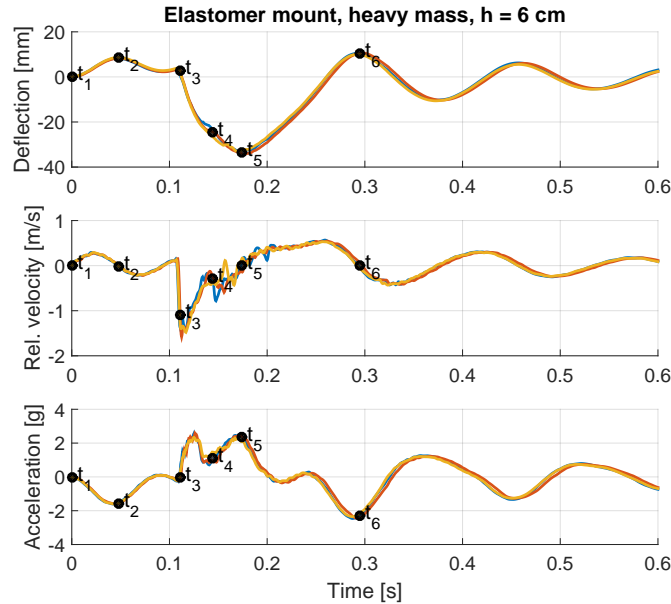


Figure 6.13: Time response free fall elastomer isolator, heavy mass (i.e. 7.42 kg), $h = 6\text{ cm}$.

6.4 Hybrid isolator

6.4.1 Quasi-static experiment

For the hybrid configuration the quasi-static experiment has not been carried out. By simply adding the elastomer and wire rope quasi-static measurements, a characteristic (static) hysteretic loop of the hybrid isolator is obtained, which is caused by the wire rope spring.

6.4.2 Shaker experiment

In the vibration tests, the hybrid isolation system is again excited by means of a harmonic voltage input signal, which approximately results in a harmonic base velocity. The top mass equals 0.99 kg , the intermediate mass equals 0.14 kg , and the masses of the wire rope and elastomer isolators are respectively 0.21 kg and 0.53 kg (also listed in appendix D.1.2).

Again, in the isolation system analysis, the higher harmonics in the velocity base signal are neglected, and the resulting first harmonic is denoted by $\sim v_b$. A detailed analysis of the (limitations of the) input signal is presented in appendix E.3.1. The magnitude of the response of the first harmonic of the isolation system $v_m/\sim v_b$ is visualized in figure 6.14. For low input amplitudes, the system is significantly damped and isolation performance is preserved. The elastomer is dominant in this region. Higher input amplitudes result in a decreasing resonance frequency (i.e. from 20 Hz to 15 Hz) and an increase in resonance damping. Apparently, the effective viscoelastic damping is less than the effective friction induced damping. The cable strands of the wire rope isolator start to slide with respect to each other causing dissipative friction forces. This transition is continuous for increasing input amplitudes. However, due to setup limitations it is not possible to perform measurements at input amplitudes larger than 0.2 m/s . The stiffness of the wire rope isolator is higher than indicated by the product sheet, and thus also compared to the elastomer stiffness. Consequently, the elastomer behaviour is dominant for all input amplitudes and the stiffness transition is relatively small.

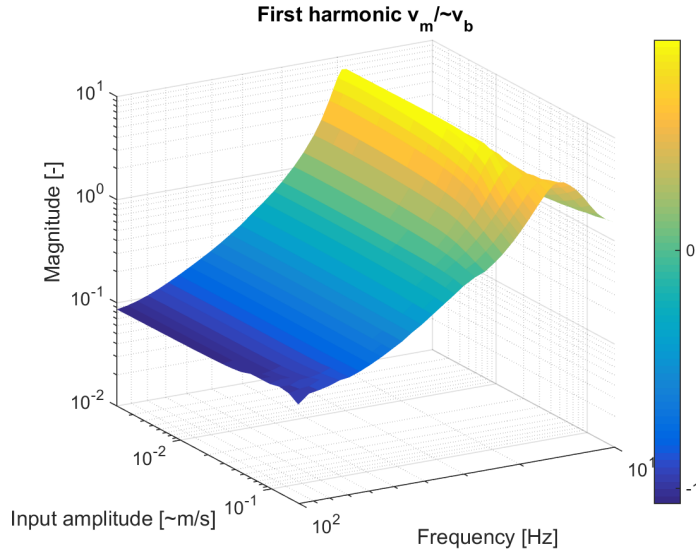


Figure 6.14: Frequency-amplitude diagram $v_m/\sim v_b$, magnitude 1st harmonic.

Frequency response diagrams of magnitude and phase of the first harmonic of the ratio $v_m/\sim v_b$ for three different base (input) amplitudes are shown in figure 6.15. For increasing input amplitudes, the decreasing resonance frequency and increasing damping are clearly recognizable. The isolation performance is good for all input amplitudes. Near 100 Hz , the influence of the intermediate mass resonance (especially for higher amplitude input) is also visible in both phase and magnitude.

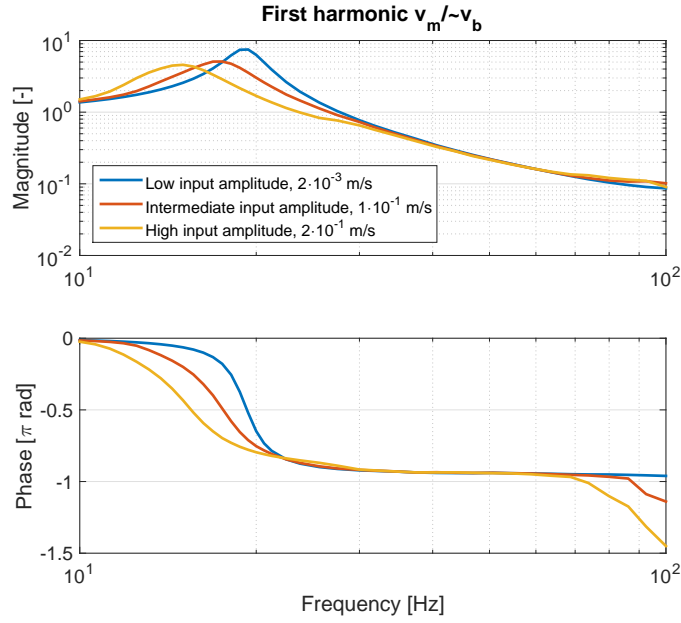


Figure 6.15: Frequency response diagram $v_m/\sim v_b$, 1st harmonic.

The magnitudes of the second and third harmonic of the system top mass velocity divided by the first harmonic of the base velocity ($v_m/\sim v_b$) are shown in figure 6.16. A top view of the magnitude-amplitude diagrams is shown, where blue indicates a low magnitude and yellow a high magnitude. Since the shaker system itself also shows a little amount of non-linear behaviour, only trends related to the non-linear dynamics of the hybrid isolation system can be observed. Slip of the wire rope cable strands is indicated by the third harmonic. For low input amplitudes, the strands stick. Increasing the input amplitude leads to a broadening slip area around the resonance frequency near 20 Hz. The same region is also indicated in the second harmonic. In addition, the second harmonic is more dominant for frequencies close to 10 Hz. This can be directly related to the non-linear resonance of the electromechanical shaker system, which is confirmed by the second harmonic in the base velocity input in this region, discussed in appendix E.3.1.

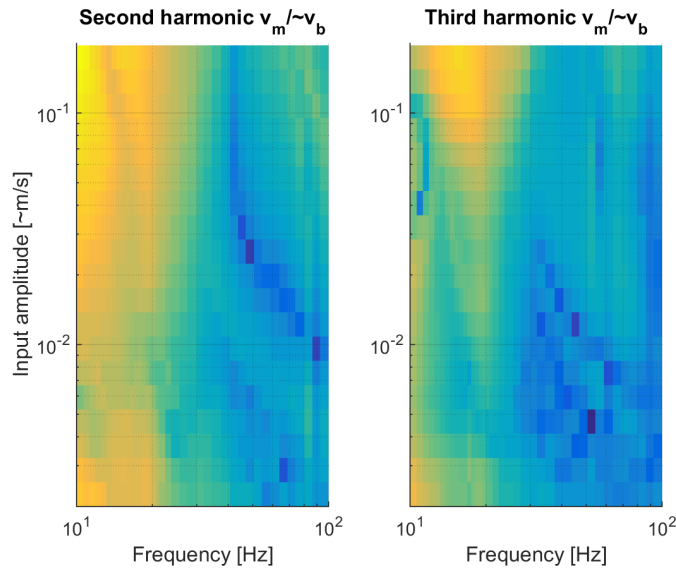


Figure 6.16: Frequency-amplitude diagram $v_m/\sim v_b$, magnitude 2nd and 3rd harmonic.

6.4.3 Drop test

Finally, the hybrid isolation system is tested on the drop test setup. Two systems, with a top mass of respectively 4.25 kg and 7.31 kg are measured over a drop height range of $1\text{-}14\text{ cm}$. The mass values of the bottom mass (i.e. 7.83 kg), the intermediate mass (i.e. 0.14 kg), the wire rope isolator (i.e. 0.21 kg), and the elastomer mount (i.e. 0.53 kg) are identical for both systems. All values are listed in appendix D.1.3. In this section, the 6 cm drop test measurements of both systems are presented. Each measurement is repeated three times. Both time responses and selected time frames (appendix E.3.2) are shown. More clear images and slow motion movies are available on the attached dvd. The stiffness of the wire rope isolator is higher than expected. Consequently, the elastomer deformation is dominant.

Figure 6.17 shows the time responses of the light, 4.25 kg , mass (high resonance frequency) system. The mass ratio of the bottom to the top mass is around 2. The relatively heavy bottom mass reduces the effects of re-bounce.

- At t_1 , the isolation system is released and the isolator starts to relax.
- At t_2 , the system is oscillating in the air. The deformation of the elastomer component is dominant, thus the behaviour is not overdamped.
- At t_3 , the impact occurs. There is a step in the relative velocity and the isolator starts to compress.
- At t_4 , the hybrid isolator is maximally compressed. The intermediate mass is moving out-of-plane. This is caused by the low rotational stiffness of the elastomer.
- At t_5 , the hybrid isolator is maximally stretched and moving only in vertical direction. Furthermore, the bottom mass is still on the ground plate.
- At t_6 , the hybrid isolator is again in compression. From this time onwards, the oscillation damps out slowly.

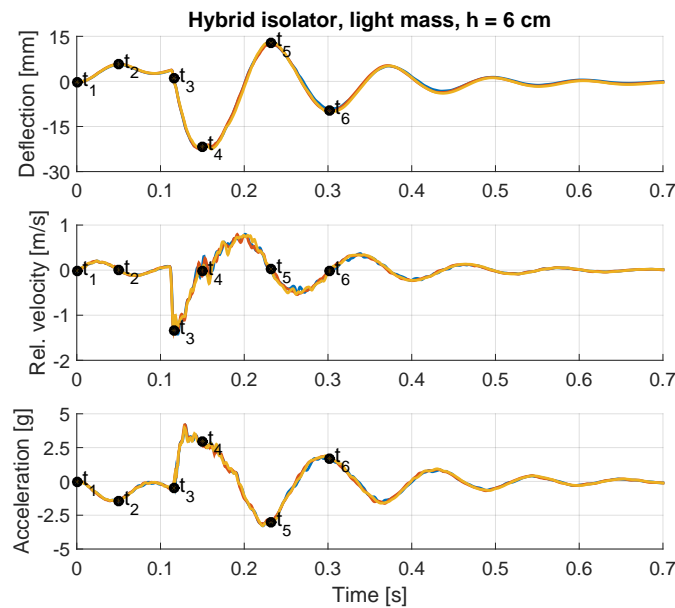


Figure 6.17: Time response free fall hybrid isolator, light mass (i.e. 4.25 kg), $h = 6\text{ cm}$.

The shock behaviour of the heavy, 7.31 kg, mass (low eigenfrequency) system is shown in figure 6.18. While the ratio of the bottom to the top mass is around 1, still the level of re-bounce is limited. The resonance frequency of this system is lower, this results in a higher deflection peak and a lower top mass acceleration peak.

- At t_1 , the isolation system is released and the hybrid isolator starts to relax.
- At t_2 , the system is oscillating. The elastomer component is dominant, thus the oscillation is not overdamped.
- At t_3 , the moment of impact, there is a step in relative velocity and the hybrid isolator starts to compress.
- At t_4 , the hybrid isolator is only compressed in vertical direction. After t_4 , the hybrid isolator starts to deform out-of-plane.
- At t_5 , the isolator is maximally compressed. The intermediate mass is out-of-plane and there are rotational effects. Furthermore, the low rotational stiffness also results in a decrease in the vertical top mass acceleration.
- At t_6 , the isolator is maximally stretched without rotational effects. The frequency of oscillation from time t_5 to time t_6 differs from the frequency of oscillation after t_6 . This is probably caused by non-linear (softening) behaviour of the elastomer for high compression amplitudes.

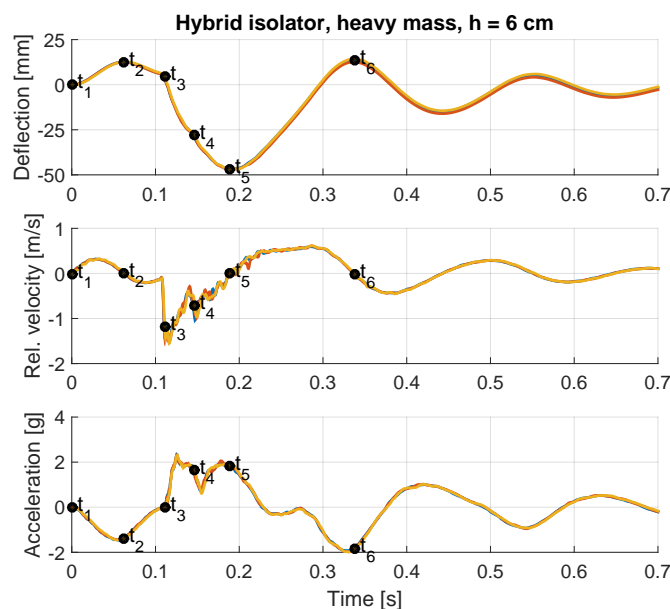


Figure 6.18: Time response free fall hybrid isolator, heavy mass, $h = 6 \text{ cm}$ (i.e. 7.31 kg).

6.5 Summary

This chapter contains results of the quasi-static, vibrational, and shock experiments of wire rope, elastomer, and hybrid isolators.

The quasi-static behaviour of the wire rope isolator is characterized by its hysteretic loops. These loops nicely show the small amplitude (i.e. local) stick-slip behaviour and high amplitude (i.e. global) asymmetric soft-hardening behaviour. The elastomer isolator measurements show a linear static stiffness at least up to 8 mm deflection, in compression as well as in tension. The static hysteretic loop of the hybrid isolator can easily be synthesized by combining both components.

The shaker experiments for investigation vibrational behaviour are performed with all three isolator systems. A harmonic base motion is required to determine HOSIDF's of the top mass response. However, the electromechanical shaker system is controlled by a voltage. Therefore, over the frequency range of interest, the voltage input amplitude is manually controlled to approximate a harmonic base velocity with a frequency independent amplitude. However, the base velocity still contains higher order harmonics, although their amplitudes are quite small. These higher harmonics may originate from both the shaker system and the wire rope isolator (if present). Consequently, the higher order harmonics of the top mass response are influenced by both the non-linear behaviour of the wire rope isolator and higher harmonics in the base velocity signal. The wire rope vibrational analysis clearly shows the (initial) decrease in stiffness and increase in damping when increasing the input amplitude from small to moderate values. The higher order harmonics in the top mass response only indicate (smooth) stick-slip transitions. Vibrational measurements of the elastomer isolator show linear behaviour for (relatively small) vibrational input. White noise excitation is applied to determine the linear FRF. The specific elastomer mount appears to have a second mode at already 200 Hz . Here, the isolator resonates due to its distributed mass. Vibrational measurements of the hybrid isolator show a decrease in stiffness and increase in damping for increasing input amplitude (due to the wire rope spring). The higher harmonics in the top mass response, again give a good indication of stick-slip transition. Only the first part of this transition region is measured due to setup limitations on the maximal input amplitude. The stiffness ratio of the wire rope and elastomer components is higher than expected from the product sheets. Consequently, the elastomer is dominant over a broad amplitude range.

Lastly, shock experiments are done on the drop test setup. Here, some effects are seen which are not incorporated in the conditioned free fall simulations: relaxation and vibrations during the free fall in air, re-bounce from the ground plate, bottom mass detachment in tension, and rotational and out-of-plane behaviour. When the bottom mass is released the falling system relaxes and starts to oscillate. The oscillation frequency is dependent on both the top and bottom mass. Due to small misalignments at the moment of impact and partial elastic collision, there are bounces from the ground plate. Furthermore, a small bottom mass results in heavy bouncing. This affects both the deflection of the isolator and the acceleration of the top mass. The wire rope drop test measurements clearly show the soft-hardening behaviour and effect of bouncing. Experiments with the elastomer isolation system show non-linear behaviour for large isolator deflections. Further, because of the misalignments in the guides and relatively low rotational stiffness of the elastomer, the elastomer measurements show significant rotational and out-of-plane behaviour. The hybrid drop test measurements are dominated by elastomer behaviour, because of the high (initial) stiffness ratio between the wire rope spring and the elastomer. This results in non-linear and out-of-plane behaviour of the elastomer.

In the next chapter, the measurement results from this chapter are used to identify and validate the isolator models from chapter 3-5. The wire rope isolator model will be identified by the quasi-static experiments and further validated by the vibrational and shock experiments. The elastomer model will be identified by the quasi-static and vibrational measurements and the drop test experiments will be used for validation. The hybrid isolator is validated by the vibrational and shock measurements.

Chapter 7

Model identification and validation

In previous chapter, the results of three types of experiments were presented. In this chapter, the experimentally obtained data is used to identify and validate the wire rope and elastomer models, which are presented in chapter 3 and 4. The hybrid system model, presented in chapter 5, is only validated. This chapter fully describes the identification of the models, whereas the validation part is only summarized.

In section 7.1, the quasi-static measurements are used to identify the wire rope model. Subsequently, the vibrational and drop test measurements are used to validate this model. In section 7.2, the elastomer model parameters are identified by the quasi-static and vibrational measurements, and the drop test results are used for validation. The hybrid isolator behaviour is validated by vibrational and drop test measurements in section 7.3. Finally, in section 7.4, a summary is given with conclusions on the identification and validation of the models. The full validation is attached in appendix F.

7.1 Wire rope isolator

In chapter 3, the modified Iwan model is used to model the wire rope isolator behaviour. This model describes the hysteretic loop of the isolator. Therefore, the hysteretic loops obtained by the quasi-static measurements are used to identify the model parameters. The other experiments, i.e. the vibrational and drop test experiments, are used for further validation of the identified modified Iwan model.

7.1.1 Identification of the model

Two types of quasi-static measurements are performed with the wire rope isolator: large input global behaviour and small input local behaviour measurements. The resulting hysteretic loops have already been presented in figures 6.2 and 6.3. The modified Iwan model consists of a set of global parameters and local parameters. The global parameters describe the characteristic of the (non-linear) parallel spring, whereas the local parameters describe the Coulomb friction force and linear stiffness of the Jenkin elements. A schematic overview of the parallel series Iwan model with its parameters is shown in figure 3.1, and (3.12) describes the non-linear characteristic of the parallel spring.

An optimization algorithm is used to fit the model on the measurement data and hence to identify the model parameter values. Each type of measurement is performed three times, which means there are three sets of data for both small and large deflections. Each data set is interpolated by a vector with a constant number of equally spaced data points. The deflection vector is assumed to be known input, the force vector is output. Moreover, the objective function to be minimized for each set is defined as a relative root mean square (RMS) error:

$$e = \sqrt{\frac{\sum_{x \in set} (F_{model}(x) - F_{meas}(x))^2}{\sum_{x \in set} F_{meas}(x)^2}} \cdot 100\% \quad (7.1)$$

where $F_{meas}(x)$ and $F_{model}(x)$ are respectively the measured force and the force predicted by the model for a known (measured) deflection x . The non-smooth (non-linear) character of this optimization problem hinders the use of gradient based optimization algorithms. The simplex search method [33] is able to solve non-smooth problems, as long as the problem is unconstrained. The MATLAB routine *fminsearch* is used to solve the optimization problem. The model is only feasible when all stiffnesses and forces are positive. This constraint can not be implemented in the simplex algorithm. A good initial guess is therefore required to ensure that the solver iterates to a feasible solution, and secondly to ensure that the global optimum is found. The optimization problem for an order 2 modified Iwan model consists of the following parameters:

$$par = \left[\underbrace{g_1 \quad g_2 \quad g_3}_{\text{global}} \quad \underbrace{k_{wr,1} \quad F_{c,1} \quad k_{wr,2} \quad F_{c,2}}_{\text{local}} \right] \quad (7.2)$$

Due to the non-linear character, a three stage optimization method, based on the difference in global and local parameters, is used to solve the optimization problem accurately:

- The small deflection data is used to fit the local (i.e. Jenkin elements) parameters and the linear stiffness term g_1 . The non-linear stiffness terms g_2 and g_3 are set to zero.
- The large deflection data is used to fit both the global and local parameters. The initial guess for this problem consists of the optimal parameters of the first optimization and initial guesses for g_2 and g_3 . This results in the final global parameters.
- In last optimization, the global parameters resulting from previous step are fixed. The local parameter are further optimized by the small deflection input.

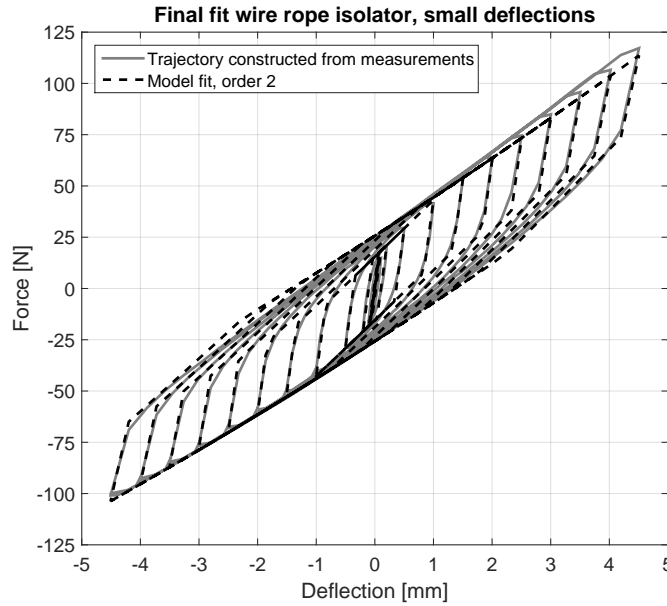


Figure 7.1: Fit wire rope isolator, modified Iwan model order 2, small deflections.

The optimization for a modified Iwan model of order 2 is shown in figure 7.1 for a small deflection set and figure 7.2 for a large deflection set. Note that for both sets the final parameter values are used, which are given in table 7.1. The mean error (7.1) over all three measurement sets for small deflections is 7.70 %, which is reasonable considering the resemblance between the fit and the measurements. The most significant deviation is seen for increasing deflection, the force is slightly underestimated in this region. The mean error (7.1) over all three large deflection sets is 7.07 %. The width of the loop is slightly underestimated in tension and slightly overestimated in compression. The loop width is directly related to the Coulomb forces of the Jenkin elements. The Coulomb force in a single Jenkin element is

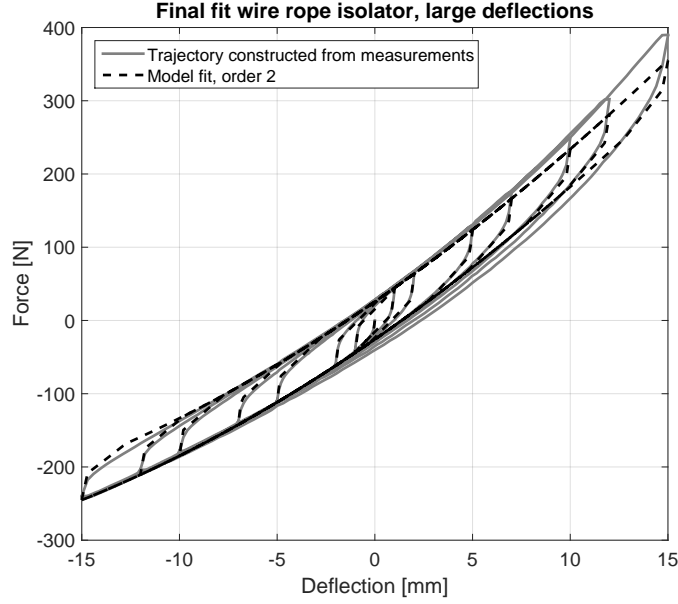


Figure 7.2: Fit wire rope isolator, modified Iwan model order 2, large deflections.

constant and not dependent on the softening and hardening behaviour. Moreover, the loop width of the model is constant when it is projected to the vertical axis, i.e. the actual model loop width increases in softening and decreases in hardening. Despite this limitation, the fit is quite accurate. An increase in the order of the modified Iwan model results only in a marginal decrease in error.

Table 7.1: Fitted wire rope model (i.e. modified Iwan model) parameters.

Parameter	g_1 [N/m]	g_2 [N/m ²]	g_3 [N/m ³]	$k_{wr,1}$ [N/m]	$F_{c,1}$ [N]	$k_{wr,2}$ [N/m]	$F_{c,2}$ [N]
Value	$1.84 \cdot 10^4$	$2.45 \cdot 10^5$	$-4.57 \cdot 10^5$	$1.88 \cdot 10^5$	15.5	$9.09 \cdot 10^3$	10.3

7.2 Elastomer isolator

In chapter 4, the dynamic modelling and behaviour of an elastomer isolator is discussed. The generalized Maxwell model as presented in section 4.2.1 is identified and validated by the measurements presented in section 6.3. The model parameter values are identified by the quasi-static and vibrational experiments, the identified model is used to validate the drop test results.

7.2.1 Identification of the model

The quasi-static experiments (section 6.3.1) and white noise excitation measurements (section 6.3.2) are used to identify the generalized Maxwell model. In figure 4.2, a schematic composition of the model with its parameters is shown. The (linear) static stiffness, $k_{el,0}$, is easily derived from the quasi-static measurements (figure 6.9) and not further discussed here. The white noise excitation measurements are used to identify the parameter values of the Maxwell elements.

In section 6.3.2, elastomer isolation systems with varying top mass (i.e. between 0.99 kg and 6.40 kg) are excited with white noise. In appendix D.1.2, the top mass and isolator mass values are provided. Further, the transmissibility FRF is determined for all three measurements of each (top mass) configuration. These FRF's are used to fit the model of the elastomer isolation system. Note that the frequency range of the measurements is limited to 1-100 Hz (i.e. two decades of frequency). The model can obviously only be

identified in this frequency range. This also means that only two Maxwell elements are needed, i.e. a low order model suffices. Each individual Maxwell element is described by a stiffness ($k_{el,i}$) and a damping constant ($d_{el,i}$). For the identification algorithm, the damping constant is replaced by a time constant $\tau_{el,i}$, given by:

$$\tau_{el,i} = \frac{d_{el,i}}{k_{el,i}} \quad (7.3)$$

It should be noted that the mass of the vibrating elastomer material can not be neglected. The effective mass of the elastomer (m_{eff}) will be modelled as a part of the top mass. For an order 2 generalized Maxwell model, this results in the following parameters to be identified:

$$par = [k_{el,1} \quad k_{el,2} \quad \tau_{el,1} \quad \tau_{el,2} \quad m_{eff}] \quad (7.4)$$

In the identification process, the transmissibility of the model (H_{model}) is compared to the measured transmissibility (H_{meas}). The transmissibility is written as a complex frequency dependent vector. The RMS relative error is given by:

$$e = \sqrt{\frac{1}{N} \sum_{f \in [1,100]} \left(\frac{|H_{model}(f) - H_{meas}(f)|}{|H_{meas}(f)|} \right)^2} \cdot 100\% \quad (7.5)$$

To increase the speed of the identification algorithm bounds are set (stiffnesses: $10^{-1}k_0 - 10^1k_0$, time constants: $10^0 - 10^4 s$), the element sequence is prescribed (increasing $\tau_{el,i}$), and the parameters are scaled (logarithmic from 0 to 1). The generalized Maxwell model is linear. However, it is unknown whether the optimization problem is globally convex and if not, how many (local) solutions exist. For a problem where only one Maxwell element is used and the effective mass is assumed known, only two unknown parameters remain: $k_{el,1}$ and $\tau_{el,1}$. The error can be determined for different combination of these parameters to investigate whether this problem is convex. Figure 7.3 shows the error landscape of the optimization in an 3D diagram. There is only one optimum for this (very broad) parameter range, so this problem seems to be globally convex. However, this does not necessarily ensure convexity for identification problems where a higher order elastomer model is used.

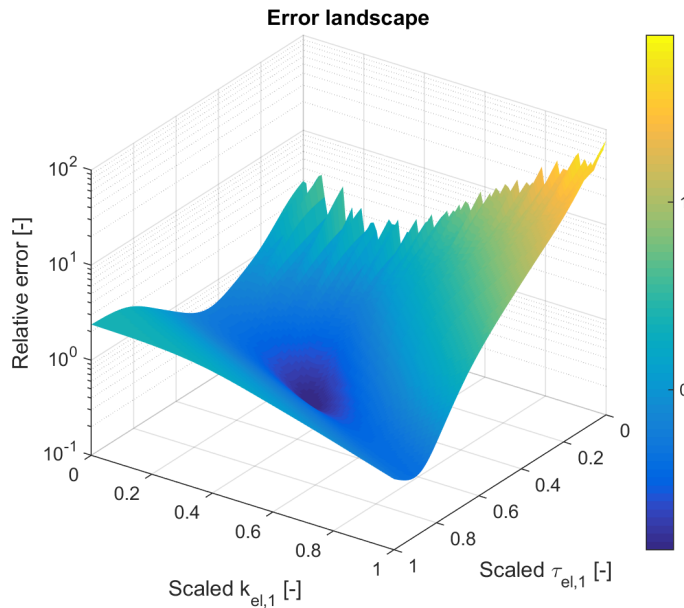


Figure 7.3: Error landscape for a single Maxwell element problem, scaled parameters.

The Newton based sequential quadratic programming (SQP) method is a non-linear gradient based algorithm, which solves smooth global optimization problems [17]. The SQP algorithm, MATLAB routine *fmincon*, is used to identify the elastomer model parameters. Table 7.2 presents the error (7.5) for identifications with different generalized Maxwell model orders. In addition, also the error of the identification of a viscous model (Voigt model, section 4.2.1) is shown.

Table 7.2: Comparison optimizations for different order Maxwell models and viscous model.

Order	Error
1	12.0 %
2	9.4 %
3	8.8 %
4	8.8 %
Viscous	22.0 %

Table 7.2 shows that for increasing generalized Maxwell model order the error decreases up to 3. It is also clear that the generalized Maxwell models are much more accurate than the viscous model. The elastomer behaviour can obviously only be described over the measured frequency range. Although a model of two elements is not optimal, it is sufficient to describe the elastomer behaviour accurately. Moreover, the parameter values of the additional elements of higher order models are fitted at the parameter value boundaries, which is obviously undesired. Using two elements complies with the rule of thumb of one element per decade of frequency [65, 78]. Next to the gradient based SQP method, a global genetic algorithm (GA) [22, 78], MATLAB routine *ga*, is used to validate that indeed the global optimum is found.

The fits of the order 2 generalized Maxwell model coupled to different top masses are shown in figures 7.4 and 7.5, the resulting elastomer characteristic is shown in figure 7.6 and the identified parameters are listed in table 7.3. Coloured lines refer to the measurement results and dashed lines to the identified models. The damping behaviour of the elastomer in the system response is best seen around eigenfrequencies. The eigenfrequencies and the damping behaviour are well described by the fitted models. The system behaviour close to 100 Hz seems to be contradictory in terms of magnitude and phase: the -2 slope is underestimated, whereas the phase is overestimated. A possible cause is the influence of a (higher) internal mode of the elastomer. These dynamics are not included in the model, whereas they experimentally appear at 200 Hz as shown in figure 6.11a.

Table 7.3: Fitted elastomer model (i.e. generalized Maxwell model) parameters.

Parameter	$k_{el,0}$ [N/m]	$k_{el,1}$ [N/m]	$k_{el,2}$ [N/m]	$\tau_{el,1}$ [s]	$\tau_{el,2}$ [s]	m_{eff} [kg]
Value	$1.40 \cdot 10^4$	$3.49 \cdot 10^3$	$1.07 \cdot 10^4$	46.6	841	0.163

As already mentioned, figure 7.6 shows the characteristic of the identified viscoelastic model, i.e. the magnitude and loss factor of the complex stiffness. For low frequencies, the magnitude is close to the static stiffness ($1.40 \cdot 10^4$ N/m), and the loss factor is close to zero. For increasing frequency, both the magnitude and the loss factor increase, i.e. both stiffness and damping increase. Around 10 Hz a plateau in loss factor appears. This region corresponds to the eigenfrequency range of the systems. From the system responses it is clear that the damping is approximately constant in that region. Also for high frequencies the loss factor flattens. This behaviour was already seen in the system responses and is probably related to the higher internal modes of the elastomer. Note that to cope with these effects an extra constraint is added to the identification problem; a positive slope of the loss factor is enforced for increasing frequency.

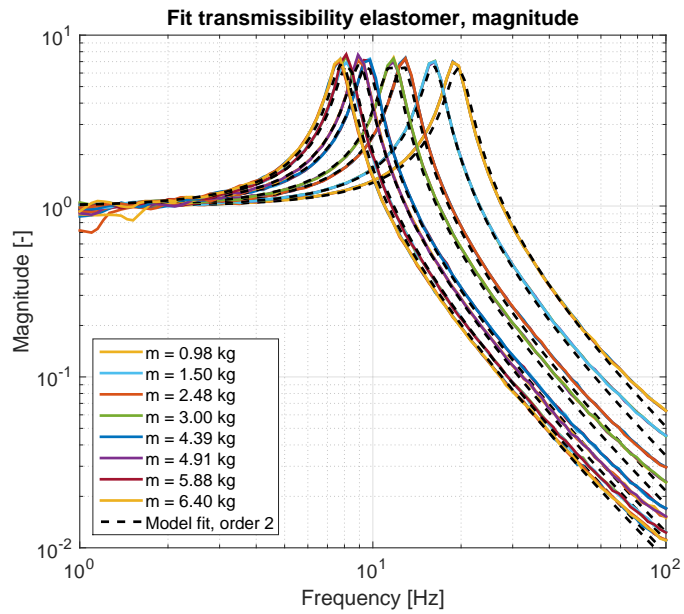


Figure 7.4: Fit elastomer isolation system, magnitude, generalized Maxwell model order 2.

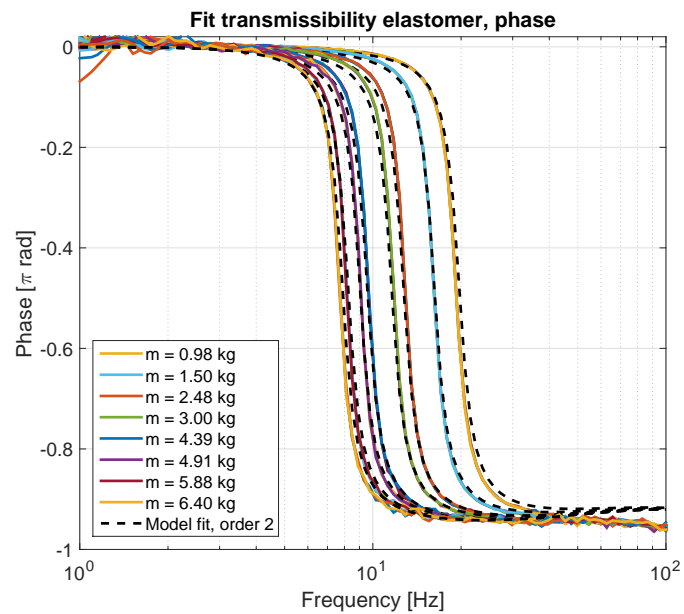


Figure 7.5: Fit elastomer isolation system, phase, generalized Maxwell model order 2.

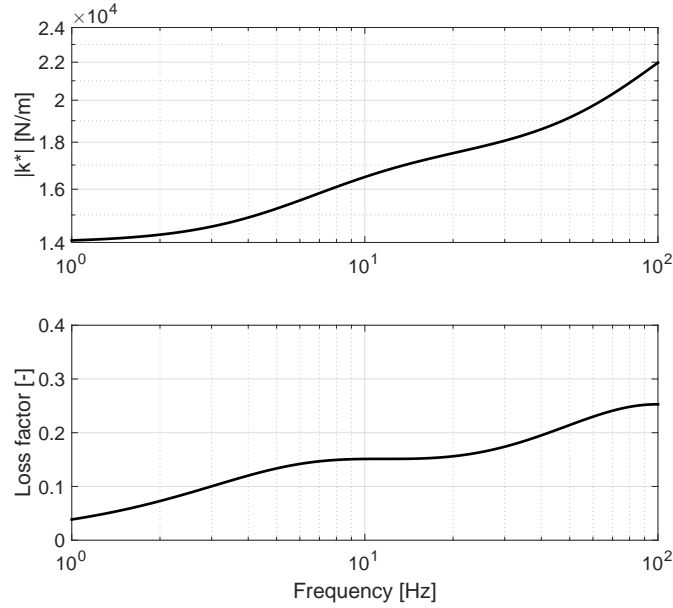


Figure 7.6: Fitted elastomer model, generalized Maxwell model order 2.

7.3 Hybrid isolator

Since the wire rope isolator and the elastomer isolator have been separately identified already in respectively section 7.1 and 7.2, the hybrid measurements are used for validation only. The hybrid isolator model consists of the wire rope model, an intermediate mass, and the elastomer model. Model validation is carried out for harmonic base input and the drop test. A summary of the validation is given in next section, a detailed description of the validation is presented in appendix F.3.

7.4 Summary

In this chapter, the measurement results, as presented in the previous chapter, are used to identify and validate the models. This section provides a short summary of the identification and validation of the isolator models. We start with some remarks on the setups used. Note that the validation is only briefly discussed in this section, a full description of the model validation is presented in appendix F.

The data acquired with the quasi-static experiment is accurate. The only minor disadvantage of this setup is the manual control of the deformation. The shaker setup is used for harmonic excitation. However, there are no controls to realize the desired harmonic base velocity (input) with constant amplitude. Moreover, the amplitude range of the shaker and thus the amplitude range of the input velocity is limited. In the drop test results, several effects are observed which are undesired. More specifically, the measurements show: relaxation and oscillations during the free fall, bounces (after impact) and detachments (in tension) of the bottom mass from the ground floor, and rotational and out-of-plane behaviour of the isolator. These effects are influenced by the mass ratio of the top and bottom mass. In general a high bottom mass reduces the effects of bounce and detachment. Rotational and out-of-plane deformation result from misalignment of the guides and low rotational stiffness of the elastomer isolator.

The wire rope isolator model is identified by the quasi-static measurements using a simplex based optimization algorithm. An order 2 modified Iwan model is identified by a three stage optimization. In the measurements, the hysteretic loop width is dependent on the softening and hardening behaviour. This is not captured by the modified Iwan model. Further, for micro scale input, the model is only able to describe the quasi-static behaviour qualitatively. This also holds for the shaker test results. A quantitative comparison is not possible due to the non-constant amplitude and limited amplitude range

of the measured base velocity input. Moreover, higher harmonics are present in the input, although their magnitudes are small. In the drop test results, relaxation and oscillations during the free fall are only relevant for very small drop heights. Furthermore, friction in air can be neglected. However, bottom mass bounce and detachment have an influence on the response for higher initial velocities (i.e. drop heights). Nevertheless, the model describes the response to shock reasonable accurate. The results confirm that for smaller drop heights, the acceleration in compression is critical, whereas for larger drop heights the acceleration in tension is critical (section 3.4.3).

The elastomer isolator is indirectly identified by its system response on white noise input. However, its static stiffness is identified from the quasi-static experiment. A gradient based SQP method is used to identify the generalized Maxwell model parameters. An order 2 generalized Maxwell model is sufficient to describe the elastomer behaviour over the (limited) frequency range. The frequency range is limited due to an internal (higher order) resonance of the elastomer mount. The large deflection responses in the drop tests indicate non-linear softening behaviour of the elastomer in compression (which in the extreme case involves in hardening). Further, due to low rotational stiffness and slight misalignment in the guiding, there is significant rotational and out-of-plane behaviour of the elastomer isolator. Due to the non-linear character of the elastomer behaviour for larger deformation, the linear generalized Maxwell model is not able to predict the response for large deformations accurately.

The model of the hybrid isolator is derived by combining the models identified for the individual wire rope isolator and the individual elastomer isolator. The shaker and drop test measurements are used for validation of this hybrid model. The response to a harmonic input is qualitatively described by the hybrid model. The vibrational behaviour for low input amplitudes is also quantitatively described. In this region the elastomer is dominant. The drop test results are quite accurately predicted for the low mass system. The compressions are relatively small for this system. The high mass system shows significant rotational and out-of-plane deformation and elastomer non-linearity. These effects are not included in the model and, therefore, there is a significant overestimation of the top mass acceleration and a significant underestimation of the compression (for high initial velocities).

In the next chapter, the identified models are used to perform simulations on the actual isolation system of a transport tool.

Chapter 8

Performance of the isolation system of a transport tool

In previous chapters, the wire rope, elastomer, and hybrid isolation systems were investigated both numerically (chapters 3-5) and experimentally (chapters 6 and 7). The main focus in these chapters was on modelling, analysis, and identification of the isolators and isolation systems. The final objective of this thesis is exploring the use of these (non-linear) isolators in the isolation system of a transport tool for vulnerable instruments. In this chapter, several SDOF isolation systems are numerically analysed and compared using realistic system and input requirements.

The system responses for both realistic random vibrational excitation and shock excitation are examined. Random input is described by a power spectral density spectrum (PSD) of the floor acceleration. For the analysis of non-linear systems, this frequency domain description has to be converted to the time domain. The isolator performance is assessed by the resulting PSD of the top mass acceleration. The response to shock is considered identically to the analysis in previous chapters: by a drop test.

In the first section of this chapter, the typical (isolation) requirements of an NTS transport tool are (further) discussed, and the isolation systems are introduced. In section 8.2, the vibration isolation performance of the different isolation systems is analysed and compared. In section 8.3, the shock absorption properties of the same systems are compared. In last section, a short summary of the obtained results and insights is given.

8.1 Transport tool and requirements

In chapter 1, the concept of a transport tool was already briefly discussed. NTS Group designs and builds these devices to safely transport delicate precision equipment in a truck or airplane. There is a broad range of (environmental) requirements during transport. An isolation system is used for vibration isolation and shock absorption. These two performance indicators are assessed in this chapter. Note that in this thesis, requirements concerning maximum isolator deflection (e.g. due to the limited design space) are not considered.

In total, four isolation systems are compared: a reference system, an elastomer isolation system, a wire rope isolation system, and a hybrid isolation system. The reference system is a viscously damped system (mass-spring-damper system) with an eigenfrequency of 5 Hz , a top mass of 15.0 kg , and a dimensionless damping ratio of 0.07 . The elastomer isolation system consists of the identified elastomer model (section 7.2.1). In the elastomer isolation system, the mass (i.e. 15.4 kg) can be coincidentally chosen such that the same system eigenfrequency and equivalent damping ratio (following (4.5)) is achieved.

Next, the identified wire rope model (section 7.1.1) is used for the wire rope isolation system. The top mass (i.e. 218 kg) is chosen to achieve a 5 Hz resonance frequency for low input amplitude. Note that this system is very lightly damped for small amplitudes, thus the equivalent damping ratio is much lower than 0.07. The hybrid isolation system (figure 5.1) consists of the wire rope model, the elastomer model, an intermediate mass and a top mass. The intermediate mass is set to 1 % of the top mass. The quantity r_k is introduced, which is the stiffness ratio of the wire rope isolator to the elastomer isolator for large input amplitude:

$$r_k = \frac{k_{wr,large\ amplitude,at\ 5Hz}}{k_{el,at\ 5Hz}} \quad (8.1)$$

The stiffness ratio r_k describes the contribution of the wire rope isolator for large input (shock), i.e. systems with a low r_k are more inclined to slip. Moreover, the identified wire rope model is one-to-one copied in the hybrid model and the parameters of the elastomer model are scaled (in magnitude) to achieve the desired r_k . Finally, with the resulting low input amplitude hybrid stiffness, the top mass is chosen to achieve the desired resonance frequency of 5 Hz. This means the top mass depends on the value of r_k .

The vibration isolation requirements are based on the PSD spectrum of the floor and machine acceleration. Standards exist for the input (floor) PSD. However, the European standard is dated [14] and most high-tech customers provide their own input PSD spectrum. Comparing the input spectrum for trucks and airplanes: for road transportation frequencies around 3 Hz are dominant, whereas for air transportation frequencies around 100 Hz are dominant. Therefore, in the vibration isolation analysis several (simplified) flat PSD floor acceleration spectra with different amplitudes are used. The system eigenfrequency of 5 Hz is as low as possible, taken the 3 Hz road transportation dominance in account. The response behaviour is considered over an excitation frequency range from 0.1 Hz to 100 Hz. The upper bound is limited by the validity of the elastomer model, see section 7.2.1. In practice, the (PSD) output requirement for the machine acceleration response is based on the character of the specific protected precision equipment and prescribed by the customer. However, in the current analysis, the output spectra are compared to the response of the viscous reference system.

For shock, a similar approach as in the previously presented numerical and experimental analysis is followed. Simulations are done for different drop heights. For a certain maximal drop height, a maximum absolute acceleration of the top mass is allowed, i.e. the rest shock level has to be minimized using a suitable isolation system. The responses of the different isolation systems are assessed for various drop heights, where the performance is indicated by the rest shock level.

8.2 Vibration isolation

Flat floor acceleration spectra are used as input for the isolation system. The viscous reference system and elastomer isolation system are linear and the PSD of the acceleration of the top (machine) mass can be determined in the frequency domain. Moreover, a change in input amplitude only results in a (proportional) vertical shift in the output PSD of the machine acceleration. When the (complex) transmissibility of the system is given by $H(f)$, the output PSD $S_{yy}(f)$ can be determined by:

$$S_{yy}(f) = |H(f)|^2 S_{xx}(f) \quad (8.2)$$

where $S_{xx}(f)$ is the input PSD. To analyse the non-linear wire rope and hybrid isolation system, the input PSD has to be converted to the time domain, in which the simulations are performed to compute the time history of the acceleration of the top mass. This time signal is converted to the frequency domain and subsequently the PSD of the acceleration response is determined. Note that the output spectrum of the non-linear systems is highly dependent on the input amplitude.

As already mentioned, to perform the time-simulations, the input PSD is transformed to the time domain. A PSD only contains magnitude information; there is no phase information. Therefore, an infinite amount of time realizations exist. To generate a unique realization of the input signal, a unique but randomly chosen phase spectrum is defined. This phase spectrum is conjugate symmetric

with respect to the zero frequency to retrieve a real valued time signal. Multiple realizations are required to mimic a random signal and improve the accuracy of the analysis. Consequently, the simulation time increases. The total simulation time and time step Δt are also dependent on the sample frequency and frequency step Δf . The sample frequency f_n is chosen based on the upper bound of the frequency range of interest (i.e. 0.1-100 Hz). Taking aliasing into account, f_n is set on 800 Hz. A rule of thumb to determine the dimensionless damping of a resonance is inverted to determine the frequency step (Δf). In this method, the -3 dB points of the magnitude of the response around the resonance frequency f_0 are identified. To get an accurate estimation, five frequency points are needed in this range. Then the quantitative analysis is accurate above the following damping ratio:

$$\zeta_{min} = \frac{4\Delta f}{2f_0} \quad (8.3)$$

Using a frequency step $\Delta f = 0.05$ Hz for the analysis of a system with an eigenfrequency of $f_0 = 5$ Hz, the analysis is quantitatively accurate for (equivalent) damping ratios $\zeta > 0.02$. For systems with less damping, the peak (resonance) height is not accurately described, however the qualitative behaviour is described properly. A smaller Δf increases the accuracy, but the computational effort also increases. The time input signal of each PSD input amplitude consists of 30 independent time realizations, i.e. 30 different random phase realizations. The output signal is averaged using a Hanning window and 66.67 % overlap. With these parameters, it seems possible to accurately estimate the output PSD $S_{yy}(f)$. The following accelerations amplitudes (PSD_{input}) and hybrid isolator global stiffness ratios (r_k) are used:

$$PSD_{input} = [10^{-8} \quad 10^{-6} \quad 10^{-5} \quad 10^{-4} \quad 10^{-3} \quad 10^{-2}] \quad [(m/s^2)^2/Hz] \quad (8.4)$$

$$r_k = [0.1 \quad 0.2 \quad 0.4 \quad 0.6 \quad 0.8 \quad 1.0 \quad 1.25] \quad (8.5)$$

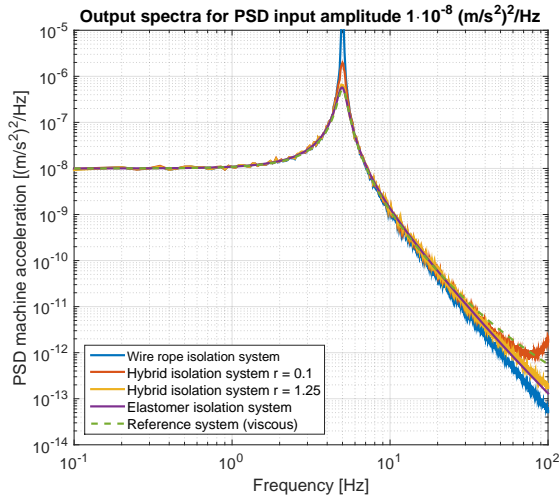
Now the hybrid stiffness ratios are known, the top masses of the hybrid systems can be determined. The top mass values (corresponding to (8.5)) are:

$$m = [101 \quad 65.4 \quad 38.4 \quad 27.2 \quad 21.1 \quad 17.2 \quad 14.0] \quad [kg] \quad (8.6)$$

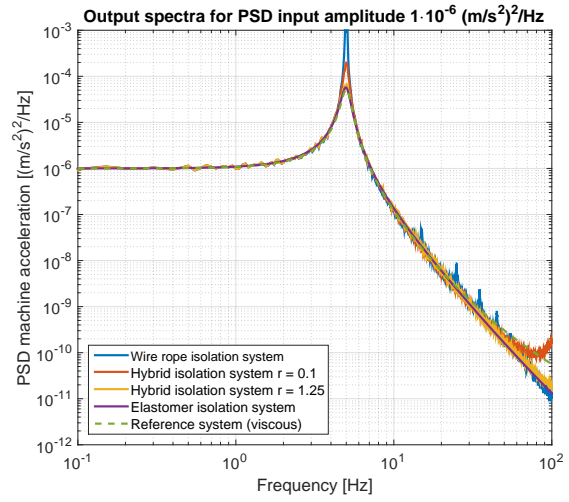
For the wire rope isolation system, the MATLAB Simulink ode3 solver is used. For the hybrid isolation systems, the MATLAB ode45 solver is used. The output PSD spectra of the machine acceleration are shown for each input amplitude separately in figure 8.1. In each sub figure, the responses of the wire rope, elastomer, low ratio hybrid ($r_k = 0.1$), high ratio hybrid ($r_k = 1.25$), and reference system are presented for a different input amplitude. Note that for the linear elastomer and reference system the output PSD is only shifted for varying input amplitude.

Figure 8.1a shows the output PSD for low input amplitude ($1 \cdot 10^{-8} (m/s^2)^2/Hz$). All systems behave linearly. All resonances occur at 5 Hz, but the damping of these resonances differs. The elastomer, high ratio hybrid, and reference system exhibit approximately the same amount of damping (equivalent damping ratio of 0.07). The equivalent damping of the more lightly damped, low ratio hybrid system, is 0.035. Here, the elastomer component is relatively stiffer, and thus less dominant in terms of deformation. The wire rope system is almost undamped. The exact peak height can not be determined, because $\zeta < 0.02$. The high frequency isolation performance is good compared to the reference system. For the reference system the slope for $f \rightarrow \infty$ is -2, due to the viscous character. In the high frequency region, the wire rope behaviour is most profitable, due to the undamped character. The dynamics of the intermediate mass of the $r_k = 0.1$ hybrid configuration are clearly indicated by the increasing magnitude close to 100 Hz. The trend is less significant for the $r_k = 1.25$ hybrid system, the second resonance (dominated by the intermediate mass) is above 100 Hz.

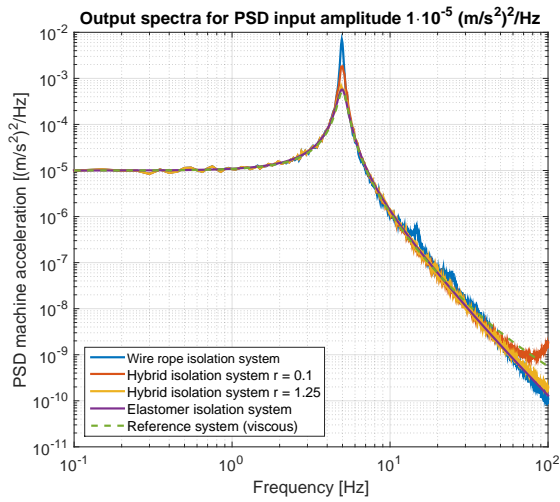
An increase in input to $1 \cdot 10^{-6} (m/s^2)^2/Hz$ (figure 8.1b) or $1 \cdot 10^{-5} (m/s^2)^2/Hz$ (figure 8.1c) leads to non-linear behaviour of the wire rope system, where the other systems still behave linearly. Figure 8.1b shows that the wire rope resonance remains at 5 Hz with very low damping. However, additional peaks appear at 15, 25, 35, 45, and 55 Hz: the odd higher harmonic components of the 5 Hz resonance. This indicates that the friction elements are slipping. Increasing the input to $1 \cdot 10^{-5} (m/s^2)^2/Hz$ (figure 8.1c) results in more wire rope resonance damping (equivalent damping ratio of 0.02). Also the odd higher harmonics exhibit more damping. Note that the resonance frequency is still at 5 Hz.



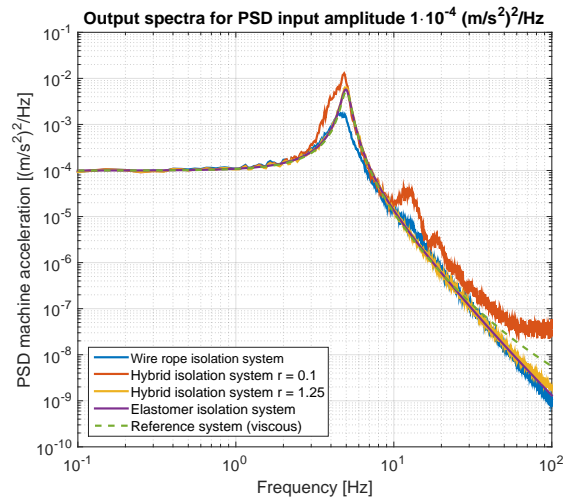
(a) Input amplitude $1 \cdot 10^{-8} (m/s^2)^2/Hz$.



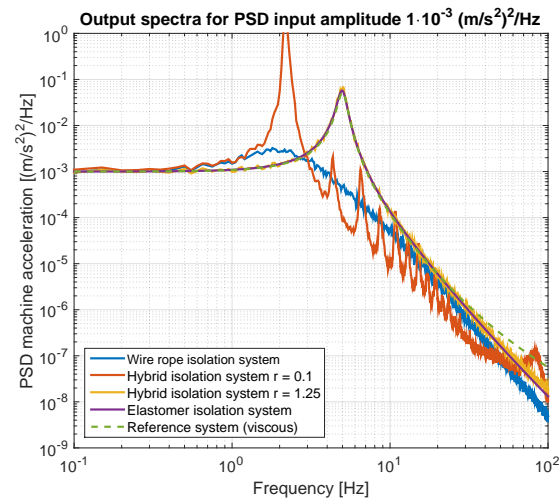
(b) Input amplitude $1 \cdot 10^{-6} (m/s^2)^2/Hz$.



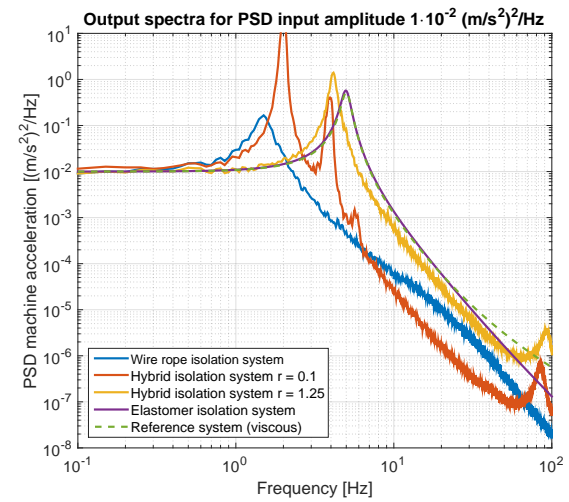
(c) Input amplitude $1 \cdot 10^{-5} (m/s^2)^2/Hz$.



(d) Input amplitude $1 \cdot 10^{-4} (m/s^2)^2/Hz$.



(e) Input amplitude $1 \cdot 10^{-3} (m/s^2)^2/Hz$.



(f) Input amplitude $1 \cdot 10^{-2} (m/s^2)^2/Hz$.

Figure 8.1: Output PSD spectra machine acceleration.

Increasing the floor acceleration input to $1 \cdot 10^{-4} (m/s^2)^2/Hz$ (figure 8.1d) results in non-linear behaviour of both the wire rope and the low ratio hybrid system. The high ratio hybrid system still behaves linearly due to the relative high wire rope stiffness. The resonance frequency of the wire rope system is decreased to $4.5 Hz$ and more heavily damped (equivalent damping ratio of 0.11). Further, the third harmonic at $13.5 Hz$ is also heavily damped, and due to this damping the higher order components visually disappear. The high frequency isolation properties are still close to the high ratio hybrid and the elastomer system. The resonance peak of the low ratio hybrid system is decreased and broadened to around $4.5 Hz$. The amount of damping is slightly increased. The first odd and even higher harmonics appear at 13.5 and $18 Hz$, respectively. This indicates asymmetric non-linear behaviour.

For an input of $1 \cdot 10^{-3} (m/s^2)^2/Hz$, see figure 8.1e, the wire rope and low ratio hybrid system behave non-linearly, where the high ratio hybrid system response is still linear. The resonance frequency of the wire rope system is decreased to $2 Hz$, where the equivalent damping ratio increased to 0.29. The higher order harmonic components are also heavily damped and can not be distinguished in the PSD. The high frequency isolation performance is comparable to the other systems. The resonance frequency of the low ratio hybrid system is decreased to $2.2 Hz$. The dimensionless damping ratio of the resonance peak is low and can not be determined quantitatively. Both even and odd harmonics appear and these are also lightly damped. The behaviour is highly non-linear and asymmetric.

A further input amplitude increase to $1 \cdot 10^{-2} (m/s^2)^2/Hz$, see figure 8.1f, drives the high ratio hybrid system also into its non-linear region. First consider the wire rope system: compared to the PSD of figure 8.1e the resonance frequency is further decreased to $1.5 Hz$, whereas the equivalent damping is now decreased to 0.13 due to stretching of its hysteretic loops. The resonance frequency of the low ratio hybrid system is further decreased to $2 Hz$, with very low damping. The high frequency isolation performance of this system is better compared to the other systems. The resonance frequency of the high ratio hybrid system is decreased to $4 Hz$, where the (equivalent) damping is slightly decreased to 0.04. The resonance of the intermediate mass, i.e. the second resonance of the system, is also shifted downwards into the plotted frequency range, namely to $90 Hz$.

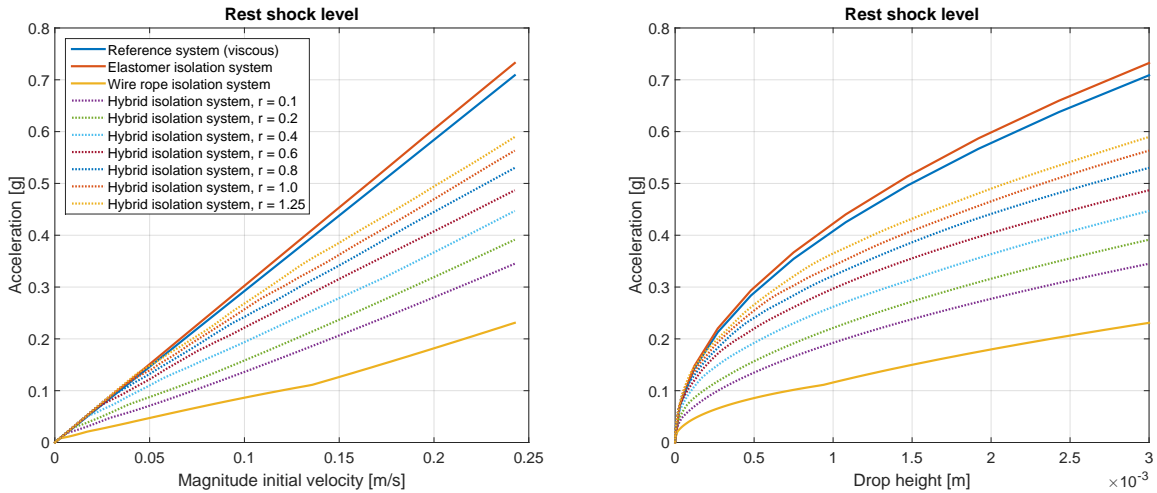
In these simulations, the wire rope isolator is beneficial for all random inputs with PSD equal to or higher than $1 \cdot 10^{-4} (m/s^2)^2/Hz$ in terms of cumulative power. However, comparing to the reference system, the elastomer system performance is close to the reference, independent of input, whereas the the wire rope system performance only suffices for an PSD input of $1 \cdot 10^{-4} (m/s^2)^2/Hz$. Further, also the randomness of the input and the direct use of the identified model of the measured wire rope isolator affect the response. The real input spectrum is not random due to periodicity in the road profile for trucks and dominant harmonics of the propulsion system for airplanes. This means the phase realization of the input signal is not random. Another important aspect is scaling of the isolators for practical applications (with much higher mass). The linear elastomer model scales linearly. However, the wire rope model can not be scaled in a straight forward manner. Wire rope isolators with larger dimensions also start to slip for higher input, resulting in a different response for the same PSD amplitude.

8.3 Shock absorption

Shock simulations are done for a conditioned free fall: relaxation, dynamics in air, bounce (after impact), and bottom mass detachment (in tension) are not considered. The simulation starts at the moment of impact; the floor is fixed (the bottom mass is not modelled), where the top mass and the intermediate mass (if applicable) have an initial velocity following the energy balance (3.18). This is a good approximation. The measurements showed that relaxation is only relevant for very small drop heights and friction in air can be neglected (section 7.4). The customer requirements describe that the transport tool is subjected to shock when it is rigidly placed inside a shipping container. Therefore, the bottom mass (floor) can be assumed heavy compared to the top mass (machine) and the effects of bounce and bottom mass detachment are small (section 7.4). The simulations start at the moment of impact, from that time the bottom remains on the ground. Consequently, there is no need to model the bottom mass. The conditioned free fall simulations are valid to make a first approximation of the shock response.

The maximum absolute acceleration (rest shock level) is determined as function of initial impact velocity and drop height. For a symmetric system (identical behaviour in compression and tension), the rest shock level coincides with the moment when the isolator is fully compressed. However, asymmetric soft-hardening behaviour can cause the maximal rest shock level to coincide with the moment that the isolator is fully stretched (section 7.4).

The reference, elastomer, wire rope, and hybrid systems (from section 8.2) are analysed for shock. Figure 8.2a shows the rest shock level as function of impact velocity. The top mass accelerations of the linear systems (i.e. the reference system and the elastomer system) are close to proportional with respect to the initial velocity, as already indicated in section 4.3.2. The small difference in damping causes the small differences in response. The wire rope isolation system also exhibits linear behaviour for very small velocities up to 0.01 m/s , i.e. the friction elements stick up to 0.01 m/s . For higher initial velocities, due to slip, the wire rope isolator stiffness decreases and consequently, the slope of rest shock level decreases. For increasing velocity, the softening behaviour causes the slope to flatten even further. For initial velocities higher than 0.14 m/s , the maximal (absolute) acceleration occurs in tension instead of in compression. Consequently, the slope increases. Figure 8.2a clearly shows that the response of the hybrid systems is bounded by the elastomer and wire rope system. For increasing r_k , the initial velocity at which slip occurs for the first time increases, and consequently, the rest shock level is higher. For an increasing ratio, relatively less energy is absorbed by the wire rope, while the elastomer is absorbing more energy. The performance (i.e. minimal rest shock level) is best for hybrid systems which characteristic is close to the wire rope isolation system, i.e. hybrid systems should have a low r_k . Figure 8.2b shows the rest shock level as function of drop height. The square root dependency of the drop height is shown, as described by (3.19). The figure clearly shows the advantage of the wire rope and hybrid systems: the rest shock level is already lowered for drop heights close to zero.



(a) Rest shock level as function of velocity.

(b) Rest shock level as function of drop height.

Figure 8.2: Maximum absolute top mass acceleration.

8.4 Summary

The simulations in this chapter clearly showed the difference in the vibrational and shock behaviour of elastomer, wire rope, and hybrid isolation systems. Basically, the hybrid system behaviour is bounded by the wire rope and elastomer system behaviour. Preferably, the elastomer behaviour is dominant for vibrational (low amplitude) input for its resonance damping properties. For shock (large amplitude) input, the wire rope is dominant. The non-linear character of the wire rope isolator is advantageous, to reduce the rest shock level. These apparently contradictory conclusions can be met using a hybrid system due to the amplitude dependent character of the wire rope isolator.

Chapter 9

Conclusions and recommendations

In this thesis, the use of linear and non-linear passive vibration isolators in floor excited isolation systems is explored. In particular, three type of isolators are considered: a linear elastomer isolator, a non-linear wire rope isolator, and a series connection of these components (i.e. a hybrid isolator). In first part of this thesis, the characteristic behaviour of the isolators is modelled and analysed. In this analysis, harmonic and shock input are considered. Secondly, several experiments are performed to identify and validate the models. Lastly, simulations are done to analyse and compare the isolation systems for realistic inputs. In this chapter, the final conclusions (section 9.1) and recommendations (section 9.2) are presented.

9.1 Conclusions

Before we will give a conclusion of the main objective stated in section 1.2, the sub objectives are discussed. The dynamic behaviour of wire rope isolators is highly amplitude dependent. For small deformations the behaviour is stiff and close to undamped. For increasing deformations the cable strands start to slide, resulting in decreasing stiffness and increasing damping. Further, the quasi-static behaviour is characterized by softening in compression and hardening in tension. The modified Iwan model describes the amplitude dependent hysteretic loop of the wire rope isolator accurately (chapter 3). The modified Iwan model is a phenomenological model, which however consists of spring and Coulomb friction elements which have a clear physical meaning. The order of the model determines the model complexity and the smoothness of the hysteretic loops. The C^0 continuous model equations are no problem for a regular ode solver. A modified Iwan model of order 2 is capable of describing the quasi-static experimental behaviour accurately. Gradient based optimization algorithms can not solve the non-smooth identification problem. Therefore, a simplex algorithm is used (section 7.1). The wire rope isolator is highly profitable for shock (large deformations) and vibration (small deformation) isolation. However, the performance is less for small deformation resonance damping.

The dynamic behaviour of an elastomer isolator is frequency, temperature, and geometry dependent. In this thesis, a specific geometry and constant temperature is assumed, resulting in a model which is only frequency dependent. For low frequencies, the stiffness and damping are low (rubber phase). For high frequencies, the stiffness is high and the damping is low (glass phase). The transition frequency region shows a gradually increase in stiffness and significant resonance damping. Note that this (broad) transition frequency region is spanned by typically eight decades of frequency. A linear generalized Maxwell model of order 10 is able to describe the elastomer behaviour both in the time and frequency domain (chapter 4). In measurements, small (vibrational) deformations are studied in the frequency range from 1 to 100 Hz (section 6.3). A generalized Maxwell model of order 2 is sufficient to describe the elastomer behaviour over this (limited) frequency range. A gradient based algorithm is used to identify the model parameters (section 7.2). The elastomer isolation system exhibits good vibrational damping and isolation properties. The response to shock however, is not as good as for the wire rope system. Further, measurements show non-linear behaviour for large deformations. This is related to the non-uniform geometry of the specific elastomer mount.

To conclude about the main objective stated in section 1.2, the hybrid isolator is indeed suitable to combine the (large deformation) shock absorbing properties of the wire rope isolator and the small signal (vibrational) damping properties of the elastomer isolator. For small deformations the wire rope is stiff and, consequently, the elastomer component dominates the overall stiffness and damping. For increasing input amplitude, the cable strands start to slide and the wire rope stiffness decreases, resulting in beneficial shock absorption properties. The hybrid isolator model consists of the two component models and a small intermediate mass. When the elastomer behaviour is modelled over a broad frequency range, a stiff solver is needed to simulate the behaviour of the hybrid isolation system. The stiff implicit solver can not solve non-smooth problems. Therefore, the stick-slip transitions are smoothed (chapter 5). The simulation results qualitatively match the experimentally obtained results (section 6.4 and 7.3).

The experiments are performed at three different measurement setups: we distinguish quasi-static measurements, shaker (vibrational) measurements, and drop test measurements (chapter 6). On a manually controlled lathe the quasi-static behaviour of the wire rope and elastomer isolator is derived accurately. The shaker measurements are used to derive the linear elastomer system response using white noise input. Secondly, all isolation systems are excited with harmonic input to validate the simulations results. The electromechanical shaker setup has a (weakly) non-linear relation between input voltage and shaker table displacement and application of a harmonic voltage will therefore not result in a harmonic shaker table motion. A fair quantitative comparison between the shaker measurements and the simulations is difficult to make. A qualitative comparison, however, can be made and shows good agreement. A drop test setup is purpose-built for this project. The experimental shock response is sometimes quantitatively but mostly qualitatively described by the models. Relaxation and oscillation during the free fall, and bottom mass bounce and detachment are not covered by the simulation model. The significance of these effects is dependent on drop height and top to bottom mass ratio of the isolator. Small drop heights and large mass ratios reduce these effects. Due to the alignment problems and the relatively low rotational stiffness of the isolators, undesired out-of-plane and rotational behaviour occurs for larger drop heights (chapter 7).

In chapter 8, simulations with realistic inputs are done to compare the response of several isolator configurations to vibrational input and shock. Hybrid systems with different stiffness ratios between the wire rope and elastomer component are used. A flat PSD floor acceleration spectrum is used as vibrational input; several input PSD amplitudes are considered. The output (isolation performance) is assessed by the PSD spectrum of the machine acceleration. For vibration isolation the elastomer performance is good and independent of the amplitude. The performance of the wire rope and hybrid systems is highly dependent on the input amplitude. The conditioned free fall simulations are similar to the simulations in previous chapters. The shock response of the hybrid systems is bounded by that of the elastomer and wire rope isolation system. For shock absorption a system with a dominant wire rope component is beneficial. Considering the overall performance of an isolation system for vibration isolation and shock absorption, the use of hybrid isolators with respect to single wire rope or elastomer isolators is beneficial, however, the specific component selection is much more complex (chapter 8).

9.2 Recommendations for further research

Further research should be focussed on two main aspects: improving the model descriptions and validation, and, most important, implementation of the hybrid damper.

Due to the wire rope amplitude dependency, there are three distinguishable characteristic wire rope regimes: a regime with linear undamped behaviour (micro scale), a regime which is characterized by stick-slip transitions (local behaviour) and a regime with large deformations (global behaviour). The modified Iwan model can be improved by relating the width of the hysteretic loop to the soft-hardening (global) behaviour. Next, in the model parameter identification process, most emphasis is on the local and global behaviour. Including the micro scale behaviour in the identification process will increase the model accuracy on micro scale (section 7.1).

The current linear elastomer model is not able to describe the non-linear behaviour occurring for large deformations and the second internal mode of the measured (non-uniform) elastomer mount. This can be resolved by testing an elastomer mount with a more uniform geometry or by introducing non-linear terms in the elastomer model. To explore the use and design of a hybrid isolator, the first suggestion is preferred. A non-linear elastomer model will increase the complexity of the hybrid model even more. Next, the elastomer model is now identified indirectly by the system response. The dynamics of the elastomer are mostly related to the system behaviour around the eigenfrequency. With a more direct measurement, where not the whole dynamic system but only the elastomer material is characterized, the elastomer model can be identified more accurately (section 7.2).

The measurement setups and conditions can be improved to increase the accuracy and quality of the measurement results. The load in the quasi-static tests is now manually applied. A controlled actuator will improve the input profile character. The velocity input amplitude of the shaker table is non-flat and not harmonic. A well designed control system (e.g. a repetitive controller) may be introduced to enforce the shaker table to move with a harmonic motion at the desired amplitude and frequency. The drop test setup may be improved by introducing a metrology frame to minimize external noise in the measured position and velocity signals. Furthermore, the design can be improved to reduce the effects of out-of-plane and rotational behaviour by reducing misalignments in the vertical guidance. Relaxation and oscillations during the free fall and bottom mass bounce and detachment are physical phenomena, which can not be excluded from the measurements; in the future these effects should be implemented in the simulations (chapter 6).

After improving the hybrid model and the experimental setups, again a model validation needs to be carried out. Scaling of the elastomer model is straight forward, whereas scaling of the wire rope model is not. Several types of wire rope isolators (with varying dimensions) have to be measured, identified, and validated. Once a satisfactory model validation has been carried out, the models can be used for design optimization. A methodology has to be developed and implemented in a design tool to actually accomplish the design of a suitable hybrid isolator. The methodology can consider only the deflection of the isolator and its components for different types of input and amplitudes (as done in this thesis). However, another possibility is considering the energy dissipation of the isolator and its components instead of only their deflection. The latter is far from trivial and will need further study.

Bibliography

- [1] K. Adolfsson, M. Enelund, and P. Olsson. On the Fractional order model of viscoelasticity. *Mechanics of Time-Dependent Materials*, 9:15–34, 2005.
- [2] F. Al-Bender, V. Lampaert, and J. Swevers. The Generalized Maxwell-slip model: A novel model for friction simulation and compensation. *IEEE Transactions on Automatic Control*, 50(11):1883–1887, 2005.
- [3] R.L. Bagley and P.J. Torvik. On the Fractional calculus model of viscoelastic behaviour. *Journal of Rheology*, 30(1):133–155, 1986.
- [4] X.M. Bai, B.M. Shah, L.M. Keer, Q.J. Wang, and R.Q. Snurr. Particle dynamics simulations of a piston-based particle damper. *Powder Technology*, 189:115–125, 2009.
- [5] R. Bouc. Forced vibration of a mechanical system with hysteresis. In *Proceedings of the Fourth Conference on Non-linear Oscillation*, volume 315, 1967.
- [6] S. Chaudhuri and B. Kushwaha. Wire rope based vibration isolation fixture for road transportation of heavy defence cargo. *Vibration Problems ICOVP*, 8:61–67, 2007.
- [7] R.G. Cobb, J.M. Sullivan, A. Das, L.P. Davis, T.T. Hyde, T. Davis, Z.H. Rahman, and J.T. Spanos. Vibration isolation and suppression system for precision payloads in space. *Smart Materials and Structures*, 8(6):798–812, 1999.
- [8] G.A. Costello. Mechanics of wire rope. In *Mordica Lecture Interwire*. Wire Association International, 2003.
- [9] P.G. Cranston, F.W. Kan, and A.T. Sarawit. Modelling the seismic behaviour of Giant Magellan Telescope (GMT) primary mirror support system. In *Proceedings of SPIE Ground-based and Airborne Telescopes IV*, 2012.
- [10] M.A. Cutchins, J.E. Cochran Jr., K. Kumar, N.G. Fitz-Coy, and M.L. Tinker. Initial investigations into the damping characteristics of wire rope vibration isolators. Technical report, Engineering Experiment Station Auburn University, Auburn, 1987.
- [11] Y. Duan and Q. Chen. Simulation and experimental investigation on dissipative properties of particle dampers. *Journal of Vibration and Control*, 17(5):777–788, 2011.
- [12] M.R. Duncan, C.R. Wassgren, and C.M. Krousgrill. The damping performance of a single particle damper. *Journal of Sound and Vibration*, 286:123–144, 2005.
- [13] S.J. Elliot, M. Serrand, and P. Gardonio. Feedback stability limits for active isolation systems with reactive and inertial actuators. *Journal of Vibrations and Acoustics*, 123:250–261, 2001.
- [14] European Committee for Electrotechnical Standardization (CENELEC). *Classification of environmental conditions Part 3: Classification of groups of environmental parameters and their severities Section 2: Transportation*, March 1997. EN 60721-3-2:1997.
- [15] R.H.B. Fey, D.H. van Campen, and A. de Kraker. Long term structural dynamics of mechanical systems with local nonlinearities. *Journal of Vibration and Acoustics*, 118:147–153, 1996.

- [16] A. Fidlin and M. Lobos. On the limiting of vibration amplitudes by a sequential friction-spring element. *Journal of Sound and Vibration*, 333:5970–5979, 2014.
- [17] R. Fletcher. *Practical methods of optimization, second edition*. Wiley, Chichester, 2000.
- [18] B.L. Fowler, E.M. Flint, and S.E. Olson. Design methodology for particle damping. In *Proceedings of SPIE*, number 4331, pages 186–197, 2001.
- [19] R.D. Friend and V.K. Kinra. Particle impact damping. *Journal of Sound and Vibration*, 233(1):93–118, 2000.
- [20] M.I. Friswell, D.J. Inman, and M.J. Lam. On the realisation of GHM models in viscoelasticity. *Journal of Intelligent Material Systems and Structures*, 8(11):986–993, 1997.
- [21] L. Gaul, P. Klein, and S. Kemple. Damping description involving Fractional operators. *Mechanical Engineering and Signal Processing*, 5(2):81–88, 1991.
- [22] D.E. Goldberg. *Genetic algorithms in search, optimization and machine learning*. Addison-Wesley, Reading, 1989.
- [23] J.A.J.M. Hoof. Nonlinear vibration control in flexible structures using piezoelectric materials, DC2013.55. Master’s thesis, Eindhoven University of Technology, Eindhoven, 2013.
- [24] J.A.J.M. van Hoof, R.H.B. Fey, A. Shukla, and H. Nijmeijer. Effect of hinge friction on the steady-state response of base-excited shallow arches. *Journal of Vibration and Control*, 20(12):1877–1894, 2014.
- [25] R.A. Ibrahim. Recent advances in nonlinear passive vibration isolators. *Journal of Sound and Vibration*, 314:371–452, 2008.
- [26] W.D. Iwan. A distributed-element model for hysteresis and its steady-state dynamic response. *Journal of Applied Mechanics*, 33:893–900, 1966.
- [27] W.D. Iwan. The distributed-element concept of hysteretic modelling and its application to transient response problems. *International Journal of Non-linear Mechanics*, 4:45–57, 1969.
- [28] M. Jean and J.J. Moreau. Dynamics in the presence of unilateral contacts and dry friction: a numerical approach. In *CISM Lectures*, volume 304, pages 131–196, 1987.
- [29] J. Kanehara. Open space project: Modelling and simulation of the 4-link biped robot with Coulomb friction by time-stepping method. Technical report, Eindhoven University of Technology, Eindhoven, 2009.
- [30] D. Karnopp. Active and semi-active vibration isolation. *Journal of Vibration and Acoustics*, 177:177–185, 1995.
- [31] J.E. Kollmer, A. Sack, M. Heckel, and T. Pschel. Relaxation of a spring with an attached granular damper. *New Journal of Physics*, 15:093023, 2013.
- [32] A. Kyprianou and K. Worden. Identification of hysteretic systems using the differential evolution algorithm. *Journal of Sound and Vibration*, 248(2):2001, 2001.
- [33] J.C. Lagarias, J.A. Reeds, M.H. Wright, and P.E. Wright. Convergence properties of the Nelder-Mead simplex method in low dimensions. *SIAM Journal of Optimization*, 9(1):112–147, 1998.
- [34] V. Lampaert, J. Swevers, and F. Al-Bender. Modification of the Leuven integrated friction model structure. *IEEE Transactions on Automatic Control*, 47:683–687, 2002.
- [35] D.F. Ledezma-Ramirez, N.S. Ferguson, and M.J. Brennan. Shock isolation using an isolator with switchable stiffness. *Journal of Sound and Vibration*, 330:868–882, 2011.
- [36] R.I. Leine and H. Nijmeijer. *Dynamics and bifurcations of non-smooth mechanical systems, LNACM vol. 18*. Springer-Verlag, Heidelberg, 2004.

- [37] Y. Liu. *Semi-active damping control for vibration isolation of base disturbances*. PhD thesis, Institute of Sound and Vibration Research University of Southampton, Southampton, 2004.
- [38] Y. Liu, H. Matsuhisa, and H. Utsuno. Semi-active vibration isolation system with variable stiffness and damping control. *Journal of Sound and Vibration*, 313:16–28, 2008.
- [39] Y. Liu, T.P. Waters, and M.J. Brennan. A comparison of semi-active damping control strategies for vibration isolation of harmonic disturbances. *Journal of Sound and Vibration*, 280:21–39, 2005.
- [40] N.J. Mallon. *Dynamic stability of thin-walled structures: a semi-analytical and experimental approach*. PhD thesis, Eindhoven University of Technology, Eindhoven, 2008.
- [41] N.J. Mallon, R.H.B. Fey, and H. Nijmeijer. Dynamic stability of a base-excited thin orthotropic cylindrical shell with top mass: Simulations and experiments. *Journal of Sound and Vibration*, 329:3149–3170, 2010.
- [42] K. Mao, M.Y. Wang, Z. Xu, and T. Chen. DEM simulation of particle damping. *Powder Technology*, 142:154–165, 2004.
- [43] L.A. Martin. *A novel material modulus function for modelling viscoelastic materials*. PhD thesis, Virginia Polytechnic Institute and State University, Blacksburg, 2011.
- [44] D.J. Mead. *Passive vibration control*. Wiley, Chichester, 1998.
- [45] K. van de Meerakker, R. Donker, and I. Widdershoven. Damper update: Squeeze film and daspot damping. Preliminary Investigation Report ASML, 2010.
- [46] J. Michielsen, R.H.B. Fey, and H. Nijmeijer. Steady-state dynamics of a 3D tensegrity structure: Simulations and experiments. *International Journal of Solids and Structures*, 49:973–988, 2012.
- [47] M.I. Molina. Exponential versus linear amplitude decay in damped oscillators. *The Physics Teacher*, 42:485–487, 2004.
- [48] Y.Q. Ni, J.M. Ko, C.W. Wong, and S. Zhan. Modelling and identification of a wire-cable vibration isolator via a cyclic loading test, Part 1: Experiments and model development. In *Proceedings of the Institution of Mechanical Engineers*, volume 213, pages 163–171, 1999.
- [49] Y.Q. Ni, J.M. Ko, C.W. Wong, and S. Zhan. Modelling and identification of a wire-cable vibration isolator via a cyclic loading test, Part 2: Identification and response prediction. In *Proceedings of the Institution of Mechanical Engineers*, volume 213, pages 173–182, 1999.
- [50] P.W.J.M. Nuij. *Higher order sinusoidal input describing functions: Extending linear techniques towards non-linear systems analysis*. PhD thesis, Eindhoven University of Technology, Eindhoven, 2007.
- [51] P.W.J.M. Nuij and D.J. Rijlaarsdam. Introduction to frequency response function measurements part 1: The transformation from time to frequency domain. *Mikroniek, Professional Journal on Precision Engineering*, 54(2):3–13, 2014.
- [52] P.W.J.M. Nuij and D.J. Rijlaarsdam. Introduction to frequency response function measurements part 2: From signal analysis to system analysis. *Mikroniek, Professional Journal on Precision Engineering*, 54(3):32–38, 2014.
- [53] P.W.J.M. Nuij and M. Steinbuch. Bias removal in Higher Order Sinusoidal Input Describing Functions. In *IEEE International Instrumentation and Measurement Technology Conference. Victoria, Vancouver Island, Canada*, 2008.
- [54] S.E. Olson. An analytical particle damping model. *Journal of Sound and Vibration*, 264:1155–1166, 2003.
- [55] W.A.W.A. Oomen. Embedding a dynamic vibration absorber system in a porous material, DC2014.53. Master’s thesis, Eindhoven University of Technology, Eindhoven, 2014.

- [56] A. Papalou and S.F. Masri. An experimental investigation of particle dampers under harmonic excitation. *Journal of Vibration and Control*, 4:361–379, 1998.
- [57] S.W. Park. Rheological modelling of viscoelastic passive dampers. In *Proceedings of SPIE*, number 4331, pages 343–354, 2001.
- [58] P.T. Piiroinen and Y.A. Kuznetsov. An event-driven method to simulate Filippov systems with accurate computing of sliding motions. In *ACM Transactions on Mathematical Software*, volume 34, 2008.
- [59] K. Popp, L. Panning, and W. Sextro. Vibration damping by friction forces: Theory and applications. *Journal of Vibration and Control*, 9:419–448, 2003.
- [60] T. Pritz. Five-parameter Fractional derivative model for polymeric damping materials. *Journal of Sound and Vibration*, 9:15–34, 2003.
- [61] D.J. Rijlaarsdam and P.W.J.M. Nuij. Introduction to frequency response function measurements part 3: Frequency domain modelling and performance optimisation of non-linear systems. *Mikroniek, Professional Journal on Precision Engineering*, 54(4):22–28, 2014.
- [62] M.W.L.M. Rijnen, F. Pasteuning, R.H.B. Fey, G. van Schothorst, and H. Nijmeijer. A numerical and experimental study on viscoelastic damping of a 3D structure. *Journal of Sound and Vibration*, 349:80–98, 2015.
- [63] E.I. Rivin. Vibration isolation of precision equipment. *Precision Engineering*, 17:41–56, 1995.
- [64] E.I. Rivin. *Passive vibration isolation*. ASME Press, New York, 2003.
- [65] T Ruijl. Technical note: Damper development, rubber general. Preliminary Investigation Report MI Partners, 2012.
- [66] M. Saeki. Impact damping with granular materials in a horizontally vibration system. *Journal of Sound and Vibration*, 251(1):153–161, 2002.
- [67] D. Sauter. *Modelling the dynamic characteristics of slack wire cables in Stockbridge dampers*. PhD thesis, Technischen Universität Darmstadt, Darmstadt, 2003.
- [68] D. Sauter and P. Hagedorn. On the hysteresis of wire cables in Stockbridge dampers. *Journal of Non-linear Mechanics*, 37:1453–1459, 2002.
- [69] W. Schwanen. Modelling and identification of the dynamic behaviour of a wire rope spring, DC2004.28. Master’s thesis, Eindhoven University of Technology, Eindhoven, 2004.
- [70] D.J. Segalman. An initial overview of Iwan modelling for mechanical joints. Technical report, Sandria National Laboratories, Albuquerque, 2001.
- [71] D.J. Segalman and M.J. Starr. Inversion of Masing models via continuous Iwan systems. *International Journal of Non-linear Mechanics*, 43:74–80, 2008.
- [72] B.M. Shah, D. Pillet, X.M. Bai, L.M. Keer, Q.J. Wang, and R.Q. Snurr. Construction and characterization of a piston-based thrust damping system. *Journal of Sound and Vibration*, 326:489–502, 2009.
- [73] C.W. de Silva. *Vibration damping, control, and design*. Taylor and Francis, Boca Raton, 2007.
- [74] D.E. Stewart and J.C. Trinkle. An implicit time-stepping scheme for rigid body dynamics with inelastic collisions and Coulomb friction. *International Journal for Numerical Methods in Engineering*, 39:2673–2691, 1996.
- [75] C.W. Studer. *Augmented time-stepping integration of non-smooth dynamical systems*. PhD thesis, ETH Zrich, Zrich, 2008.

- [76] M.A. Trindade, A. Benjeddou, and R. Ohayon. Modelling of frequency-dependent viscoelastic materials for active-passive vibration damping. *Journal of Vibrations and Acoustics*, 122:169–174, 2000.
- [77] A.K. van der Vegt and L.E. Govaert. *Polymeren: Van keten to kunststof*. DUP Blue Print, Delft, 5 edition, 2003.
- [78] C.A.M. Verbaan. *Robust mass damper design for bandwidth increase of motion stages*. PhD thesis, Eindhoven University of Technology, Eindhoven, 2015.
- [79] E.L.B. Vorst, D.H. van Campen, R.H.B. Fey, and A. de Kraker. Determination of global stability of steady-state solutions of a beam system with discontinuous support using Manifolds. *Chaos, Solitons & Fractals*, 7(1):61–75, 1996.
- [80] Y.K. Wen. Method for random vibration of hysteretic systems. *Journal of Engineering Mechanics*, 100(2):249–263, 1976.
- [81] N. van de Wouw. An introduction to time-stepping: a numerical technique for mechanical systems with unilateral constraints. Eindhoven University of Technology.
- [82] S.L. Xie, Y.H. Zhang, C.H. Chen, and X.N. Zhang. Identification of nonlinear hysteretic systems by artificial neural network. *Mechanical Systems and Signal Processing*, 34:76–87, 2013.
- [83] N. Zhou and K. Liu. A tunable high-static-low-dynamic stiffness vibration isolator. *Journal of Sound and Vibration*, 329:1254–1273, 2010.

Appendix A

Additional simulation results wire rope analysis

In this appendix, additional simulation results of the wire rope analysis are shown. In section A.1, a system with parallel Coulomb-spring element is studied, in the remainder of this appendix the wire rope isolation system is considered. In these sections, the system parameters (A.2), additional frequency-amplitude diagrams of the symmetric wire rope system (A.3), additional time histories of the asymmetric wire rope system (A.4), and additional shock response figures (A.5) are shown.

A.1 Simulations parallel Coulomb-spring element

The simulation results, discussed in section 3.3.1, are shown in this appendix.

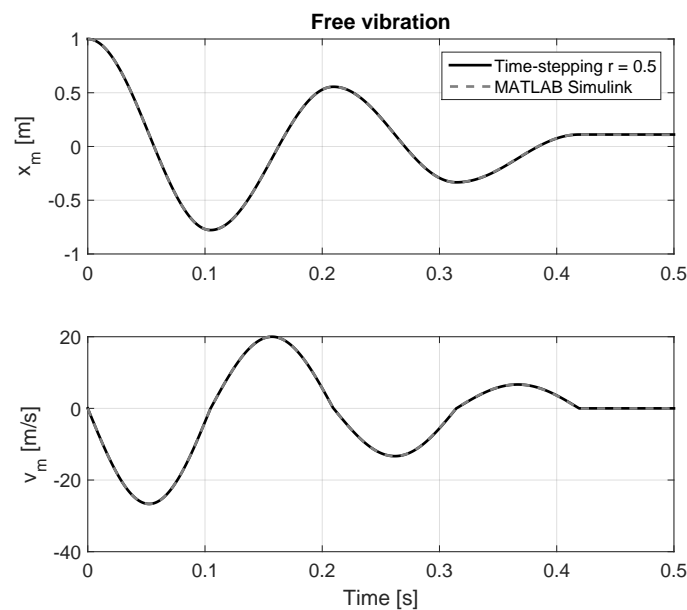


Figure A.1: Free vibration parallel Coulomb-spring system, time-stepping and Simulink.

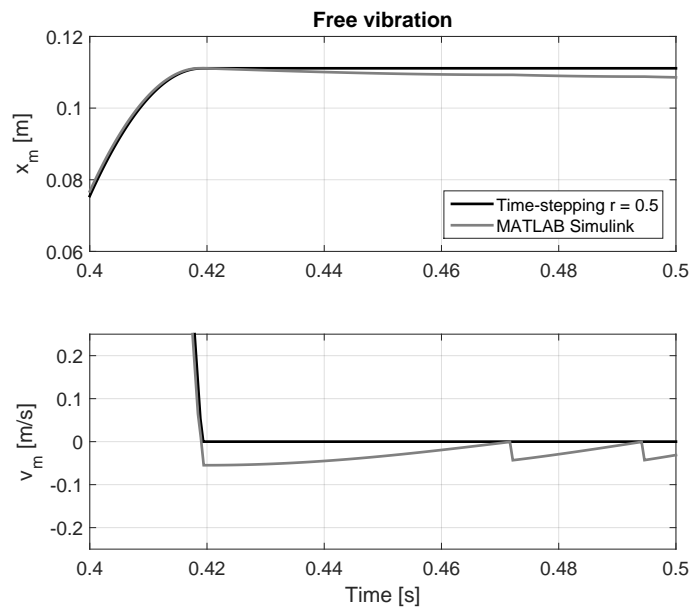


Figure A.2: Free vibration parallel Coulomb-spring system, time-stepping and Simulink, zoom.

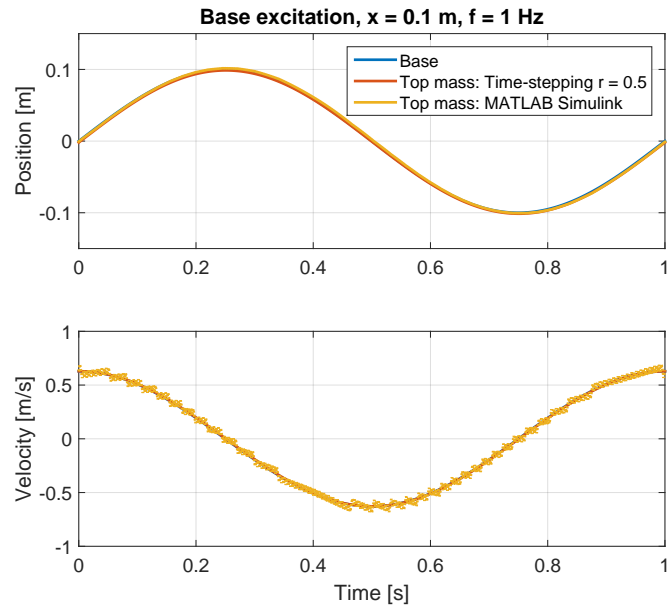


Figure A.3: Steady-state response parallel Coulomb-spring system, time-stepping and Simulink, stick.

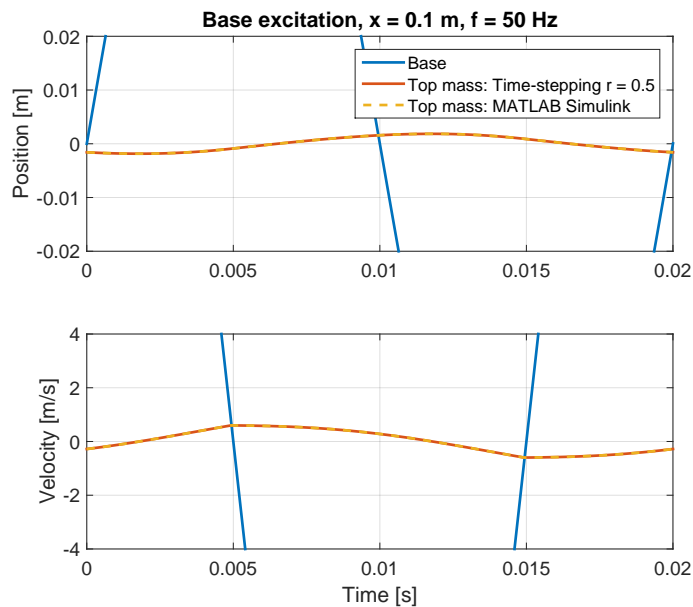


Figure A.4: Steady-state response parallel Coulomb-spring system, time-stepping and Simulink, slip.

A.2 System parameters

Table A.1: Wire rope system parameters.

Parameter	Symmetric system	Asymmetric system
m [kg]	8	8
$k_{wr,0}$ [N/m]	$3 \cdot 10^3$	
g_1 [N/m]		$3 \cdot 10^3$
g_2 [N/m ²]		$4 \cdot 10^4$
g_3 [N/m ³]		$3 \cdot 10^5$
$k_{wr,1}$ [N/m]	$3 \cdot 10^3$	$3 \cdot 10^3$
$k_{wr,2}$ [N/m]	$3 \cdot 10^3$	$3 \cdot 10^3$
$F_{c,1}$ [N]	8.3	8.3
$F_{c,2}$ [N]	14.6	14.6

A.3 Symmetric isolation system

The additional frequency-amplitude magnitude diagram, as mentioned in section 3.4.1, is shown in this appendix.

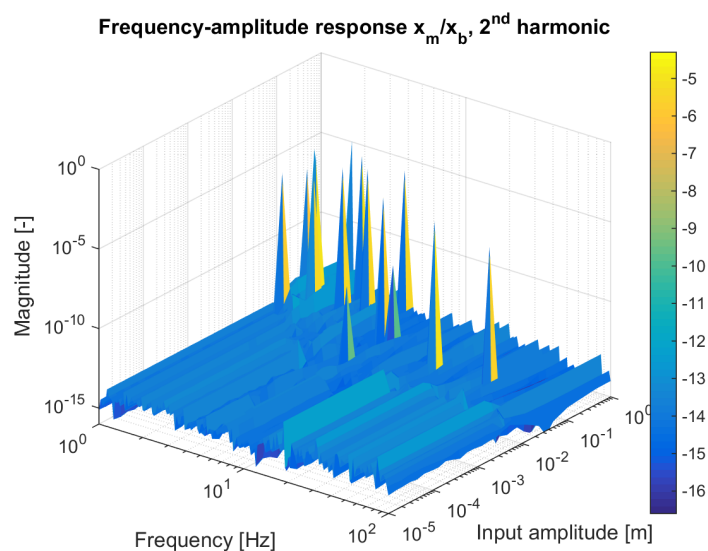


Figure A.5: Frequency-amplitude diagram, magnitude 2nd harmonic, symmetric.

A.4 Asymmetric isolation system

The additional time histories, as mentioned in 3.4.2, are shown in this appendix.

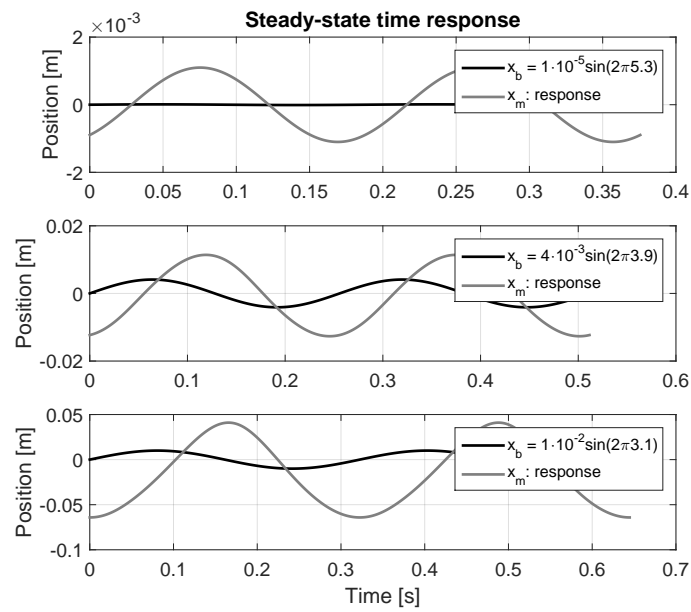


Figure A.6: Steady-state time histories top mass position for different inputs, asymmetric.

A.5 Analysis shock

The additional shock response figures, as discussed in section 3.4.3, are shown in this appendix.

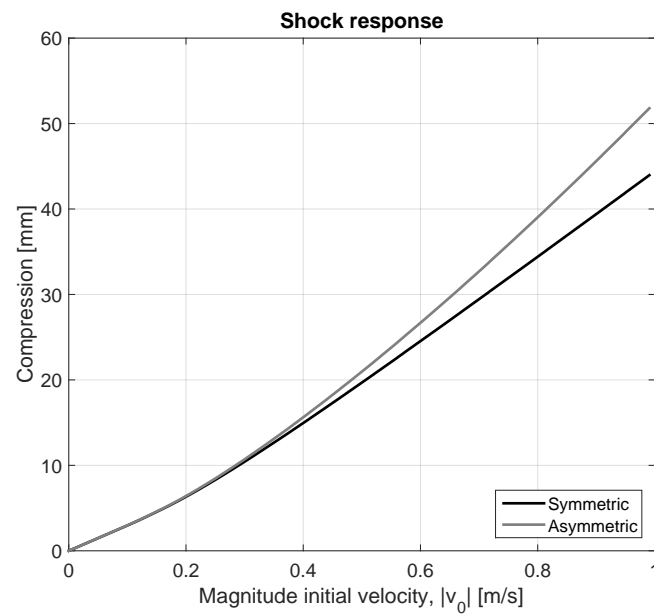


Figure A.7: Maximum deflection free fall as function of velocity.

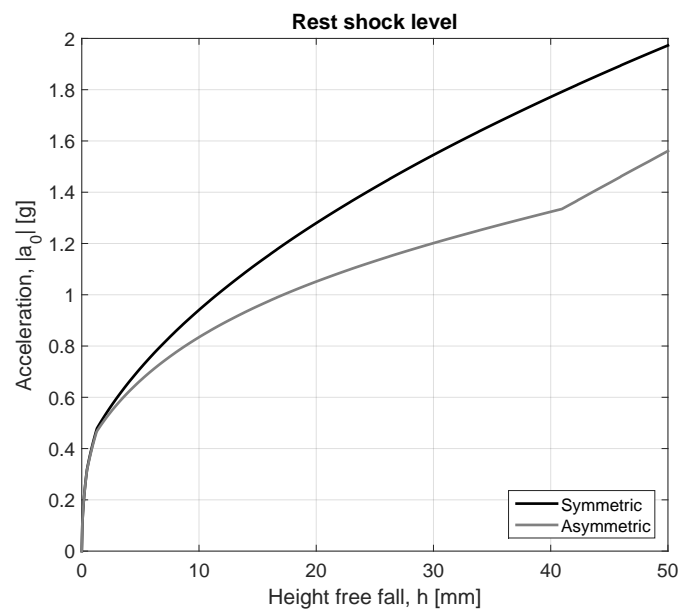


Figure A.8: Maximum absolute acceleration free fall as function of drop height.

Appendix B

Parameters elastomer analysis

In this appendix the elastomer system parameters (B.1) are listed.

B.1 System parameters

Table B.1: Elastomer system parameters.

Parameter	Low freq. damping	Medium freq. damping	High freq. damping
m [kg]	5	5	5
$k_{el,0}$ [N/m]	$1.0 \cdot 10^3$	$1.0 \cdot 10^3$	$1.0 \cdot 10^3$
$k_{el,1}$ [N/m]	$5.4 \cdot 10^2$	$5.4 \cdot 10^2$	$5.4 \cdot 10^2$
$k_{el,2}$ [N/m]	$1.2 \cdot 10^3$	$1.2 \cdot 10^3$	$1.2 \cdot 10^3$
$k_{el,3}$ [N/m]	$2.5 \cdot 10^3$	$2.5 \cdot 10^3$	$2.5 \cdot 10^3$
$k_{el,4}$ [N/m]	$5.4 \cdot 10^3$	$5.4 \cdot 10^3$	$5.4 \cdot 10^3$
$k_{el,5}$ [N/m]	$1.2 \cdot 10^4$	$1.2 \cdot 10^4$	$1.2 \cdot 10^4$
$k_{el,6}$ [N/m]	$2.5 \cdot 10^4$	$2.5 \cdot 10^4$	$2.5 \cdot 10^4$
$k_{el,7}$ [N/m]	$5.4 \cdot 10^4$	$5.4 \cdot 10^4$	$5.4 \cdot 10^4$
$k_{el,8}$ [N/m]	$1.2 \cdot 10^5$	$1.2 \cdot 10^5$	$1.2 \cdot 10^5$
$k_{el,9}$ [N/m]	$2.5 \cdot 10^5$	$2.5 \cdot 10^5$	$2.5 \cdot 10^5$
$k_{el,10}$ [N/m]	$5.4 \cdot 10^5$	$5.4 \cdot 10^5$	$5.4 \cdot 10^5$
$d_{el,1}$ [Ns/m]	$5.4 \cdot 10^4$	$5.4 \cdot 10^2$	$5.4 \cdot 10^0$
$d_{el,2}$ [Ns/m]	$2.5 \cdot 10^4$	$2.5 \cdot 10^2$	$2.5 \cdot 10^0$
$d_{el,3}$ [Ns/m]	$1.2 \cdot 10^4$	$1.2 \cdot 10^2$	$1.2 \cdot 10^0$
$d_{el,4}$ [Ns/m]	$5.4 \cdot 10^3$	$5.4 \cdot 10^1$	$5.4 \cdot 10^{-1}$
$d_{el,5}$ [Ns/m]	$2.5 \cdot 10^3$	$2.5 \cdot 10^1$	$2.5 \cdot 10^{-1}$
$d_{el,6}$ [Ns/m]	$1.2 \cdot 10^3$	$1.2 \cdot 10^1$	$1.2 \cdot 10^{-1}$
$d_{el,7}$ [Ns/m]	$5.4 \cdot 10^2$	$5.4 \cdot 10^0$	$5.4 \cdot 10^{-2}$
$d_{el,8}$ [Ns/m]	$2.5 \cdot 10^2$	$2.5 \cdot 10^0$	$2.5 \cdot 10^{-2}$
$d_{el,9}$ [Ns/m]	$1.2 \cdot 10^2$	$1.2 \cdot 10^0$	$1.2 \cdot 10^{-2}$
$d_{el,10}$ [Ns/m]	$5.4 \cdot 10^1$	$5.4 \cdot 10^{-1}$	$5.2 \cdot 10^{-3}$

Appendix C

Additional simulation results hybrid analysis

In this appendix, additional frequency-amplitude diagrams of the symmetric hybrid isolation system (C.1), and additional time histories of the asymmetric hybrid isolation system (C.2) are shown.

C.1 Symmetric isolation system

The additional frequency-amplitude magnitude diagram of the second harmonic, as mentioned in section 5.3.1, is shown in this appendix.

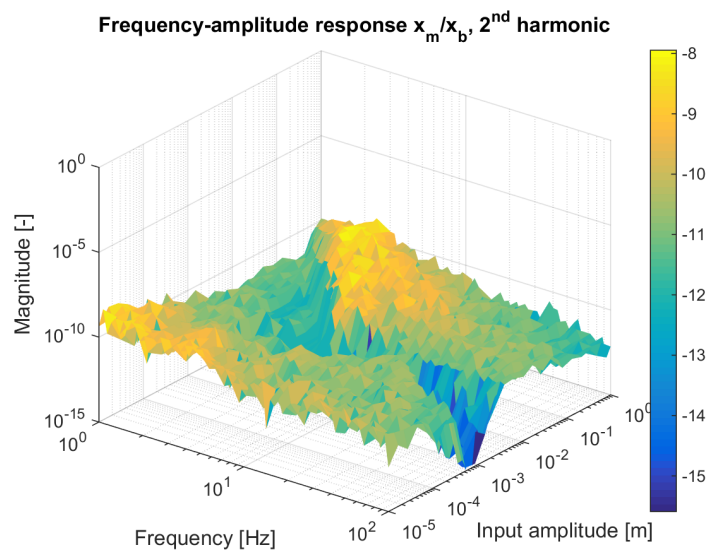


Figure C.1: Frequency-amplitude diagram, magnitude 2nd harmonic, symmetric.

C.2 Asymmetric isolation system

The additional time histories, as mentioned in 5.3.2, are shown in this appendix.

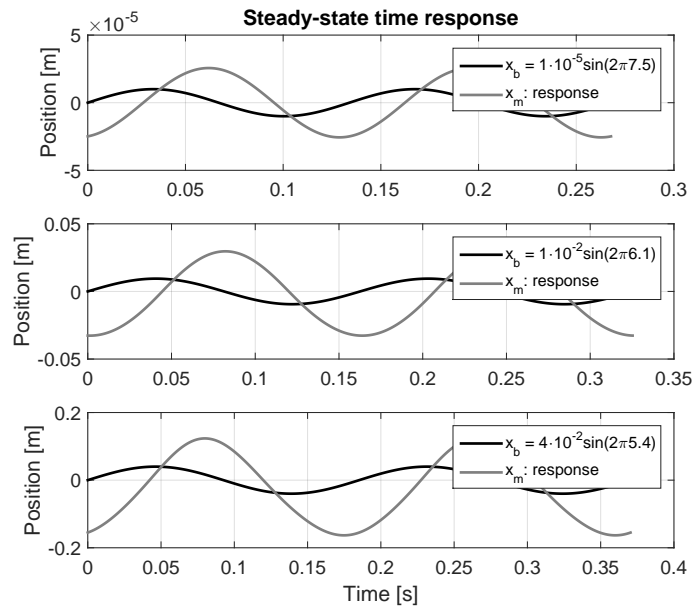


Figure C.2: Steady-state time histories top mass position for different inputs, asymmetric.

Appendix D

Measurement setups

In this appendix, a detailed description of the measurement setups is given (D.1). Further, the technical drawings of the drop test setup (D.2) and the product sheets of the isolators (D.3) are included.

D.1 Measurements hardware

This section provides a more detailed description and images of the measurement setups.

D.1.1 Quasi-static setup

The quasi-static measurements are performed on a lathe. A load cell (Mecmesin S-Beam 500/330N) is used to measure the force and a displacement sensor (Tesa GT 62 USB) measures the deflection. A notebook with LabView software is used for the data acquisition. Figure D.1 shows an overview of the whole setup. At the left there is the data acquisition system, top right the isolation component and sensors are shown. A detailed overview of the isolator and sensors is given in figure D.2. The load cell is in series with the isolator, the displacement sensor is placed in parallel with the isolator, rigidly connected to the lathe by a magnetic base.

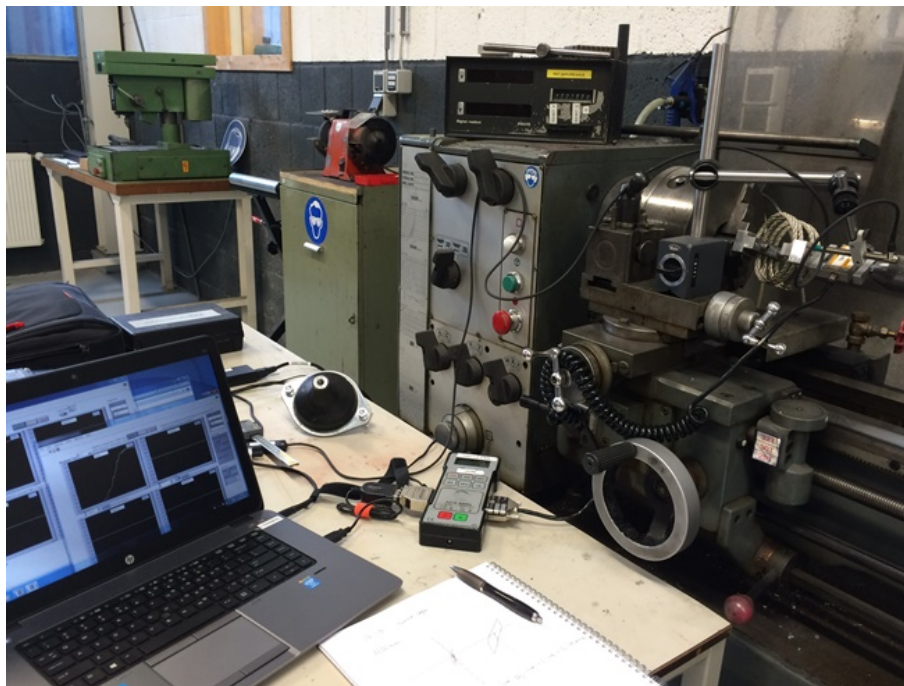


Figure D.1: Overview quasi-static setup.



Figure D.2: Detailed overview isolator and sensors quasi-static setup, detailed.

D.1.2 Dynamical shaker setup

An existing shaker setup at the DCT-lab of TU/e is used to analyse the vibrational behaviour of the isolation systems. The setup is designed for SDOF floor excited systems, the top mass is restricted to a single translational movement in vertical direction. Interface plates are made to fit the isolators and weights to the shaker head and top mass. Figure D.3 shows an overview of the whole dynamical shaker setup. Figure D.4 provides a more detailed overview of the shaker head, isolator, and top mass.

The shaker is fixed to the ground through the base frame. The isolator is mounted on top of the shaker head. A linear guidance of leaf springs ensures the shaker head can only move in vertical direction. The top mass is restricted to vertical motion by air bearings on the metrology frame. The metrology frame is isolated from ground vibrations by air pots. Therefore, the two vibrometers are mounted on the metrology frame. The top mass and isolator mass values are shown in table D.1.

Table D.1: Mass values.

Isolator	Top mass [kg]	Isolator mass [kg]
Wire rope	2.98	0.21
Elastomer	0.99 (harmonic input)	0.53
	0.99 - 6.40 (random input)	0.53
Hybrid	0.99	0.88

The system is excited by a voltage controlled electromechanical shaker system. A SigLab data acquisition system with notebook is used to perform the measurements. The acquisition system measures the control voltage, the position and the velocity of the base (Polytec OFV-5000 controller with OFV-552 sensor head), and the velocity of the top mass (Polytec OFV-3000 controller with OFV-302 sensor head). The control voltage is measured directly.

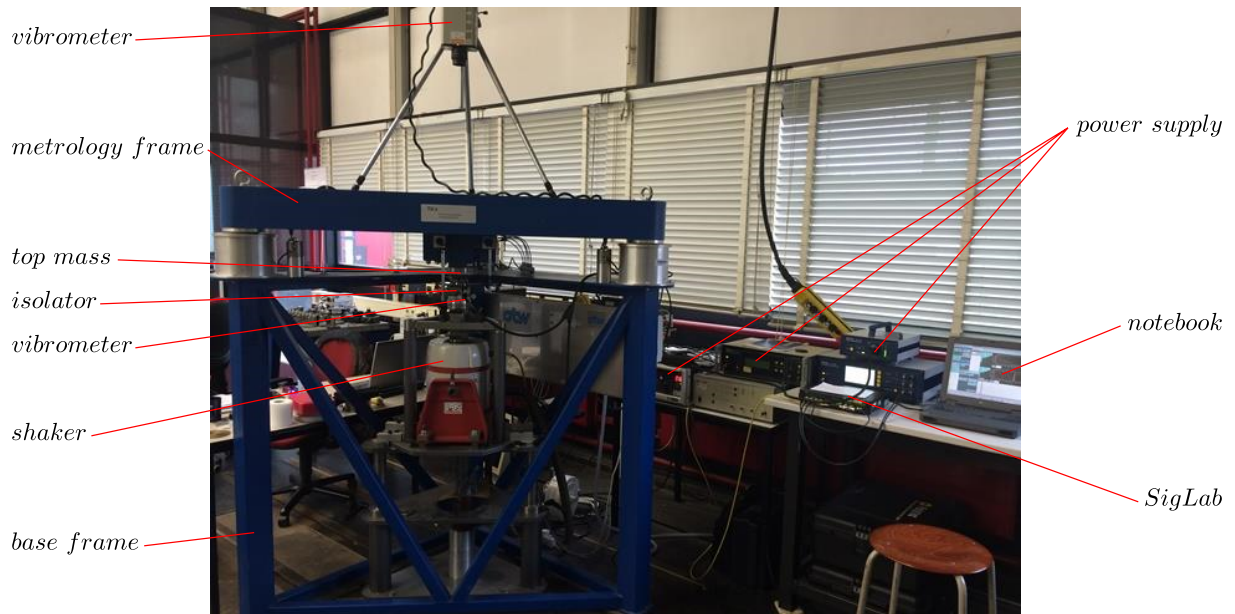


Figure D.3: Overview dynamical shaker setup.

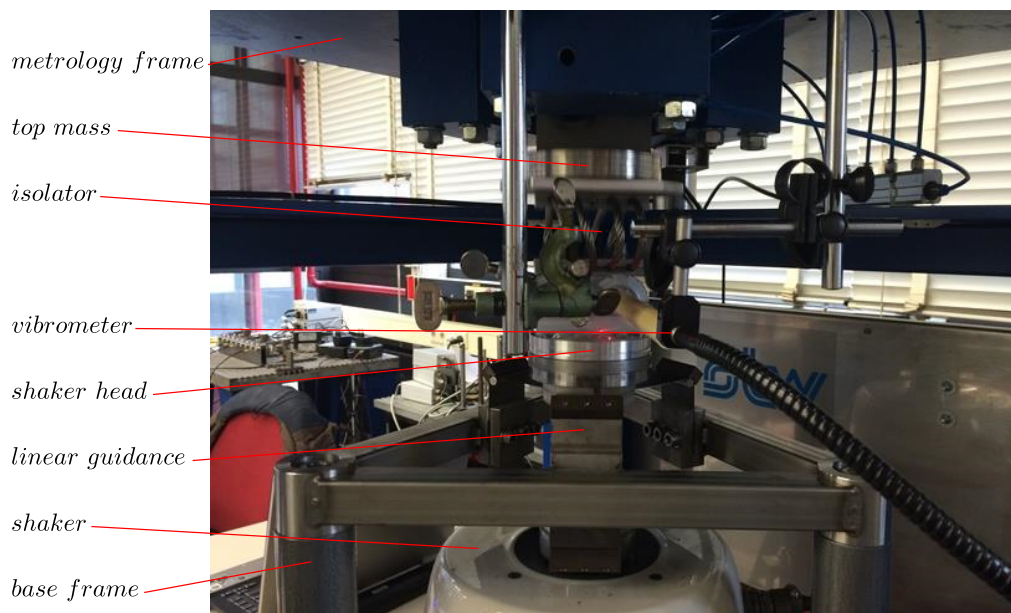


Figure D.4: Overview dynamical shaker setup, detailed.

Note that to use the HOSIDF’s method, a pure sinusoidal (i.e. harmonic) movement of the shaker head is required. However, the shaker motion is indirectly controlled by a harmonic voltage, U_{in} , and not directly by a harmonic motion. In previous measurements with this setup, a linear model of the bare shaker system (v_b/U_{in}) was derived, identified, and incorporated in the simulation model [23, 40, 41, 46, 55]. However, measurements of the bare shaker, excited by harmonic control voltages, indicate non-linear behaviour, which is highly undesired for determining the HOSIDF’s. The magnitude of the higher harmonic components is significant, especially for excitation frequencies up to 30 Hz .

A possible method to remove the bias due to higher order components, is compensating for the higher order harmonics. This method requires several measurements sessions with constant excitation amplitude and a controller is needed to do this accurately [53]. Another solution is using a repetitive controller, which controls the voltage to achieve a harmonic base motion [50]. Both methods are too complex considering the scope of this thesis. This means that the higher order harmonic responses analysed in this chapter, only give an indication of the non-linear characteristics.

Next to the (undesired) higher harmonics in the excitation signal, the dynamics of the bare shaker system result in a frequency dependent base motion to control voltage relation (i.e. v_b/U_{in}). Therefore, the control voltage is manually controlled to approximate a frequency independent harmonic base motion spectrum. Note that a dedicated controller can probably fully compensate for these effects. Due to force limitations it is not possible to achieve a reasonable base position spectrum, therefore a base velocity spectrum is approximated.

D.1.3 Drop test setup

An overview of the drop test setup with data acquisition hardware, is shown in D.5, moreover figure D.6 shows a detailed view of the drop test components. A Brüel & Kjaer Pulse data acquisition system with frontend and notebook is used to acquire the data. The laser vibrometer (Polytec OFV-5000 controller with OFV-552 sensor head) measures the relative velocity and displacement between the top and bottom mass, i.e. the velocity over the isolator and isolator deflection. Two three axes accelerometers (Brüel & Kjaer 4506-B) are positioned on top of the top mass, the vertical acceleration of the top mass is determined by the mean of both sensor signals. A high speed camera (Apple iPhone 6) is used to capture the behaviour visually. The top and bottom mass are represented by one or two solid steel blocks together with the bearing connecting plate, leaf springs and bearings. The release mechanism is located below the isolation system. This way the isolator is statically loaded by the top mass at the moment of release. The shaft with hole pattern is used to set the drop height, the drop height resolution is 10 mm . The release is done by pulling the small pin out of the shaft. Table D.2 presents the masses and drop height range of the experiments.

Table D.2: Mass and drop height values.

Isolator	Isolator mass [kg]	Bottom mass [kg]	Top mass [kg]	Drop height [cm]
Wire rope	0.21	7.88	4.25	1 - 14
			7.31	1 - 8
Elastomer	0.53	7.83	4.37	1 - 14
			7.42	1 - 8
Hybrid	0.88	7.83	4.25	1 - 14
			7.31	1 - 6

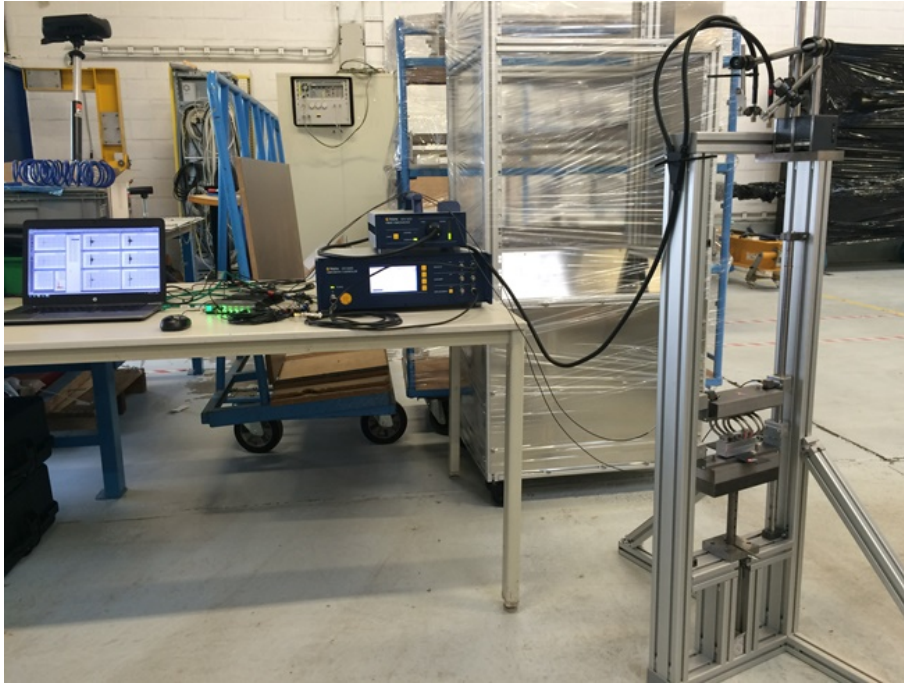


Figure D.5: Overview drop test setup.

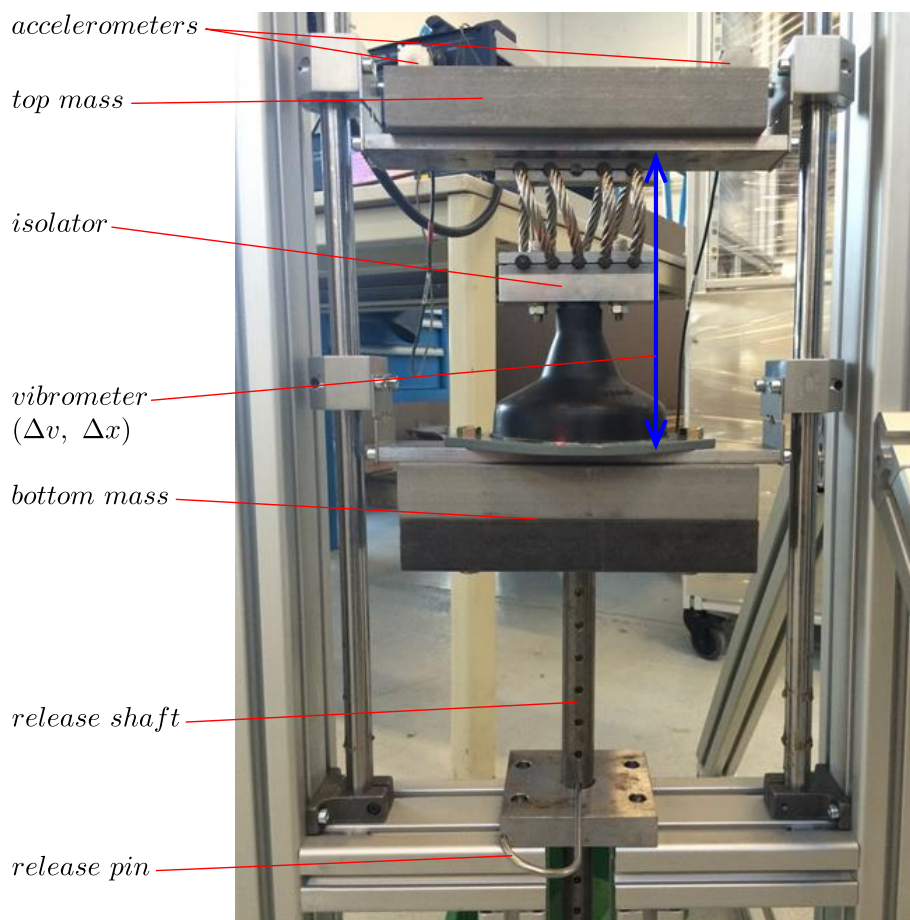
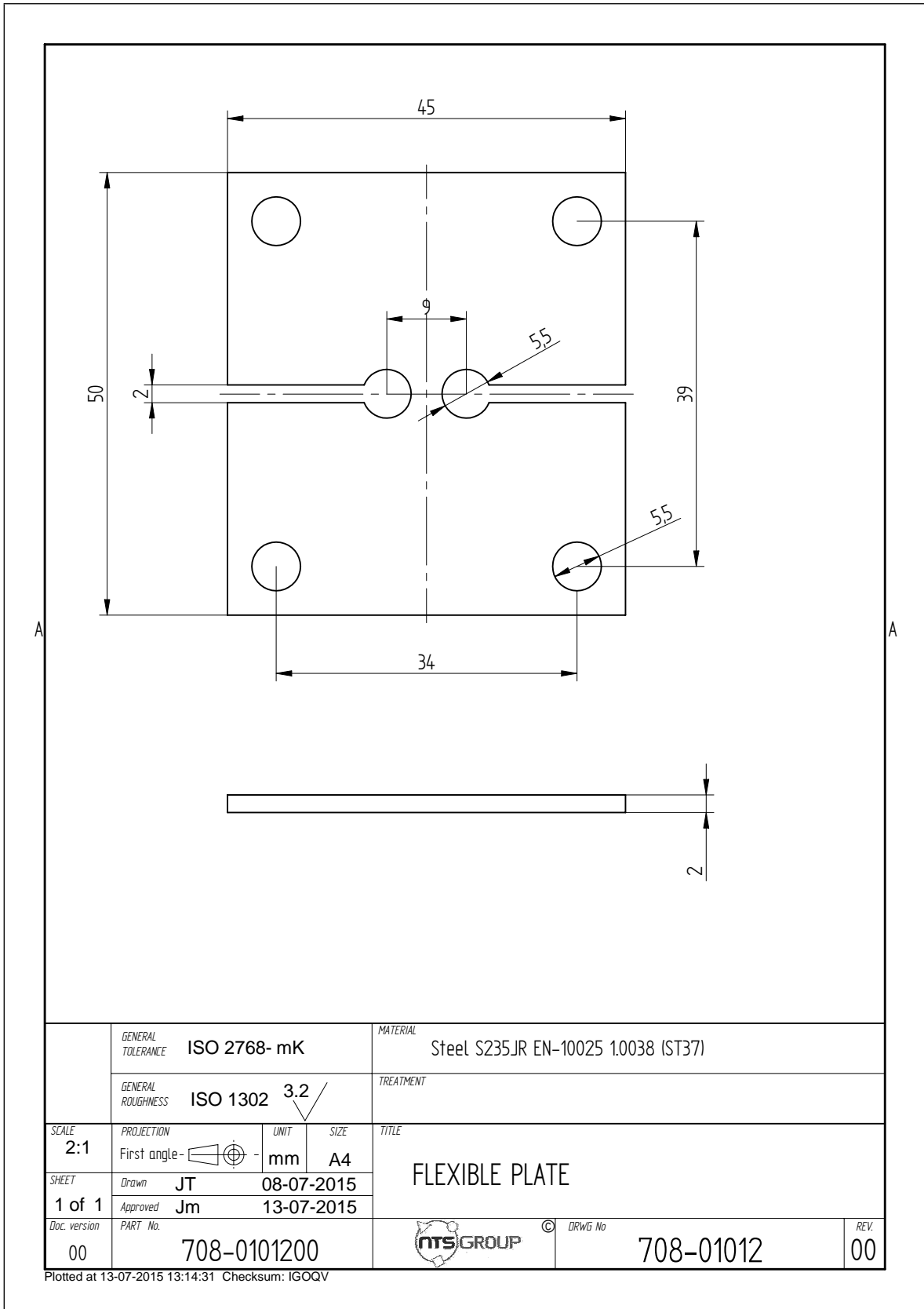
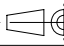

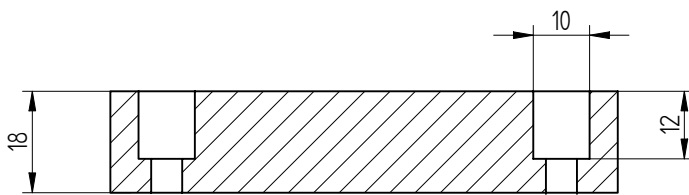
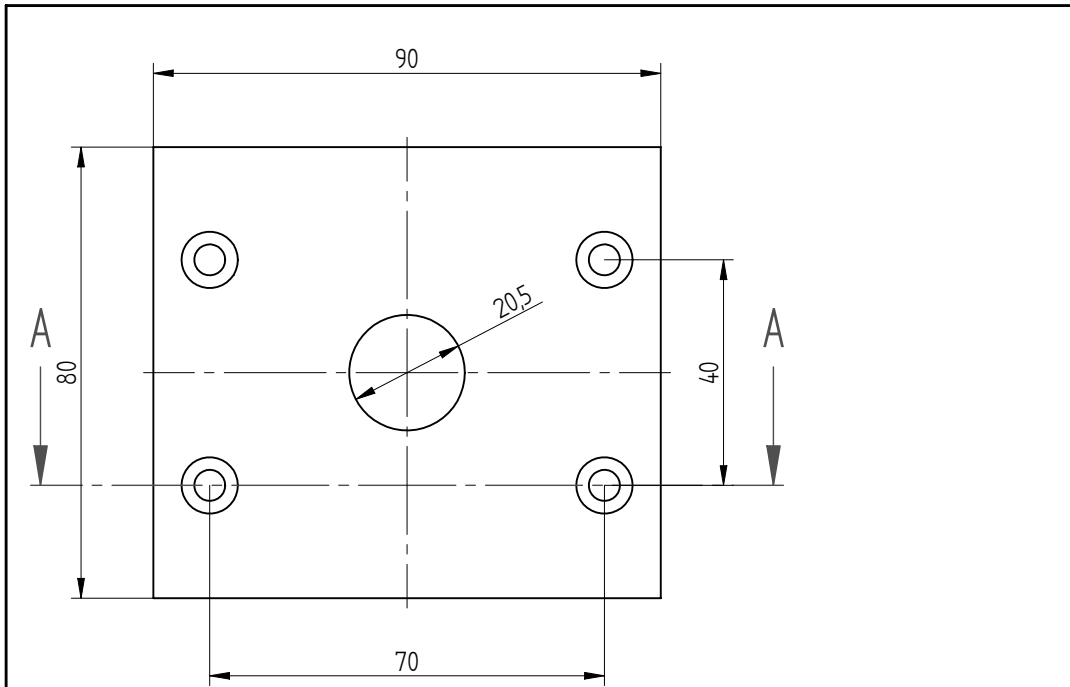


Figure D.6: Overview drop test setup, detailed.

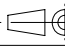



GENERAL TOLERANCE		ISO 2768- mK		MATERIAL		Steel S235JR EN-10025 1.0038 (ST37)			
GENERAL ROUGHNESS		ISO 1302 3.2		TREATMENT					
SCALE	PROJECTION	UNIT	SIZE	TITLE					
2:1	First angle - 	mm	A4	FLEXIBLE PLATE					
SHEET	Drawn	JT	08-07-2015						
1 of 1	Approved	Jm	13-07-2015						
Doc. version	PART No.	708-0101200		 © DRWG No		708-01012 <table border="1" style="float: right;"> <tr> <td>REV.</td> <td>00</td> </tr> </table>		REV.	00
REV.	00								

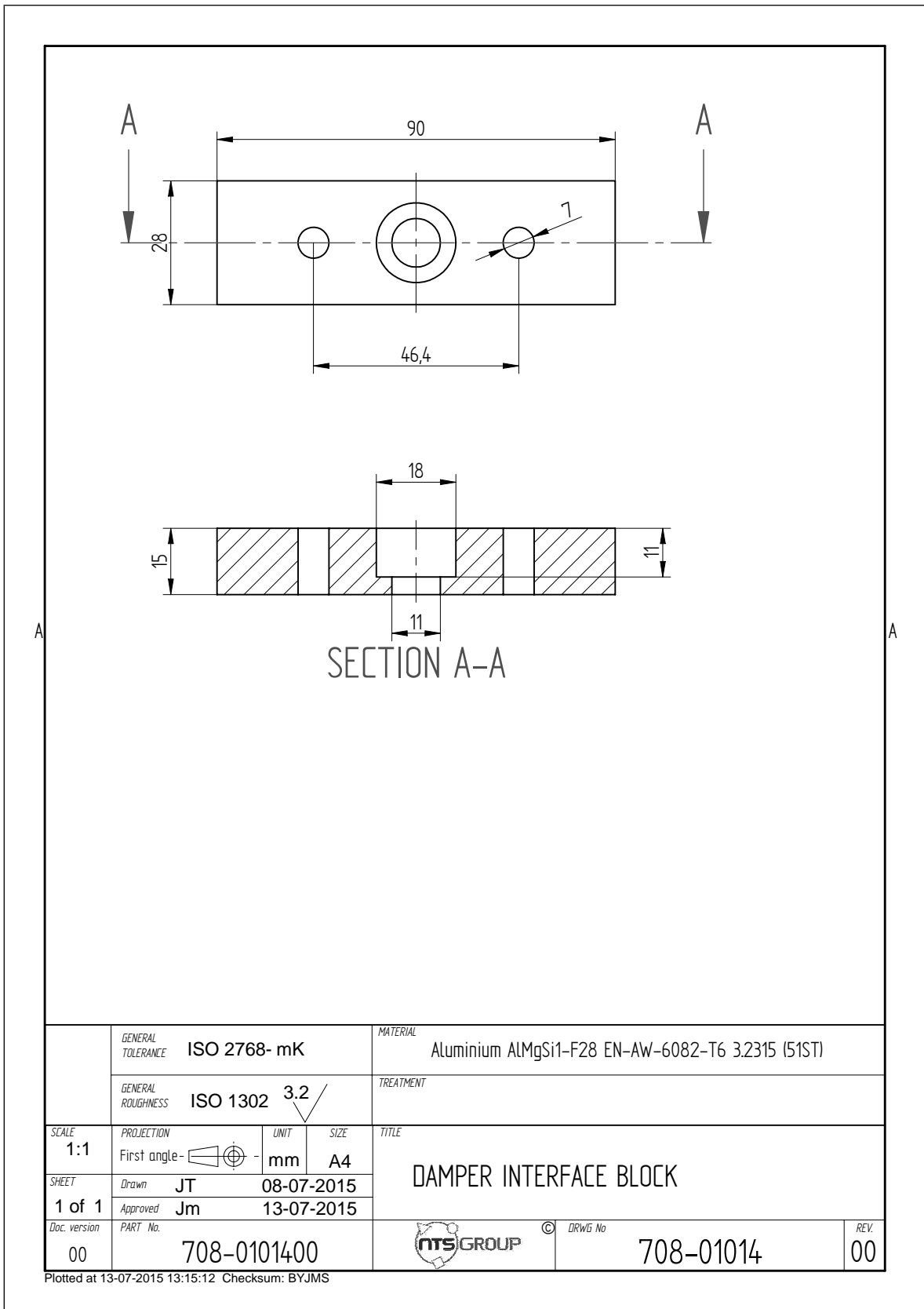
Plotted at 13-07-2015 13:14:31 Checksum: IGOQV

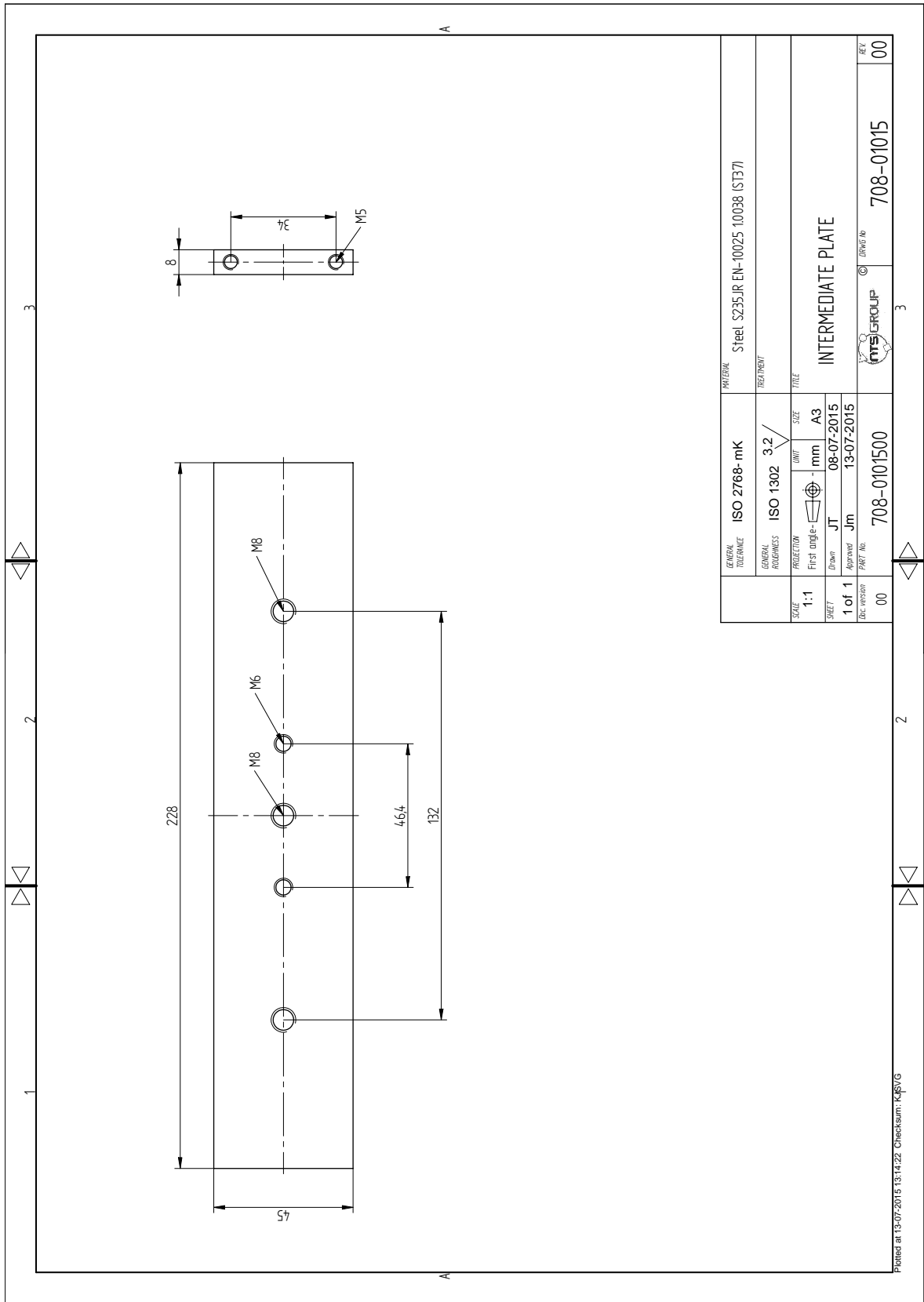


SECTION A-A

GENERAL TOLERANCE		ISO 2768- mK		MATERIAL		Steel S235JR EN-10025 1.0038 (ST37)	
GENERAL ROUGHNESS		ISO 1302 3.2		TREATMENT			
SCALE	PROJECTION	UNIT	SIZE	TITLE			
1:1	First angle - 	mm	A4	GROUND PLATE			
SHEET	Drawn	30-06-2015					
1 of 1	Approved	Jm	13-07-2015				
Doc. version	PART No.	708-0101300		 © DRWG No		708-01013	
00						REV. 00	

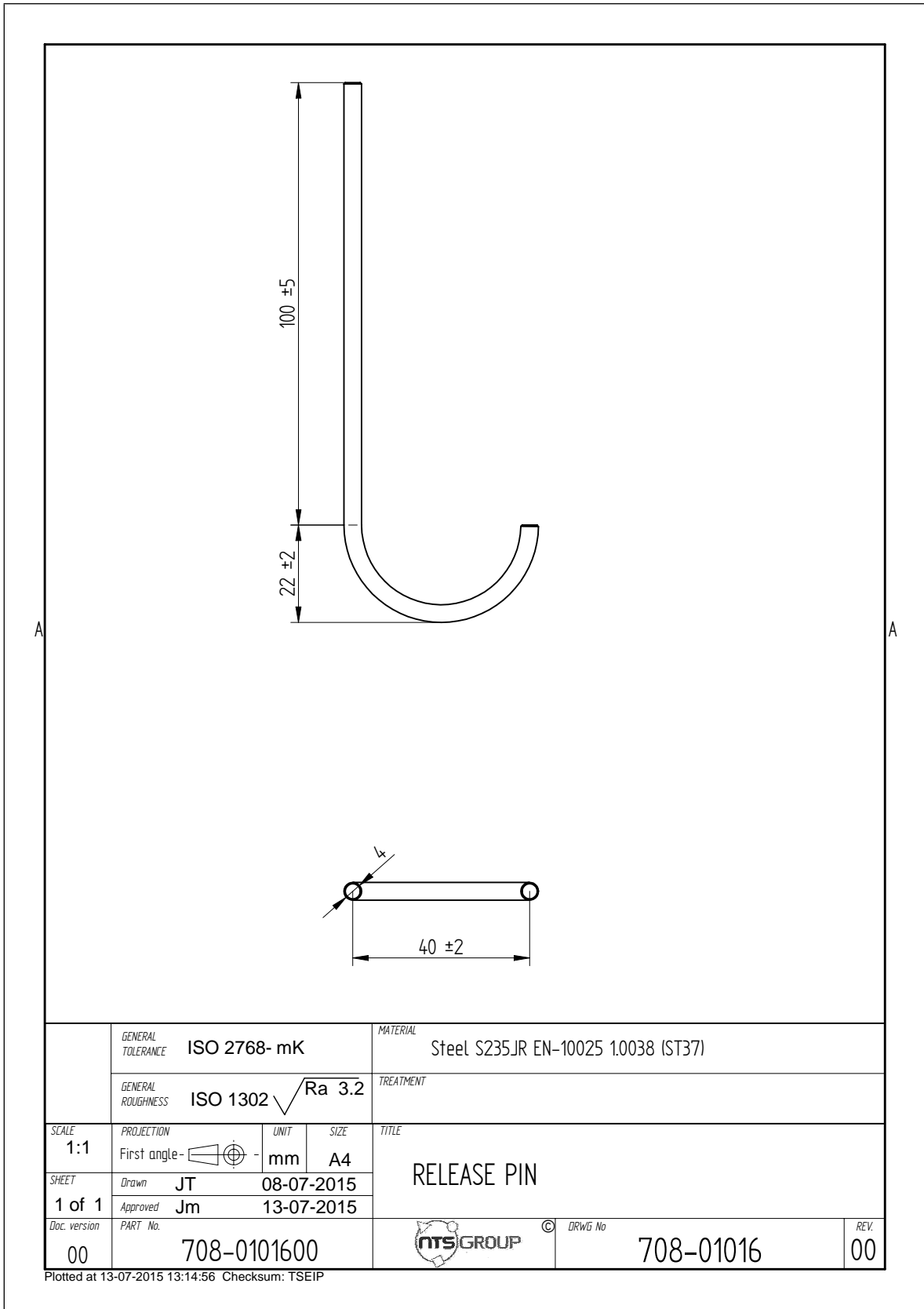
Plotted at 13-07-2015 13:14:47 Checksum: RPXDJ

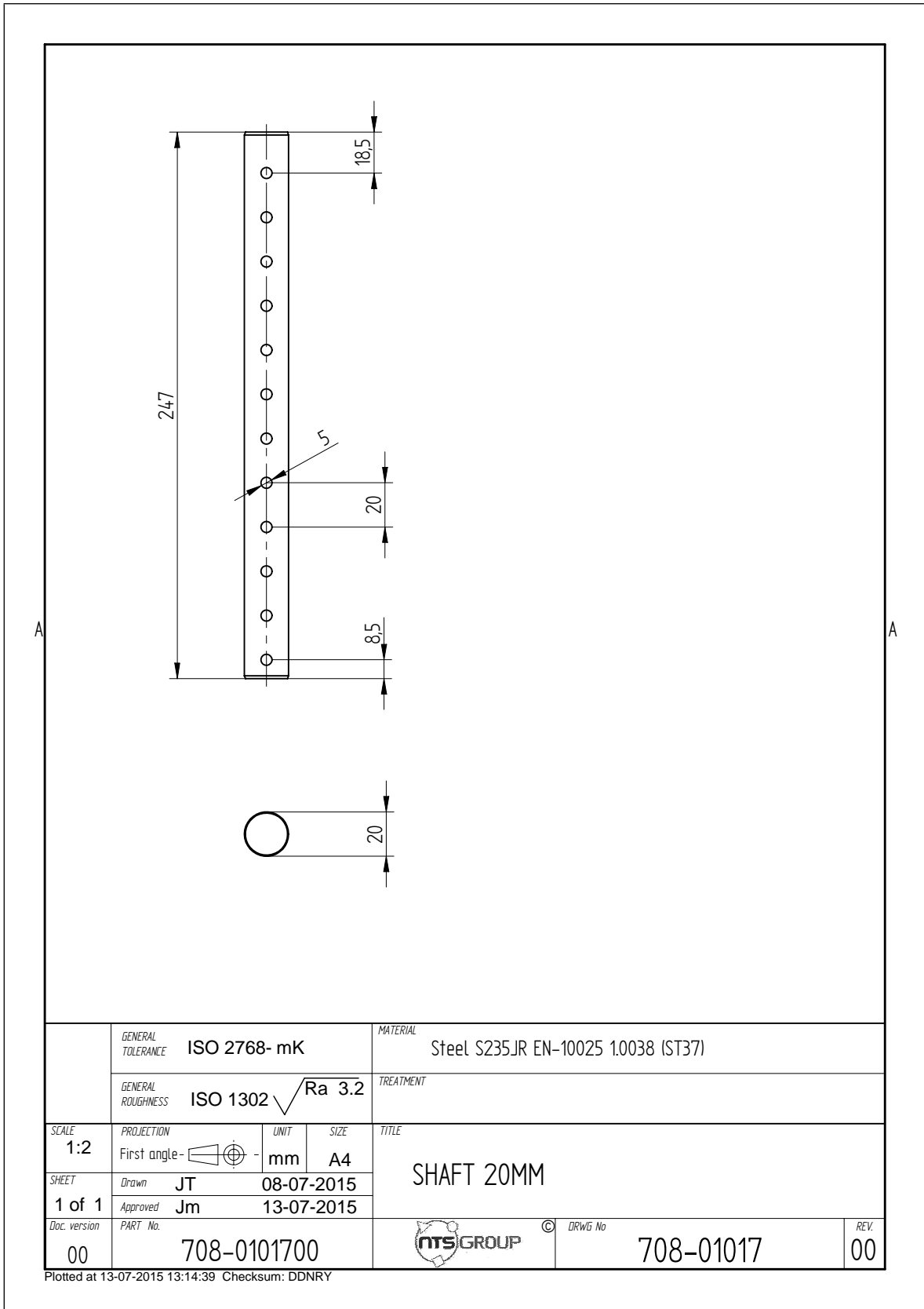


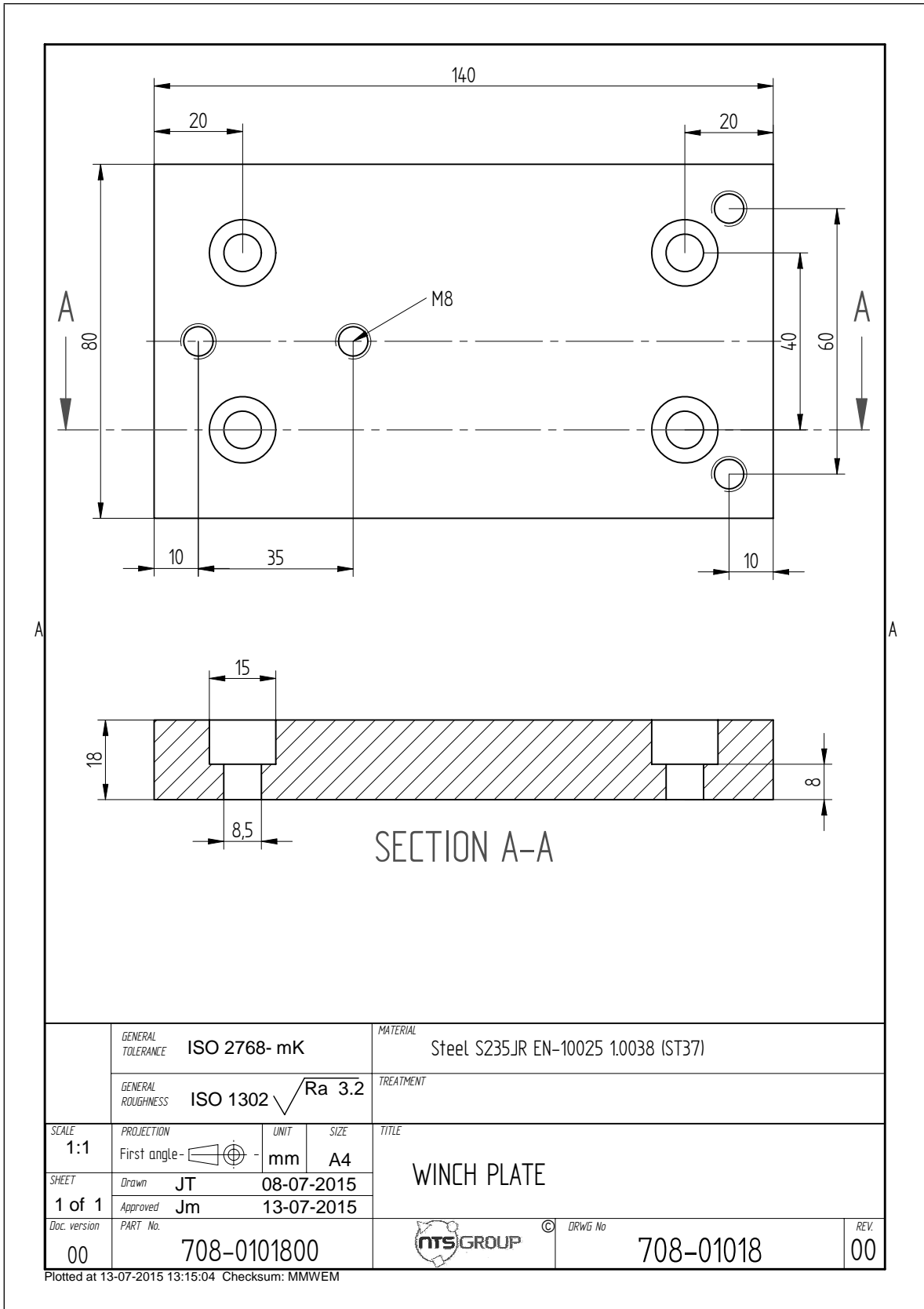


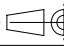

GENERAL TOLERANCE	ISO 2768-mK	MATERIAL	Steel S235JR EN-10025 1.0038 (S137)
GENERAL DIMENSIONS	ISO 1302	TREATMENT	
PROJECTION	First angle	FILE	
SCALE	1:1	UNIT	mm
SHEET	1 of 1	SIZE	A3
DEC. VERSION	00	Drawn	JT
		Approved	Jm
		DATE	13-07-2015
		PART No.	708-0101500
		GROUP	708-01015
		REV	00

Printed at 13-07-2015 13:14:22 Checksum: K4S1/G







GENERAL TOLERANCE		ISO 2768- mK		MATERIAL		Steel S235JR EN-10025 1.0038 (ST37)			
GENERAL ROUGHNESS		ISO 1302 \sqrt{Ra} 3.2		TREATMENT					
SCALE	PROJECTION	UNIT	SIZE	TITLE					
1:1	First angle - 	mm	A4	WINCH PLATE					
SHEET	Drawn	JT	08-07-2015						
1 of 1	Approved	Jm	13-07-2015						
Doc. version	PART No.	708-0101800		 © DRWG No		708-01018 <table border="1" style="float: right;"> <tr> <td>REV.</td> <td>00</td> </tr> </table>		REV.	00
REV.	00								

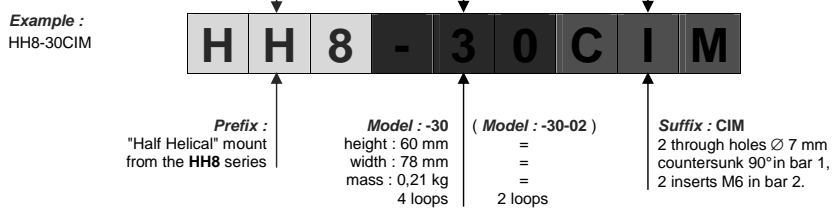
Plotted at 13-07-2015 13:15:04 Checksum: MMWEM

D.3 Product sheets isolators

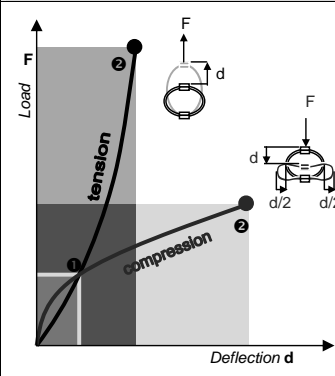
low frequency elastomer mounts		<i>series</i>																							
standard line "BF"		BFL																							
<i>definition</i>																									
<p style="text-align: center;"><i>Dimensions are in mm.</i></p>		<ul style="list-style-type: none"> • Multidirectional anti-vibration/ shock mounts. • Displacement under shock up to 45mm. • Transmissibility : $Q < 10$. • Maximum static load 3g. • Resonant frequency between 10 and 12Hz. • Temperature range : -30°C +100°C. • Great adaptability/versatility : Specials on request (materials, size and interfaces, etc.). <div style="text-align: right;"> </div>																							
<table border="1" style="width: 100%; border-collapse: collapse;"> <tr> <th style="text-align: left;">Series</th> </tr> <tr> <td>Materials and finishes</td> </tr> <tr> <td>BFL</td> </tr> <tr> <td>Elastomer : polychloroprene</td> </tr> <tr> <td>Top and bottom interfaces : corrosion protected steel</td> </tr> <tr> <td> <i>Other materials on request.</i></td> </tr> </table>	Series	Materials and finishes	BFL	Elastomer : polychloroprene	Top and bottom interfaces : corrosion protected steel	 <i>Other materials on request.</i>	<table border="1" style="width: 100%; border-collapse: collapse;"> <tr> <th rowspan="2" style="text-align: left;">Load capability</th> <th colspan="2" style="text-align: center;">static load (daN)</th> <th style="text-align: center;">axial stiffness</th> <th rowspan="2" style="text-align: center;">mass (kg)</th> </tr> <tr> <th style="text-align: center;">mini</th> <th style="text-align: center;">maxi</th> <th style="text-align: center;">(N.mm⁻¹)</th> </tr> <tr> <td style="text-align: center;">2</td> <td style="text-align: center;">4</td> <td style="text-align: center;">6</td> <td style="text-align: center;">12</td> <td rowspan="2" style="text-align: center;">0,5</td> </tr> <tr> <td style="text-align: center;">3</td> <td style="text-align: center;">8</td> <td style="text-align: center;">12</td> <td style="text-align: center;">24</td> </tr> </table>		Load capability	static load (daN)		axial stiffness	mass (kg)	mini	maxi	(N.mm ⁻¹)	2	4	6	12	0,5	3	8	12	24
Series																									
Materials and finishes																									
BFL																									
Elastomer : polychloroprene																									
Top and bottom interfaces : corrosion protected steel																									
 <i>Other materials on request.</i>																									
Load capability	static load (daN)		axial stiffness	mass (kg)																					
	mini	maxi	(N.mm ⁻¹)																						
2	4	6	12	0,5																					
3	8	12	24																						
<p><i>Example :</i> BFL-12</p> <div style="display: flex; justify-content: center; align-items: center; gap: 10px;"> <div style="border: 1px solid black; padding: 5px; text-align: center;">B</div> <div style="border: 1px solid black; padding: 5px; text-align: center;">F</div> <div style="border: 1px solid black; padding: 5px; text-align: center;">L</div> <div style="border: 1px solid black; padding: 5px; text-align: center;">-</div> <div style="border: 1px solid black; padding: 5px; text-align: center;">1</div> <div style="border: 1px solid black; padding: 5px; text-align: center;">2</div> </div> <p style="text-align: center;"><i>Prefix :</i> "Low Frequency" mount from the BFL series</p> <div style="display: flex; justify-content: space-between; margin-top: 10px;"> <div style="text-align: center;"> <p>min static load : 4 daN max static load : 6 daN axial average stiffness : 12 N.mm⁻¹</p> </div> </div>																									
01/07/2013																									
Socitec BP 33, 78501 Sartrouville cedex - France Telephone : +33 (0)1 61 04 60 00 Fax : +33 (0)1 39 14 03 27 http://www.socitec.com e-mail : shock-intl@socitec.com																									
Document subject to modification without prior notice																									

wire rope isolators	<i>series</i>
standard line "Half-Helical"	HH8
<i>definition</i>	
<p style="font-size: small;">Dimensions are in mm.</p> <p style="font-size: small;">Dimensions for reference only.</p>	<ul style="list-style-type: none"> • All metal multidirectional anti-vibration/shock mounts. • Exceptional reliability and long life. • High damping. • No ageing. • Corrosion resistant. • Unequalled temperature range : -180°C +300°C. • Great adaptability/versatility. Specials on request (material size and number of loops, etc.).

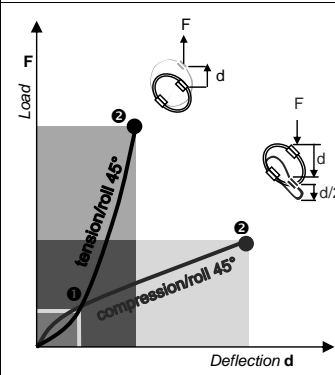
Series	Model	Interfaces	Bar 1		
Materials and finishes HH8 Cable : stainless steel. (galvanised HHG8) Retainer bars : Aluminium alloy/Surtec 650 Screws : alloy steel/zinc plate. (Inserts : stainless steel). <i>All stainless steel version HHSS8</i> <i>Other materials on request.</i>	height H (mm)	width W (mm)	mass (kg)		
	-10	45	54	0,17	
	-20	51	61	0,18	
	-25	56	69	0,20	
	-30	60	78	0,21	
	-35	60	87	0,22	
	-38	64	93	0,23	
-40	64	98	0,24		
-50	79	106	0,25		
-60	95	127	0,28		
		fixture holes D	Bar 1		
		Bar 2	2 through holes Ø 7 mm	2 through holes Ø 7 mm countersunk 90°	2 inserts M6
			2 through holes Ø 7 mm	not standard	not standard
		2 through holes Ø 7 mm countersunk 90°	TCM	CM2	not standard
		2 inserts M6	TIM	CIM	IM2



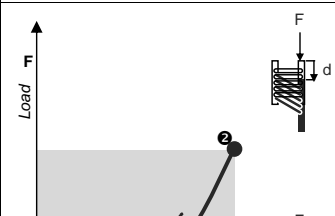
series wire rope isolators
HH8 standard line "Half-Helical"
*performances**



HH8 series		Model	-10	-20	-25	-30	-35	-38	-40	-50	-60
Max static	F daN		35,8	29,6	23,9	19,2	16,0	13,7	12,9	11,9	7,1
	d mm		3,3	4,2	5,2	5,9	5,8	6,5	6,5	9,0	11,6
Max shock	F daN		108	88,8	71,7	57,5	47,8	41,2	38,5	35,6	21,3
	d mm		18	23	28	32	32	35	36	49	63
Max vibration	2a mm		2,0	2,5	3,1	3,5	3,5	3,9	3,9	5,4	6,9
	f Hz		9,2	8,1	7,4	7,0	7,2	6,9	6,9	5,7	5,0



HH8 series		Model	-10	-20	-25	-30	-35	-38	-40	-50	-60
Max static	F daN		26,9	22,2	17,9	14,4	12,0	10,3	9,7	8,9	5,3
	d mm		5,3	6,9	8,6	9,9	8,2	10,9	9,2	15,8	16,4
Max shock	F daN		67,0	54,9	44,7	36,3	31,0	26,8	25,3	22,5	13,4
	d mm		27	35	42	48	48	53	53	74	94
Max vibration	2a mm		3,0	3,8	4,6	5,3	5,2	5,8	5,8	8,1	10,4
	f Hz		7,7	6,8	6,2	5,9	6,1	5,8	5,9	4,8	4,2



HH8 series		Model	-10	-20	-25	-30	-35	-38	-40	-50	-60
Max static	F daN		17,9	14,8	12,0	9,6	8,0	6,9	6,4	5,9	3,6
	d mm		6,3	8,0	9,8	11,2	11,0	12,2	12,3	17,1	22
Max shock	F daN		124	93,4	76,6	64,0	62,7	55,2	53,9	39,2	19,8
	d mm		20	25	31	38	45	51	54	60	69
Max vibration	2a mm		2,2	2,7	3,4	4,2	4,9	5,6	6,0	6,5	7,6
	f Hz		9,1	8,1	7,3	6,6	6,3	5,9	5,8	5,3	4,8

① Max static load (F) with corresponding deflection (d)
 ② Max shock load (F) with corresponding deflection (d)
 ③ Uncoupled resonant frequency (f) under max static loading ① and max peak to peak sinusoidal vibration input (2a)
 * Important : Performance characteristics are given here for reference only. They can be increased under specific conditions.
 Contact us. 01/07/2013

Typical shock/vibration specifications :

Ground Forces	GAM EG13A, SEFT 001, MIL-STD-810, VG 95332.
Air	AIR 7306, MIL-E-5400, MIL-C-172, MIL-STD-810.
Marine	GAM EG13C, IT25-21/96-31/15-86, MIL-S-167, MIL-S-901, STANAG 042, BV 043.73, BV 044.
Others	GAM EMB1, GAM EMBT4, DEF STAN 07-55, IEC 571, FINABEL 2C.

Socitec
 BP 33, 78501 Sartrouville cedex - France
 Telephone : +33 (0)1 61 04 60 00
 Fax : +33 (0)1 39 14 03 27
 http://www.socitec.com
 e-mail : shock-intl@socitec.com
 Document subject to modification without prior notice



Appendix E

Additional measurement results

In this appendix, additional measurement results of the wire rope isolator (E.1), elastomer isolator (E.2), and hybrid isolator (E.3) experiments are provided. In the first part of each section, the (harmonic) input signal of the harmonic shaker tests is analysed. The second part shows several images, captured during the drop test measurements at specific time instances.

E.1 Measurements wire rope isolator

In this section, the analysis of the velocity signal of the shaker table in the shaker experiment (E.1.1) and time frames of the drop tests (E.1.2) for the wire rope analysis (section 6.2) are presented.

E.1.1 Shaker experiment

Figure E.1 shows the first three harmonics of the velocity signal of the shaker table. It is clear that a frequency independent velocity amplitude is not realized. The dominant first harmonic component is shown in figure E.2. Considering the voltage as the input signal, we have a fourth order mechanical system with the the shaker base mass and the system top mass. Near 15 Hz , the shaker resonance is visible, whereas near 90 Hz (for small input amplitudes), the system mass resonates. Note that from 90 Hz the control voltage U_{in} is increased to approximate a frequency independent velocity input. The base response shows a dip near 65 Hz (anti-resonance), which is the resonance of the second order mass wire rope spring system.

The base velocity also shows a second and a third harmonic component. These components are caused by non-linear behaviour, which may originate from isolator, but also from the shaker. Indeed, in appendix D.1.2, it was noted that the bare shaker itself also shows some non-linear behaviour. It is expected that the wire rope isolator shows non-linear behaviour for large deflections. In chapters 3-5, pure harmonic base excitation was used and higher order harmonics in the response directly indicate non-linear isolator behaviour. In the experimental base motion, the second and third harmonics are (globally) two decades smaller in amplitude compared tot the first harmonic (figure E.1). Note that the input amplitude axis of the frequency(-amplitude) diagrams is approximated from the magnitude of the first harmonic.

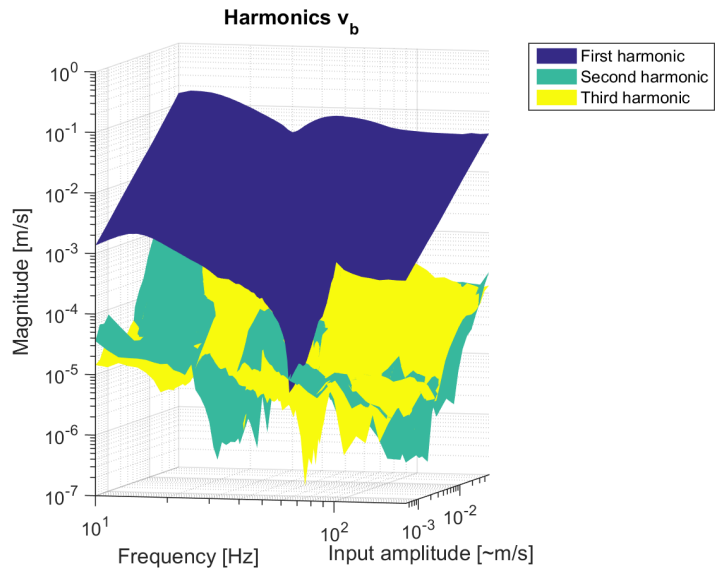


Figure E.1: Frequency-amplitude diagram, magnitude input spectrum (v_b).

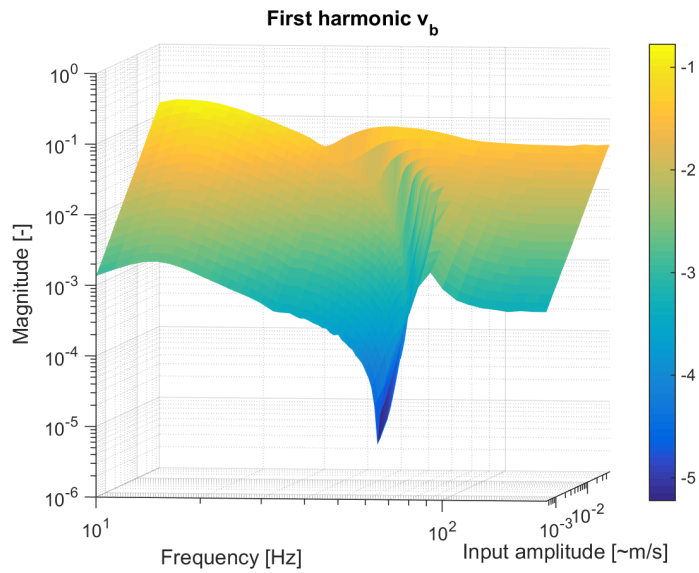


Figure E.2: Frequency-amplitude diagram, magnitude 1st harmonic v_b (input).

The response of the top mass also indicates a fourth order system. Figure E.3 shows the (dominant) first harmonic of the velocity signal. Again, near 15 Hz , the resonance of the shaker is shown, whereas near 90 Hz (for small excitation amplitudes) the resonance of the top mass is seen. The response of this mass has no anti-resonance, as expected. Note that the top mass velocity signal also contains higher harmonics, which are not shown.

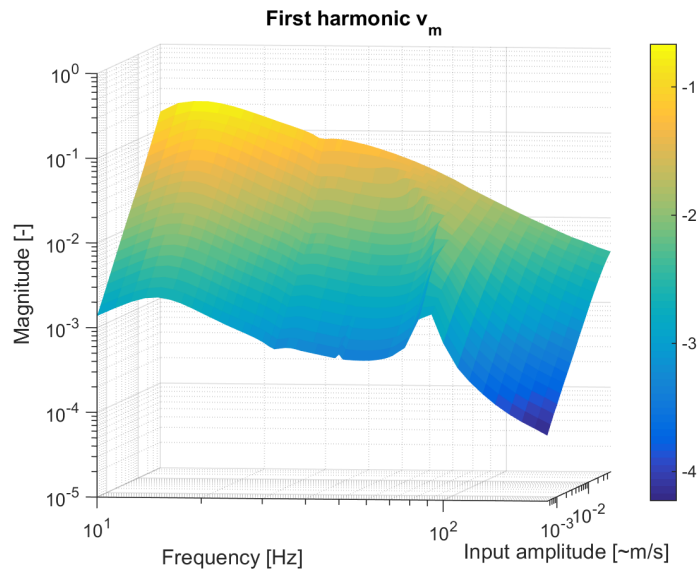


Figure E.3: Frequency-amplitude diagram, magnitude 1st harmonic v_m (response).

E.1.2 Drop test

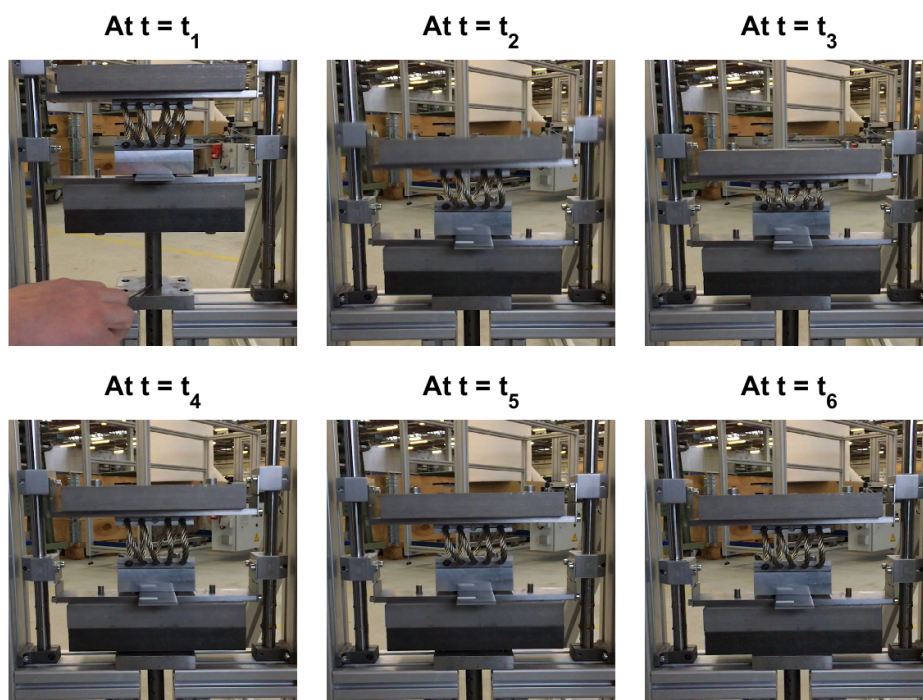


Figure E.4: Frames free fall wire rope isolator, light mass (i.e. 4.33 kg), $h = 8$ cm.

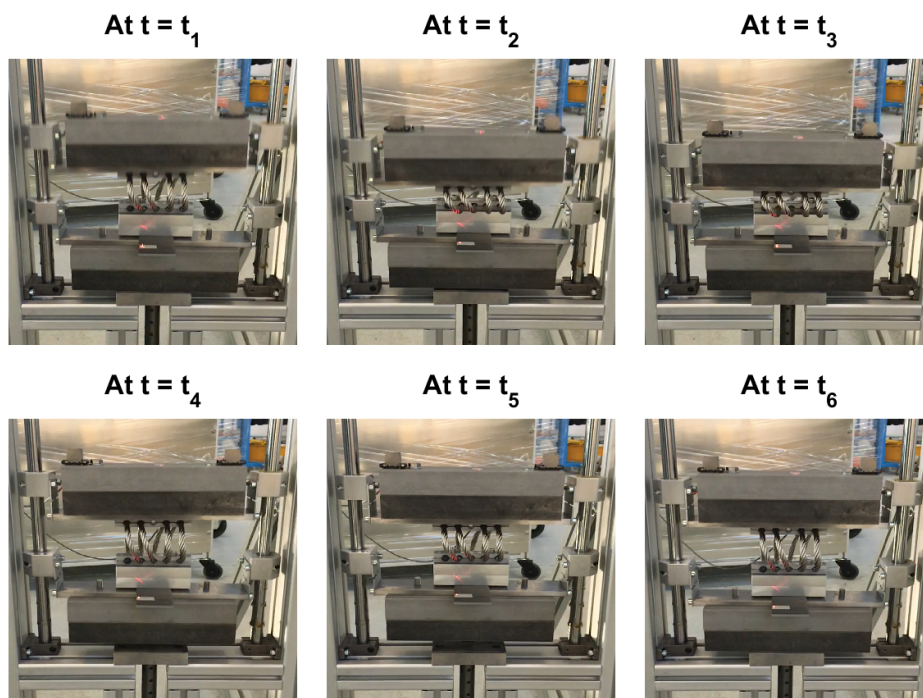


Figure E.5: Frames free fall wire rope isolator, heavy mass (i.e. 7.39 kg), $h = 8$ cm.

E.2 Measurements elastomer isolator

In this section, the analysis of the velocity signal of the shaker table in the shaker experiment (E.2.1) and time frames of the drop tests (E.2.2) for the elastomer analysis (section 6.3) are presented.

E.2.1 Shaker experiment

The harmonics of the base velocity resulting from the applied harmonic (voltage) input are shown in figure E.6. Similar to the wire rope case, the response of a fourth order system is recognized in the dominant first harmonic. Near 15 Hz , there is the shaker resonance, whereas near 30 Hz the system mass resonance is visible. Note that from 30 Hz the control voltage U_{in} is increased to approximate a frequency independent velocity input. The base velocity response shows a dip (anti-resonance) near 20 Hz , which is the resonance of the second order mass elastomer system. The (anti-)resonance frequencies seem to be independent of the input amplitude.

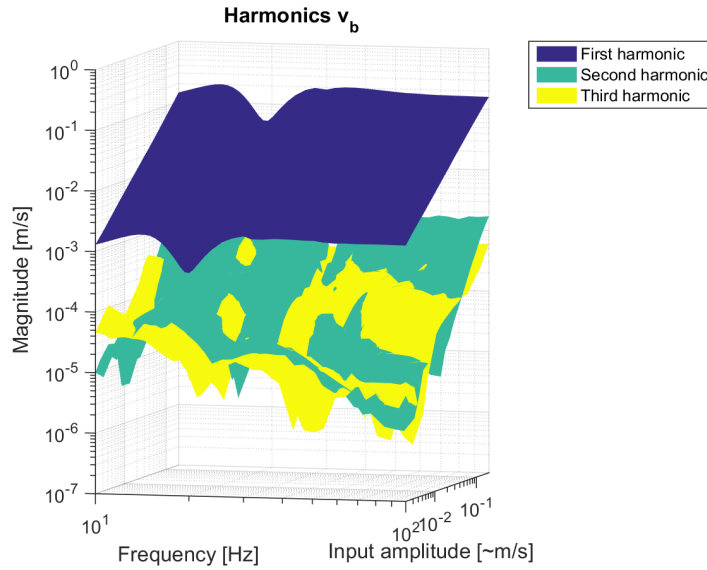


Figure E.6: Frequency-amplitude diagram, magnitude input spectrum (v_b).

Again, higher harmonics are present in the base velocity (mainly) due to the small non-linearities in the electromechanical shaker system. The amplitudes of the higher harmonics are again two decades small than the amplitude of the first harmonic. The input amplitude axis of the frequency(-amplitude) diagrams is approximated from the magnitude of the first harmonic.

E.2.2 Drop test

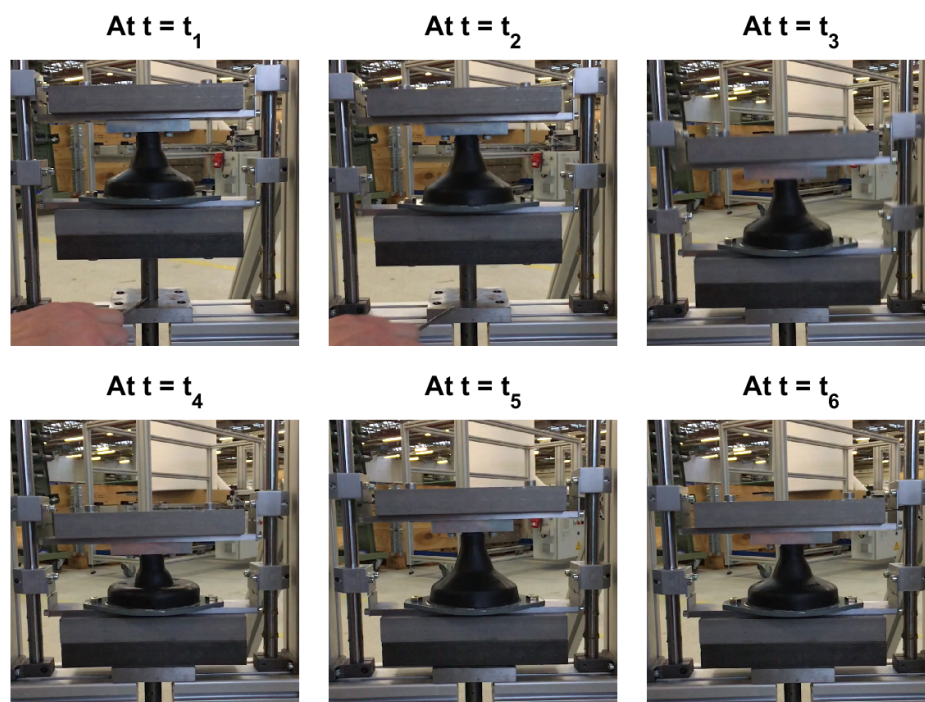


Figure E.7: Frames free fall elastomer isolator, light mass (i.e. 4.37 kg), $h = 6$ cm.

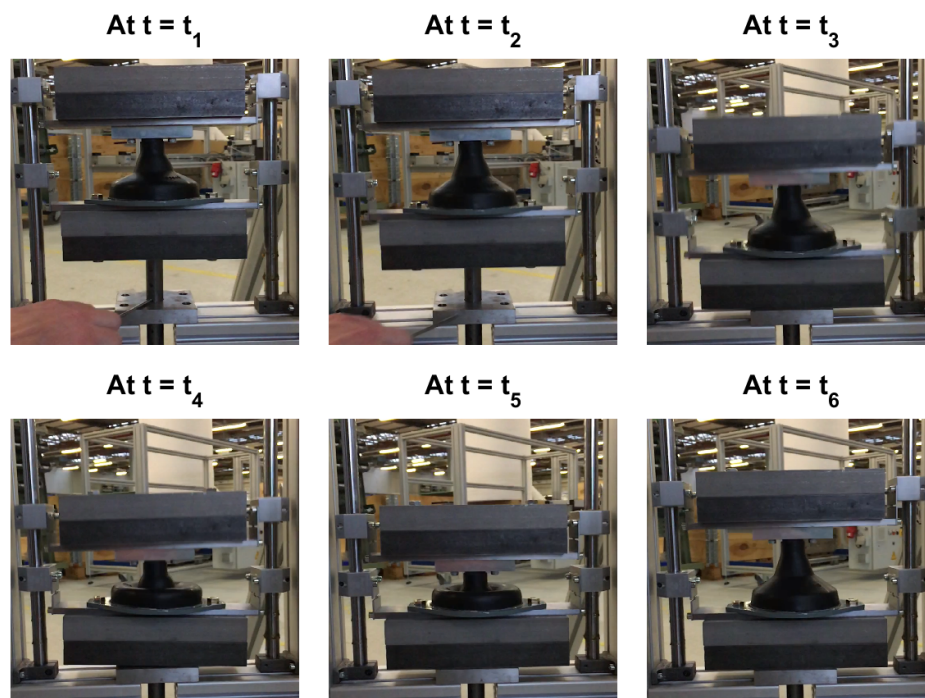


Figure E.8: Frames free fall elastomer isolator, heavy mass (i.e. 7.42 kg), $h = 6$ cm.

E.3 Measurements hybrid isolator

In this section, the analysis of the velocity signal of the shaker table in the shaker experiment (E.3.1) and time frames of the drop tests (E.3.2) for the hybrid analysis (section 6.4) are presented.

E.3.1 Shaker experiment

The first three harmonics of the base velocity are shown in figure E.9. The magnitude of the second and third order components are small but non-zero and again two decades smaller compared to the amplitude of the first harmonic.

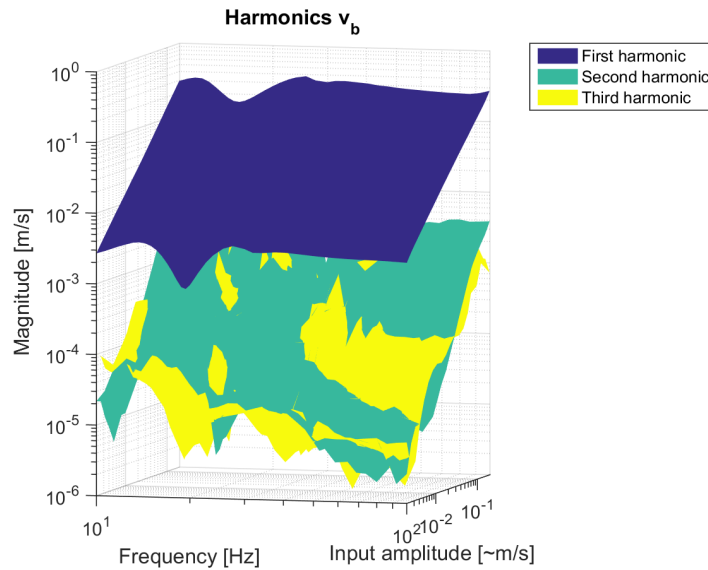


Figure E.9: Frequency-amplitude diagram, magnitude input spectrum (v_b).

The first harmonic shows the characteristics of a fourth order system. Near 14 Hz , the shaker resonance appears, whereas near 28 Hz the top mass resonance is visible. From 28 Hz , the control voltage is increased to approximate a frequency independent velocity spectrum. Near 20 Hz , an anti-resonance is shown, which coincides with the resonance of the second order isolation system. The input amplitude axis of the frequency(-amplitude) diagrams is approximated from the magnitude of the first harmonic.

E.3.2 Drop test

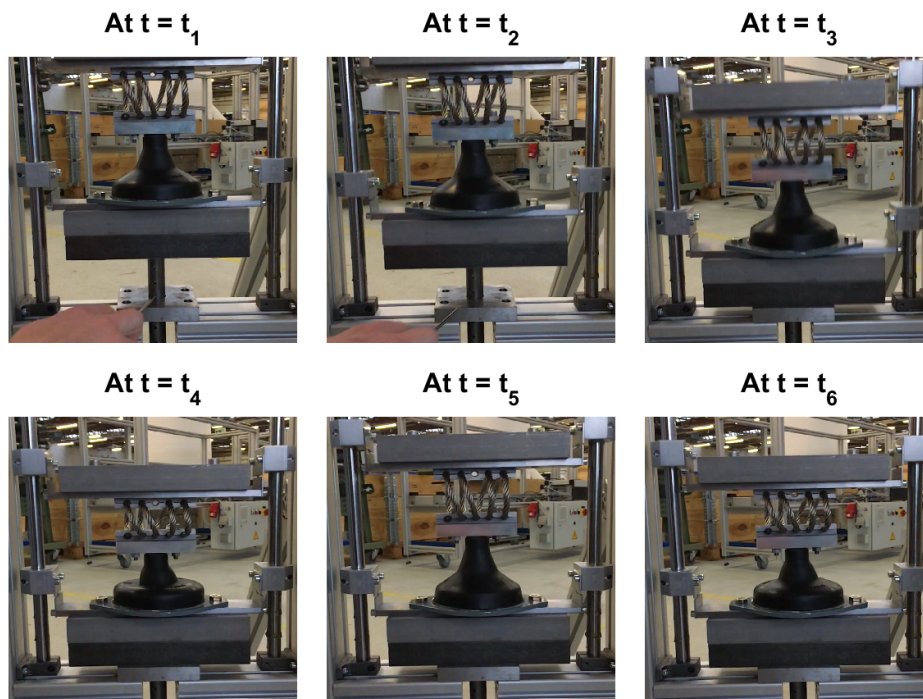


Figure E.10: Frames free fall hybrid isolator, light mass (i.e. 4.25 kg), $h = 6$ cm.

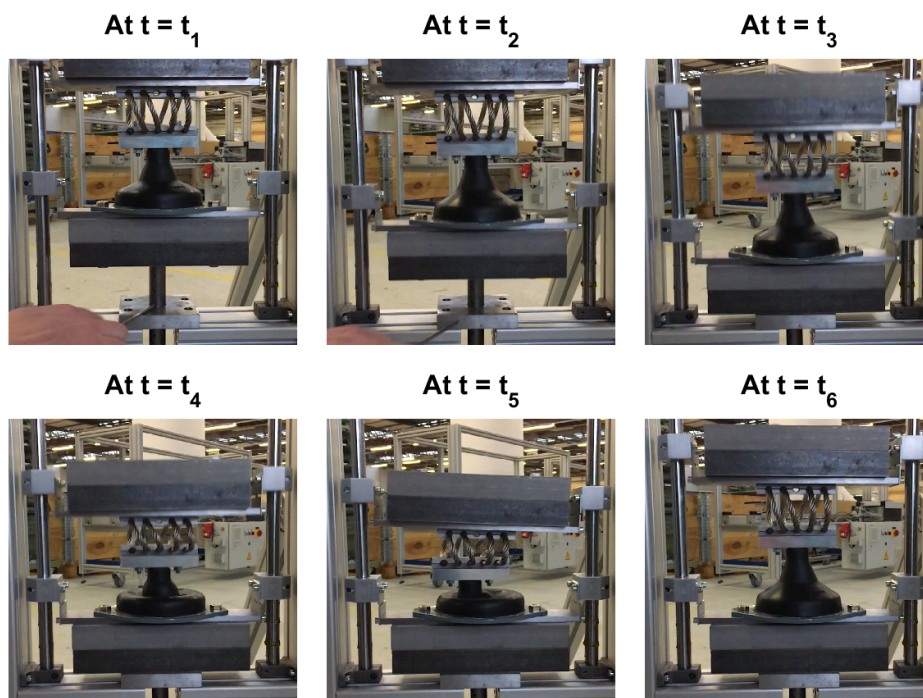


Figure E.11: Frames free fall hybrid isolator, heavy mass (i.e. 7.31 kg), $h = 6$ cm.

Appendix F

Model validation

F.1 Wire rope isolator

The identified wire rope model (section 7.1) is validated by comparing vibration and shock simulations with the experiments. Harmonic input is applied in order to analyse the frequency-amplitude behaviour and a conditioned free fall simulation examines the shock behaviour.

The input signals in the shaker test are harmonic velocity signals with varying amplitude and frequency approximated from the measurements (figure E.1). Note that in the measurement analysis the higher harmonics are ignored, whereas in the simulations both the higher order harmonics and the frequency dependent amplitude are ignored. The measurement and simulation results of the magnitude of the ratio of the first harmonic component of the system velocity response and the first harmonic component of the base velocity ($v_m/\sim v_b$) are compared. Figure F.1 shows the measurement results, whereas figure F.2 presents the simulation results. Note that figure F.1 is identical to figure 6.4.

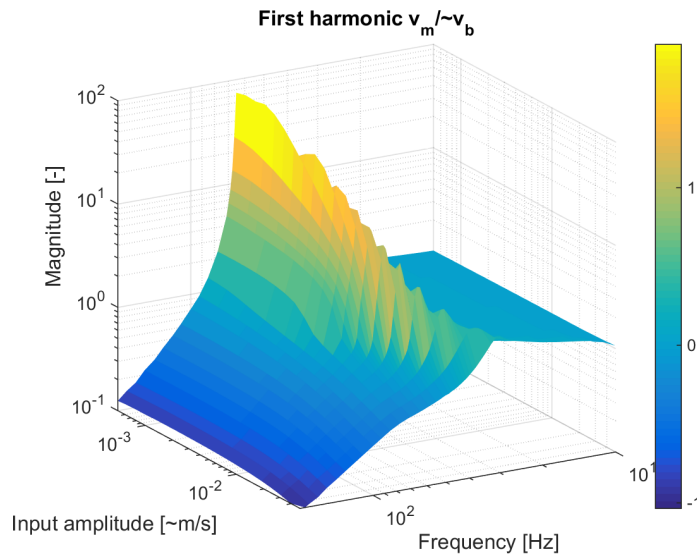


Figure F.1: Frequency-amplitude diagram $v_m/\sim v_b$, magnitude 1st harmonic, measurement.

Qualitatively, both plots correspond quite well. For low input amplitudes, the simulated resonance frequency is lower. In the model, the stiffness is underestimated for low deformation amplitudes (i.e. at micro scale). Note that the model is identified on millimeter scale deformation (in the quasi-static measurements), whereas the velocity input range here (in the vibrational measurements) corresponds with a deflection range between from micro to millimeter scale. Therefore, micro scale behaviour is

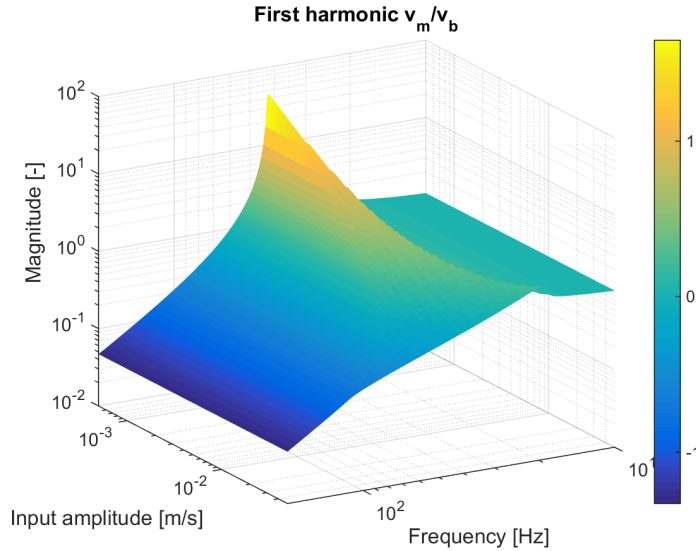


Figure F.2: Frequency-amplitude diagram $v_m/\sim v_b$, magnitude 1st harmonic, simulation.

not specifically considered in the identification. Next, the transition from stick to slip in the model is already starting at inputs lower than $5 \cdot 10^{-4} \text{ m/s}$, whereas in the measurements the transition starts from 10^{-3} m/s . The dip (anti-resonance) in velocity amplitude input observed in the measurements (i.e. near 65 Hz) is ignored in the simulations. A more detailed and fair quantitative comparison is impossible, due to the non-constant amplitude and limitations of the experimental velocity input signal.

Next, the identified wire rope model is further validated by comparing drop test results with simulation results. The relaxation during the free fall observed in section 6.2.3 is implemented in the current simulations by prescribing an initial elongation of the spring which equals the gravity of the top mass. Note that instantaneous relaxation is assumed and that the behaviour of the bottom mass is not included. It appears that relaxation is only significant for very small shocks up to an initial velocity (v_0) of 0.2 m/s , from 0.2 m/s onwards the effect of relaxation on the rest shock level is negligible. Other experimental phenomena: misalignments, bounces, and rotational and out-of-plane behaviour, are considered to be too complex phenomena to be included in the current simulation model.

Validation is done by comparing the maximum acceleration magnitude in compression and tension as function of impact velocity. Figure F.3 shows the measurement and model response for the light mass (i.e. 4.33 kg) system, where figure F.4 shows the same response for the heavy mass (i.e. 7.39 kg) system. The initial impact velocity in the measurements is not really measured but estimated from the energy laws (3.18). This law assumes a frictionless fall, and therefore the model should overestimate the actual velocity at impact. However, the measurements rather indicate a higher than lower impact velocity. Despite this and unmodelled phenomena, the simulations approximate the measurements quite well.

In figure F.3, up to 1 m/s , the model only slightly overestimates the measured accelerations. For higher initial velocities, in the model the acceleration in tension clearly exceeds the acceleration in compression. However, the acceleration in tension is overestimated by the model. A possible explanation is the detachment of the bottom mass from the ground during tension in the experiment, which is not covered by the simulation model.

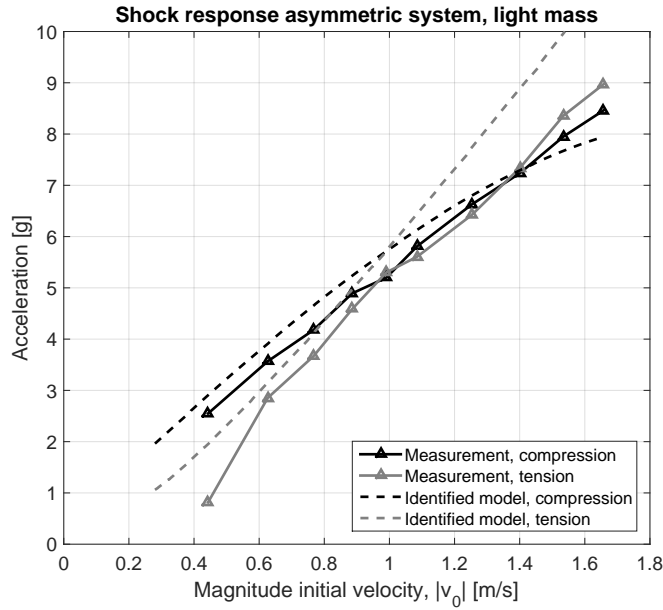


Figure F.3: Drop test: maximum accelerations in compression and tension, 4.33 kg top mass.

In figure F.4, the top to bottom mass ratio is around 1, which in the experiment results in heavier bouncing of the bottom mass after the initial impact to the ground. The model slightly overestimates the acceleration in compression over the whole initial velocity range: bouncing causes a decrease in top mass acceleration during compression. Moreover, till the moment the isolator is fully compressed, the bounces result in additional energy absorption. Again, the detachment of the the bottom mass from the ground is a possible explanation for the significant overestimation of the acceleration in tension.

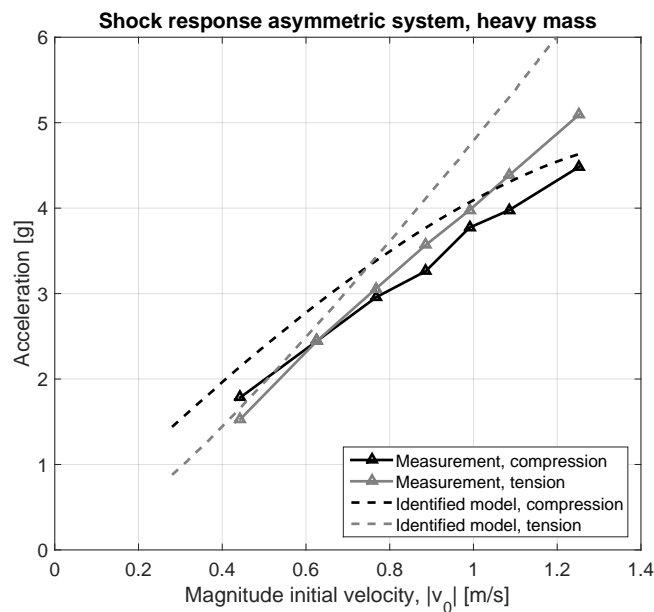


Figure F.4: Drop test: maximum accelerations in compression and tension, 7.39 kg top mass.

F.2 Elastomer isolator

The identified elastomer model (section 7.2) is validated by comparing drop test measurement results with simulation results. From the measurement analysis as summarized in section 6.5, some important effects are seen which are not included in the simulations. The stiffness of the elastomer systems is relatively low. Moreover, relaxation during free fall is significant for smaller drop heights. Therefore, instantaneous relaxation is implemented in the simulations (i.e. by an initial elongation of the elastomer which equals the gravity of the top mass). However, oscillations during the free fall, bounces at impact, rotational and out-of-plane behaviour, and elastomer non-linearities because of large deformations are not considered in the simulations.

Figure F.5 shows the rest shock level as function of the initial impact velocity. Figure F.6 shows the maximum elastomer deflection in compression. The rest shock level close to zero initial velocity is overestimated by the model for both systems, especially for the heavy mass (7.42 kg) system. It is assumed that the elastomer relaxes instantaneous at the moment of release, however it takes some time for the system to fully relax. For large compressions (larger than 15 mm), the overestimated rest shock level can be related to the unmodelled non-linear softening and rotational behaviour of the elastomer, as indicated in section 6.3.3. Moreover, for larger compressions than 15 mm the slope of the maximum deflection increases, whereas the slope of the rest shock level decreases. For compressions larger than 30 mm , it seems there is stiffening again. For low initial velocities (low drop heights) the light mass system is approximated well, the compression decreases linearly with the initial velocity and the acceleration is only slightly overestimated by the model. The heavy mass system is not described accurately. This system suffers from bouncing and there is already non-linear deflection for small initial velocities.

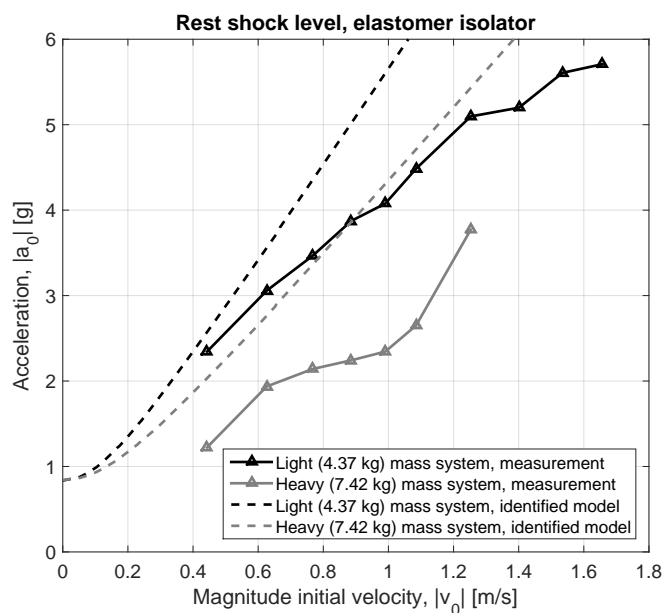


Figure F.5: Drop test: rest shock level, derived from measurement and model.

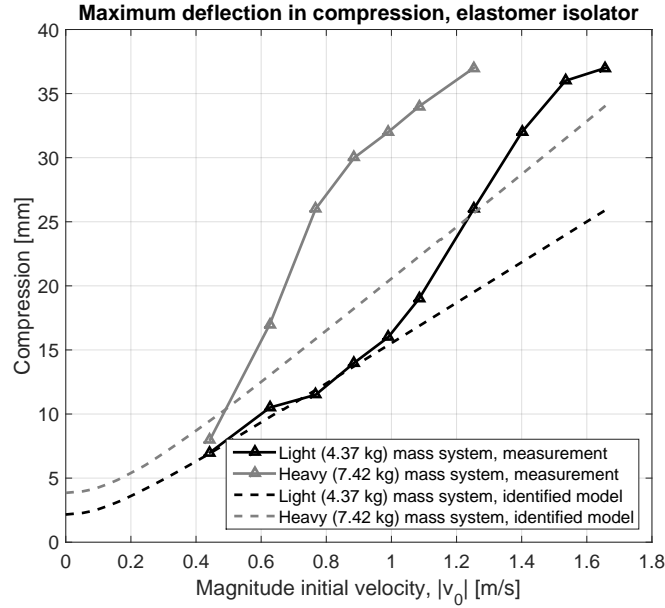


Figure F.6: Drop test: maximum deflection in compression, derived from measurement and model.

F.3 Hybrid isolator

The hybrid model (section 7.3) is validated by the shaker and drop test measurements. In section 6.4.2, already the limited velocity input amplitude range (i.e $2 \cdot 10^{-3} - 2 \cdot 10^{-1} \text{ m/s}$) of the shaker setup has been mentioned. Because of this fact, the stick-slip transition is only partly inside the measurement range. Again, the harmonic velocity input signals with varying frequency and amplitude are used. Note that in the measurement analysis the higher harmonics are ignored, whereas in the simulations both the higher order harmonics and the frequency dependent amplitude are ignored. The magnitude of the ratio of the first harmonic of the machine velocity to the (first harmonic of the) floor velocity ($v_m/\sim v_b$) is visualized for both the measurement in figure F.7 and the identified model in figure F.8. Note that figure F.7 is identical to figure 6.14.

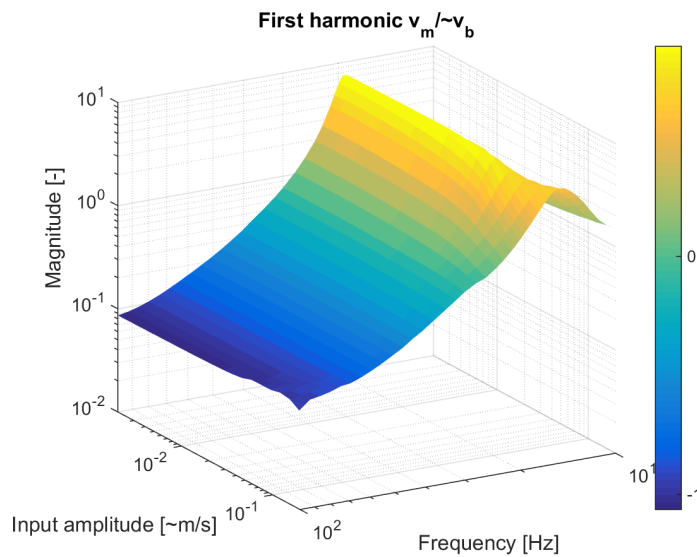


Figure F.7: Frequency-amplitude diagram $v_m/\sim v_b$, magnitude 1st harmonic, measurement.

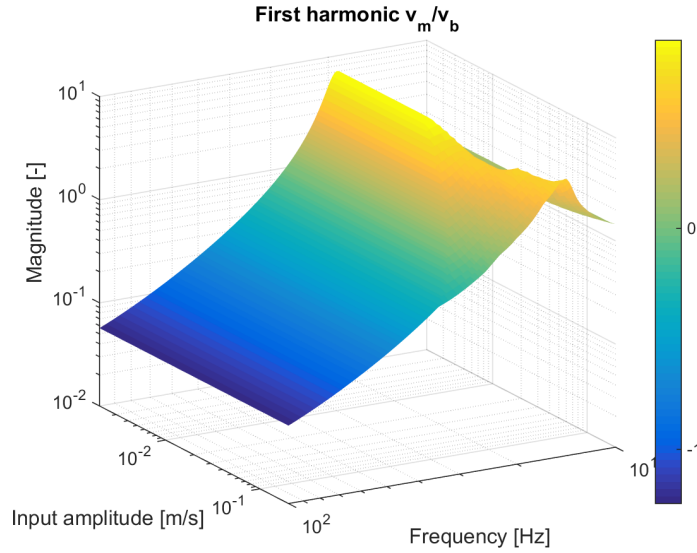


Figure F.8: Frequency-amplitude diagram $v_m/\sim v_b$, magnitude 1st harmonic, simulation.

For low input amplitudes, the resonance frequency and corresponding damping are accurately described by the model. In the low amplitude region, the elastomer component is dominant. In the model, the transition region, where the wire rope elements start to slip, starts at a lower input velocity (i.e. $2 \cdot 10^{-2} \text{ m/s}$) than in reality (i.e. $5 \cdot 10^{-2} \text{ m/s}$). This is mainly related to the velocity input amplitude; the dip in input amplitude around the resonance frequency (i.e. near 20 Hz) is not included in the simulations, i.e. in the measurements the strands are more inclined to stick. From the transition, the elastomer is no longer dominant; from here the elastomer to wire rope stiffness ratio is around 1. Moreover, note that depending on the specific wire rope isolator and elastomer isolator product type, slipping of the strands results in an increase or decrease in damping (section 5.3). Further, in the experiment only the first part of the transition region is measured. Near resonance, in the simulations a decrease in damping is shown for high input amplitudes (outside the measured range, shown in figure F.7), i.e. the effective damping of the wire rope decreases (the hysteretic loops are extended, whereas the width is constant). For frequencies close to 100 Hz the slope of the first harmonic in the measurement diagram decreases, which is caused by the dynamics of the intermediate mass. Apparently, the intermediate mass used in the model is smaller; no intermediate mass dynamics are seen in the simulations. A detailed quantitative comparison can not be made, due to the amplitude deviations and limitations of the velocity input.

Next, the model is validated by means of the drop test results. The maximum acceleration in compression and tension is shown for both a system with light (4.25 kg) top mass (figure F.9) and heavy (7.31 kg) top mass (figure F.10). Further, the maximum deflection in compression for both systems is shown in figure F.11. Similar to the elastomer isolation system, the stiffness is relatively low, which results in a high static deflection. Therefore, (instantaneous) relaxation is included in the simulations.

The light mass (i.e. 4.25 kg) system is accurately approximated by the model in the compression phase. The acceleration in compression shown in figure F.9 is only slightly overestimated. In tension, the acceleration is accurate up to an initial velocity of 0.9 m/s . For higher velocities the measured acceleration in tension is significantly lower. This is most likely caused by the detachment of the bottom mass from the ground and to a less extent by rotational and out-of-plane deformation. The effect of the non-linear (softening) character of the elastomer (section 6.3.3 and appendix F.2) is apparently small on the acceleration in compression. The maximum deflection in compression of the light mass system is visualized in figure F.11. The model is accurate up to an initial velocity of 1.2 m/s (which corresponds with a maximum compression of 25 mm). For higher velocities, the measured compression is clearly higher than

the predicted compression. This effect is probably caused by the non-linear elastomer character (i.e. softening). The low velocity deflection is accurately approximated by the simulations of the identified model.

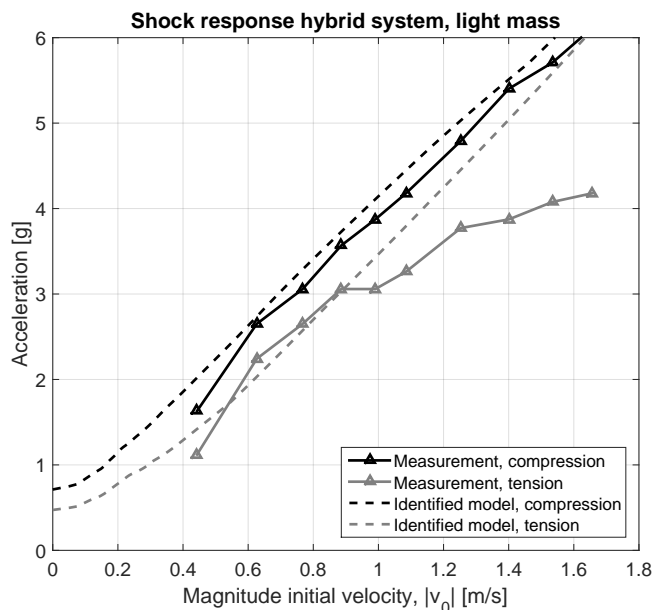


Figure F.9: Drop test: maximum accelerations in compression and tension, 4.25 *kg* top mass.

The top mass accelerations of the heavy mass (i.e. 7.31 *kg*) system are shown in figure F.10. The system response is clearly overestimated by the model. For high initial velocities, this is probably related to bouncing, bottom mass detachment from the ground, elastomer non-linearity (i.e. softening), and rotational and out-of-plane behaviour. Moreover, all these effects cause a decrease in acceleration. Further, for low initial velocities, the system is not fully relaxed at the moment of impact, whereas in the simulation instantaneous relaxation is assumed. Hereby both the impact velocity and consequently acceleration are overestimated by the model. The maximum compression is shown in figure F.11. The underestimation for low initial velocities is probably mainly caused by the incomplete relaxation, while the overestimation for high velocities is most likely caused by the bounces, detachment, elastomer non-linearity, and rotational and out-of-plane deformation.

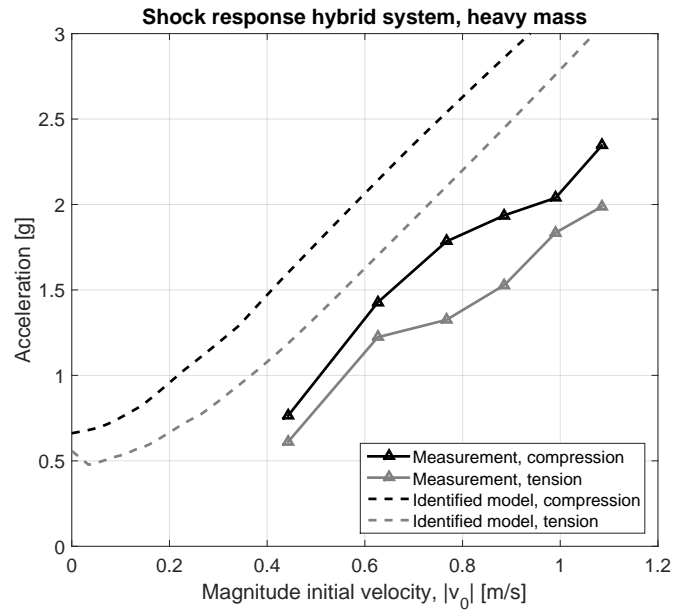


Figure F.10: Drop test: maximum accelerations in compression and tension, 7.31 kg top mass.

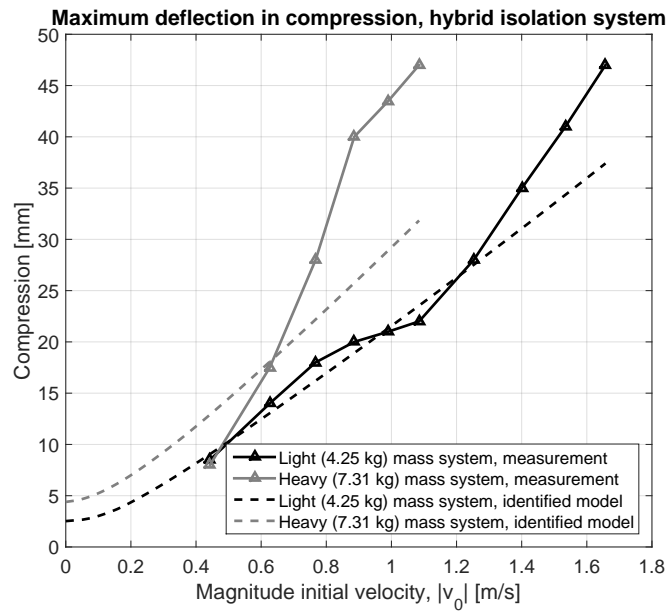


Figure F.11: Drop test: maximum deflection in compression, derived from measurement and model.

Acknowledgements

This graduation project is performed at Eindhoven University of Technology and NTS Systems Development in Eindhoven. It was not possible to successfully finish this thesis without the help and support of many people.

To begin, I would like to offer my special thanks to prof.dr. Henk Nijmeijer, my supervisor, for the opportunity to work on this project and for his knowledge, constructive discussions, and feedback. I also want to thank dr.ir. Rob Fey, my coach at the university, his advice and critical comments were very helpful. In particular I want to thank him for the time and effort he put in the detailed review of this report. Without the assistance from the people of the DCT-lab, I was not able to perform the measurements. Further, a special thanks to dr.ir. Nick Rosielle for the use of his measurement equipment. Dr.ir. Joris Remmers is acknowledged for his work as member of the committee.

At NTS I got the opportunity to work on this challenging project, for which I am very grateful. Especially I would like to thank dr.ir. Pieter Nuij and ir. Araz Abbasi, my coaches, for their useful input, critical feedback, practical view, and enthusiasm. Also the help and advice from the people of NTS Mechatronics was essential to build the valuable measurement setups. Many thanks as well to all other colleagues for their inspiring conversations and advice.

Finally, I would like to thank my parents Piet and Bea, and my siblings for their support, sincere interest, and encouragement throughout my whole study.

Joep Tax
May 2016

